

**Femtosecond-laser Microstructuring of Silicon  
for Novel Optoelectronic Devices**

A thesis presented

by

James Edward Carey III

to

The Division of Engineering and Applied Sciences

in partial fulfillment of the requirements

for the degree of

Doctor of Philosophy

in the subject of

Applied Physics

Harvard University

Cambridge, Massachusetts

July 2004

©2004 by James Edward Carey III

All rights reserved.

# **Femtosecond-laser Microstructuring of Silicon for Novel Optoelectronic Devices**

Eric Mazur

James E. Carey III

## **ABSTRACT**

This dissertation comprehensively reviews the properties of femtosecond-laser microstructured silicon and reports on its first application in optoelectronic devices. Irradiation of a silicon surface with intense, short laser pulses in an atmosphere of sulfur hexafluoride leads to a dramatic change in the surface morphology and optical properties. Following irradiation, the silicon surface is covered with a quasi-ordered array of micrometer-sized, conical structures. In addition, the microstructured surface has near-unity absorptance from the near-ultraviolet (250 nm) to the near-infrared (2500 nm). This spectral range includes below-band gap wavelengths that normally pass through silicon unabsorbed.

We thoroughly investigate the effect of experimental parameters on the morphology and chemical composition of microstructured silicon and propose a formation mechanism for the conical microstructures. We also investigate the effect of experimental parameters on the optical and electronic properties of microstructured silicon and speculate on the cause of below-band gap absorption. We find that sulfur incorporation into the silicon surface plays an important role in both the formation of sharp, conical microstructures and the near-unity absorptance at below-band gap wavelengths.

Because of the novel optical properties, femtosecond-laser microstructured silicon has potential application in numerous optoelectronic devices. We use femtosecond-laser microstructured silicon to create silicon-based photodiodes that are one hundred times more sensitive than commercial silicon photodiodes in the visible, and five orders of magnitude more sensitive in the near-infrared. We also create femtosecond-laser microstructured silicon solar cells and field emission arrays.

# Table of Contents

<i>Abstract</i>	<i>iii</i>
<i>Table of Contents</i>	<i>iv</i>
<i>List of Figures</i>	<i>vii</i>
<i>List of Tables</i>	<i>x</i>
<i>Acknowledgements</i>	<i>xi</i>
<i>Citations to Published Work</i>	<i>xiv</i>
<b>1 Introduction</b>	<b>1</b>
<b>2 Femtosecond-laser microstructured silicon</b>	<b>4</b>
2.1 Background . . . . .	5
2.2 Apparatus and procedure . . . . .	8
<b>3 Morphology and chemical composition</b>	<b>13</b>
3.1 Effect of shot number . . . . .	14
3.1.1 Surface morphology . . . . .	14
3.1.2 Surface layer structure and composition . . . . .	21
3.2 Spot samples <i>vs.</i> translated samples . . . . .	24
3.3 Effect of fluence . . . . .	27
3.3.1 Surface morphology . . . . .	27
3.3.2 Surface layer structure and composition . . . . .	30
3.4 Effect of pulse duration . . . . .	31
3.4.1 Surface morphology . . . . .	32
3.4.2 Surface layer structure and composition . . . . .	34
3.5 Effect of laser wavelength . . . . .	36
3.5.1 Surface morphology . . . . .	36
3.5.2 Surface layer structure and composition . . . . .	38
3.6 Effect of polarization and propagation direction . . . . .	38
3.6.1 Surface morphology . . . . .	39

---

3.6.2	Surface layer structure and composition . . . . .	40
3.7	Effect of ambient gas . . . . .	40
3.7.1	Surface morphology . . . . .	40
3.7.2	Surface layer structure and composition . . . . .	47
3.8	Effect of ambient gas pressure . . . . .	49
3.8.1	Surface morphology . . . . .	50
3.8.2	Surface layer structure and composition . . . . .	50
3.9	Effect of annealing . . . . .	51
3.9.1	Surface morphology . . . . .	51
3.9.2	Surface layer structure and composition . . . . .	52
3.10	Effect of silicon substrate properties . . . . .	53
3.11	Summary of chemical composition (RBS data) and trends . . . . .	53
3.12	Discussion . . . . .	55
<b>4</b>	<b>Optical and electronic properties</b>	<b>61</b>
4.1	Optical measurements . . . . .	62
4.1.1	Optical properties of femtosecond-laser microstructured silicon . . . . .	63
4.1.2	Effect of shot number . . . . .	64
4.1.3	Effect of fluence . . . . .	65
4.1.4	Effect of pulse duration . . . . .	65
4.1.5	Effect of laser wavelength, polarization, and propagation direction . . . . .	67
4.1.6	Effect of ambient gas . . . . .	67
4.1.7	Effect of gas pressure . . . . .	69
4.1.8	Effect of annealing . . . . .	69
4.1.9	Effect of silicon substrate properties . . . . .	71
4.2	Electronic measurements . . . . .	71
4.2.1	Hall effect and resistivity measurements: procedure and apparatus . . . . .	71
4.2.2	Results . . . . .	76
4.3	Discussion . . . . .	81
<b>5</b>	<b>Femtosecond-laser microstructured silicon photodiodes</b>	<b>86</b>
5.1	Introduction to photodiodes: the $p$ - $n$ junction . . . . .	87
5.2	Femtosecond-laser microstructured silicon photodiodes . . . . .	94
5.2.1	Experimental . . . . .	96
5.2.2	Results . . . . .	98
5.3	Optimization and discussion . . . . .	110
<b>6</b>	<b>Solar cells, field emission, and future directions</b>	<b>117</b>
6.1	Solar cells and renewable energy . . . . .	118
6.2	Femtosecond-laser microstructured silicon solar cells . . . . .	119
6.2.1	Introduction to solar cells . . . . .	119
6.2.2	Recent progress . . . . .	122
6.3	Field emission from femtosecond-laser microstructured silicon surfaces . . . . .	126
6.3.1	Introduction to field emission . . . . .	126
6.3.2	Field emission results . . . . .	131

---

6.4 Future directions . . . . .	134
<b>7 Summary and outlook</b>	<b>135</b>
<b>References</b>	<b>138</b>

# List of Figures

2.1	Morphology of femtosecond-laser microstructured silicon. . . . .	5
2.2	Optical properties of femtosecond-laser microstructured silicon. . . . .	7
2.3	Microstructuring apparatus. . . . .	9
3.1	Evolution of surface morphology with increasing shot number. . . . .	15
3.2	Fourier analysis of a silicon surface after 2 laser pulses in SF <sub>6</sub> . . . . .	16
3.3	Fourier analysis of a silicon surface after 5 laser pulses in SF <sub>6</sub> . . . . .	17
3.4	Fourier analysis of a silicon surface after 10 laser pulses in SF <sub>6</sub> . . . . .	18
3.5	A sideview of a cleaved microstructured silicon sample. . . . .	19
3.6	Fourier analysis of a silicon surface after 500 laser pulses in SF <sub>6</sub> . . . . .	21
3.7	Transmission electron micrographs of samples made with 10 and 500 laser pulses. . . . .	22
3.8	Comparison of morphology for stationary and translated samples. . . . .	25
3.9	Morphology of stationary sample made with changing pulse energy. . . . .	26
3.10	Morphology of samples made at different fluences. . . . .	27
3.11	Morphology variation in a single irradiated spot. . . . .	29
3.12	Self-ordered silicon nano-islands formed with low fluence irradiation. . . . .	30
3.13	Transmission electron micrographs of samples made with fluence 8 kJ/m <sup>2</sup> and 4 kJ/m <sup>2</sup> . . . . .	31
3.14	Morphology of samples made with two pulse durations: 100 femtoseconds and 30 nanoseconds. . . . .	32
3.15	Microstructure separation for several pulse durations. . . . .	34
3.16	Transmission electron micrographs of samples made with femtosecond and nanosecond laser pulses. . . . .	35
3.17	Evolution of surface morphology with increasing shot number for samples made with 400 nm laser pulses. . . . .	37
3.18	Morphology of samples made with different laser polarizations. . . . .	39
3.19	Morphology of samples made with different gas species. . . . .	41
3.20	Fourier analysis of a silicon surface after 2 laser pulses in vacuum. . . . .	43
3.21	Fourier analysis of a silicon surface after 50 laser pulses in vacuum. . . . .	44
3.22	Fourier analysis of a silicon surface after 200 laser pulses in vacuum. . . . .	45
3.23	Fourier analysis of a silicon surface after 500 laser pulses in vacuum. . . . .	46

3.24	Morphology of samples made with different gas species at high magnification.	47
3.25	Fractional concentration of chemical species for different ambient gases. . .	49
3.26	Morphology of samples made in different pressures of SF <sub>6</sub> . . . . .	50
3.27	Morphology of samples after annealing. . . . .	51
3.28	Transmission electron micrographs of samples before and after annealing. .	52
4.1	Optical properties of femtosecond-laser microstructured silicon. . . . .	63
4.2	Optical properties of microstructured silicon at different shot numbers. . . .	64
4.3	Optical properties of microstructured silicon at different fluences. . . . .	65
4.4	Optical properties of microstructured silicon at different pulse durations. . .	66
4.5	Optical properties of microstructured silicon for different ambient gas species.	67
4.6	Optical properties of microstructured silicon for different pressures of SF <sub>6</sub> . .	69
4.7	Optical properties of microstructured silicon after annealing. . . . .	70
4.8	A silicon sample prepared for resistivity and Hall voltage measurements. . .	73
5.1	Creation of a <i>p-n</i> junction. . . . .	88
5.2	A <i>p-n</i> junction in thermal equilibrium. . . . .	90
5.3	The effect of an externally applied voltage (electric field) on a <i>p-n</i> junction.	91
5.4	Current-voltage characteristics of a <i>p-n</i> diode. . . . .	94
5.5	Schematic diagrams of a femtosecond-laser microstructured silicon photodiode.	97
5.6	Current-voltage characteristics of microstructured silicon photodiodes after annealing. . . . .	99
5.7	Responsivity of microstructured silicon photodiodes after annealing. . . . .	100
5.8	Current-voltage characteristics of microstructured silicon photodiodes made with different fluences. . . . .	101
5.9	Responsivity of microstructured silicon photodiodes made with different flu- ences. . . . .	102
5.10	Current-voltage characteristics of microstructured silicon photodiodes made with different substrate dopings. . . . .	103
5.11	Responsivity of microstructured silicon photodiodes made with different sub- strate dopings. . . . .	104
5.12	Responsivity measurements with no applied bias (quantum efficiency). . . .	105
5.13	Responsivity with increasing back bias. . . . .	107
5.14	Current-voltage characteristics and responsivity measurements with decreas- ing temperature. . . . .	108
5.15	Photodiode characteristics for a heavily sulfur doped amorphous silicon layer and a laser annealed surface layer. . . . .	109
5.16	Photodiode characteristics for an optimized femtosecond-laser microstruc- tured silicon photodiode. . . . .	111
6.1	Spectral irradiance distribution of the solar spectrum. . . . .	120
6.2	The difference between photoconductive and photovoltaic mode. . . . .	121
6.3	Maximum power rectangle and fill factor of a solar cell. . . . .	123
6.4	Current-voltage characteristics for femtosecond-laser microstructured silicon solar cells under one sun illumination. . . . .	124

---

6.5	Energy level arrangement versus position for field emission from a metal surface.	128
6.6	Energy level arrangement versus position for field emission from a semiconductor surface. . . . .	130
6.7	Field emission measurement apparatus. . . . .	131
6.8	Field emission measurements from a silicon surface microstructured in SF <sub>6</sub> .	132
6.9	Field emission measurements from silicon surfaces microstructured in N <sub>2</sub> , Cl <sub>2</sub> , and air. . . . .	133

# List of Tables

3.1	Summary of sulfur concentration data. . . . .	54
3.2	Summary of the trends in morphology and composition with experimental parameters. . . . .	55
4.1	Electronic properties of microstructured silicon made at different fluences. .	77
4.2	Electronic properties of microstructured silicon after annealing. . . . .	78
4.3	Electronic properties of microstructured silicon for <i>p</i> -doped substrates. . . .	79
4.4	Electronic properties of microstructured <i>p</i> -doped substrates after annealing.	80

# Acknowledgements

Without the support of family, friends, and coworkers, I never would have reached this point. Today, I am putting the finishing touches on my dissertation and thereby completing my doctorate. As my last task in this process, I want to thank everyone who has helped me along the way.

I would first like to thank my advisor Eric Mazur and the Mazur group itself. When I first arrived at Harvard, I found it to be quite a challenge. I honestly did not think I would be able to finish. However, the supportive environment that Eric and the rest of the Mazur group provided helped me overcome my initial fears. Since joining the group, Eric has granted me enormous freedom in my pursuits. He taught me how to be a good researcher, the importance of motivating your audience, when teaching or speaking in front of an audience, and how to clearly convey ideas. I greatly enjoyed having Eric as a mentor and friend over these past five years.

There are many members of the Mazur group that I wish to thank. I begin with the elder members who made me feel so welcome five years ago. Adam, Albert, Nan, Claudia, Paul, Chris Schaffer, Chris Roeser, and Jon were all wonderful colleagues and quick with any advice or help I needed when I joined the group. In particular, I thank Chris R. for showing me the right way to do pretty much everything; and Jon for simultaneously keeping me focused on finishing and wasting precious research time with random conversation.

I also would like to thank the younger students that have come along and are the future of the group. Rafael, Iva, and Maria made my time here more enjoyable with every day. It feels as though we have banded together to fight through the struggles of graduate school. I thank Rafa for being thoughtful and generous no matter what the situation; Iva for keeping my spirits high and keeping me in shape; and Maria for being such a good friend and a good sport when I occasionally joked around at her expense. I would also like to thank Alex and Veronica for showing me how a postdoc is done, and for being such wonderful people and welcome additions to the group. There have also been some recent additions to the graduate student supply in Sam, Loren, Geoff, and Prakriti. I hope to get to know all of you better, and that your time here will be as rewarding as mine has been.

Then there are all the people I have had the pleasure of working directly alongside: Catherine, Michael, Rebecca, Brian, Mengyan, Claudia, Li, and Josh. I owe all of you a debt of gratitude for your friendships and your hard work that contributed so much to my own progress. I would especially like to thank Catherine and Michael, who were there with me through most of this experience and made each working day a pleasure. I also want to wish Brian luck with carrying on our work; I know it is in good hands.

Lastly, I would like to thank my family and friends for being so loving and supportive. My friends may not even know what I actually do in graduate school, but they always helped me through hard times and helped me relax when needed. I thank Guy for being the best roommate and friend a Harvard graduate student could as for. Most of all, I thank my parents and my sisters, Charlene, Beth, and Tina. They made me who I am today and any successes I have can be attributed to them. They raised me right and I can be proud of what I have accomplished because I know that they are proud of me. I would also like to thank the rest of my family including all my brother-in-laws, Rich, Steve, and Mike, for being good friends and the brothers I never had. Many thanks to my loving and

wonderful girlfriend Beth; you have been so patient, understanding, and caring during this last push toward my degree. Your support made everything seem easier and possible.

It is a nearly impossible task to adequately thank everyone for helping me through these last five years. I consider myself extremely lucky to have the friends and loved ones that I have, and to have found myself surrounded by good friends and cohorts at work. Thank you everyone, my future is bright because of you.

*James Carey  
Cambridge, Massachusetts  
August, 2004*

### **Acknowledgements of Financial Support**

This thesis is based on work supported by the Department of Energy under contract DE-FC36-016011051 and by the Army Research Office under contract DAAD19-99-1-0009. My time in graduate school was partially funded by a fellowship provided by the Department of Defense.

# Citations to Published Work

Parts of this dissertation cover research reported in the following articles:

- [1] J. E. Carey, C. H. Crouch, M. A. Sheehy, M. Shen, C. Friend, and E. Mazur, “High sensitivity silicon-based VIS/NIR photodetectors,” *to be submitted to Optics Lett.*, 2004.
- [2] C. H. Crouch, J. E. Carey, M. Shen, E. Mazur, and F. Y. Genin, “Infrared absorption by sulfur-doped silicon formed by femtosecond laser irradiation,” *accepted for publication in Appl. Phys. A*, 2004.
- [3] C. H. Crouch, J. E. Carey, J. M. Warrender, M. J. Aziz, E. Mazur, and F. Y. Genin, “Comparison of structure and properties of femtosecond and nanosecond laser-structured silicon,” *Appl. Phys. Lett.*, vol. 84, p. 1850, 2004.
- [4] J. E. Carey, C. H. Crouch, and E. Mazur, “Femtosecond-laser-assisted microstructuring of silicon surfaces,” *Optics and Photonics News*, p. 32, February 2003.
- [5] R. J. Younkin, J. E. Carey, E. Mazur, J. Levinson, and C. Friend, “Infrared absorption by conical silicon microstructures made in a variety of background gases using femtosecond-laser pulses,” *J. Appl. Phys.*, vol. 93, p. 2626, 2003.
- [6] M. Y. Shen, C. H. Crouch, J. E. Carey, R. Younkin, M. Sheehy, C. M. Friend, and E. Mazur, “Formation of regular arrays of silicon microspikes by femtosecond laser irradiation through a mask,” *Appl. Phys. Lett.*, vol. 82, p. 1715, 2003.
- [7] C. Wu, C. H. Crouch, L. Zhao, J. E. Carey, R. J. Younkin, J. Levinson, E. Mazur, R. M. Farrel, P. Gothoskar, and A. Karger, “Near-unity below-band gap absorption by microstructured silicon,” *Appl. Phys. Lett.*, vol. 78, p. 1850, 2001.

To MY PARENTS –

*for always teaching and keeping me grounded.*

*I am a great believer in luck and I find the harder I work, the more I have of it.*

THOMAS JEFFERSON

# Chapter 1

## Introduction

Silicon is the most prevalent semiconductor used in microelectronics and photonics. Second only to oxygen in earthly abundance, silicon is produced in higher volume for lower cost than any other semiconductor. Its readily grown oxide made silicon the material of choice for the semiconductor device industry. A band gap of 1.07 eV leads to efficient detection of visible light and conversion of sunlight into electricity. Easily integrated with other microelectronics, silicon is used in many forms (including crystalline, amorphous, and porous) in numerous opto-electronic devices.

However, silicon has several shortcomings: as an indirect band-gap material, it is a poor light emitter; silicon cannot be used to detect many important communications wavelengths; and silicon solar cells fail to convert nearly a third of the sun's spectrum into electricity. A large research effort is directed at manipulating the properties of silicon to overcome these shortcomings. Despite the existence of other semiconductor materials that can better detect longer wavelengths, it is the low cost and easy integration with existing silicon fabrication techniques that drives research to find new forms and uses of silicon.

This dissertation describes a method for using the intense conditions created at

the focus of a femtosecond laser pulse to create a new form of silicon with unique optical and electronic properties. Through an interdisciplinary effort that involves ultrafast optical techniques and material science, we investigate the reasons for the unique properties and apply our conclusions toward creating novel optoelectronic devices. Although our methods can be used to create a wide variety of interesting materials, we concentrate on femtosecond-laser microstructured silicon surfaces for use in photodetectors, photovoltaics, and field emission devices.

### **Organization of the dissertation**

Chapter 2 is a brief review of the history and context of femtosecond-laser microstructuring of silicon. We also introduce the microstructuring apparatus and procedure.

Chapter 3 examines the effect of experimental parameters on surface morphology and chemical composition. The intense conditions at the focus of the laser cause ablation and melting of the silicon surface; the molten surface evolves and interacts with chemical species present in the ambient gas before resolidifying with an altered morphology. The inclusion of sulfur into the surface during laser irradiation is crucial in conical microstructure formation.

Chapter 4 examines the effect of experimental parameters on the optical and electronic properties of the laser-disordered surface layer. Silicon microstructured in a sulfur hexafluoride environment has near-unity absorptance for both the visible and near-infrared spectrum. The increased absorption is a result of surface texturing and inclusion of high levels of sulfur in a nonequilibrium arrangement. Annealing to high temperatures eliminates absorption in the near-infrared and greatly increases the number of donor carriers contributed by implanted sulfur atoms.

Chapter 5 presents the use of femtosecond-laser microstructured silicon to make

highly sensitive photodiodes for the visible and near-infrared. We successfully create silicon-based photodetectors that utilize the extended absorption range of surfaces microstructured in sulfur hexafluoride. Large gain at small applied biases is responsible for the high sensitivity of the photodiodes. The gain mechanism is related to disorder in the surface layer and is eliminated with annealing to high temperatures.

Chapter 6 presents the use of femtosecond-laser microstructured silicon to make novel solar cells and field emission arrays. Lessons learned while creating photodiodes help identify and remedy past problems in these areas. We demonstrate femtosecond-laser microstructured silicon solar cells for the first time and these solar cells show great potential for use in thin film solar cells. We also present results for field emission from microstructured surfaces with low turn-on fields and high emission currents.

Chapter 7 summarizes the work contained within the dissertation and comments on the future of the research. Past successes and current progress indicate that femtosecond-laser microstructuring has numerous potential future applications.

## Chapter 2

# Femtosecond-laser microstructured silicon

Six years ago, we reported the first observation of conical microstructures formed on the surface of silicon following irradiation with femtosecond laser pulses in an atmosphere of sulfur hexafluoride. A serendipitous and quite unexpected result, femtosecond-laser microstructured silicon was born from experiments on ultrashort laser pulse induced chemical reactions at semiconductor surfaces. In the ensuing six years, we investigated both the formation and physical properties of microstructured silicon; our experimental goals and motivations have grown from solely morphological curiosity to applications in novel semiconductor devices.

This chapter presents a brief introduction to the history of our work and its context in the area of laser microstructuring of semiconductor surfaces. We begin with a description of our initial experiments and how our motivations and goals have changed with time. We also describe comparable work being done on laser microstructuring of semiconductor surfaces. At the end of the chapter, we present the experimental apparatus and procedure

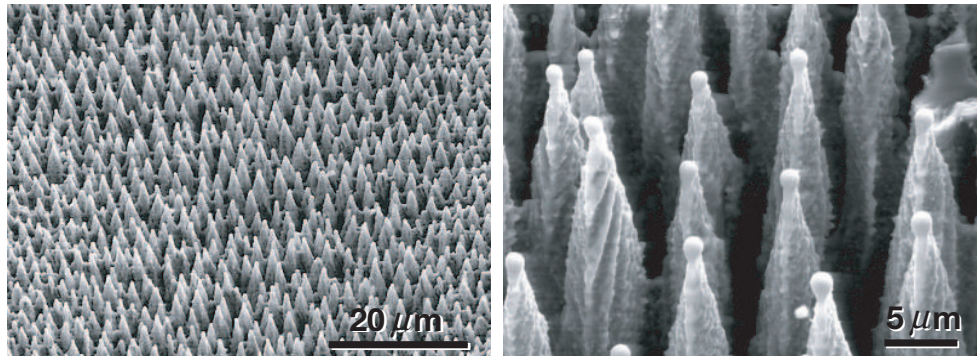


Figure 2.1: Scanning electron micrographs of typical surface morphologies for femtosecond-laser microstructured silicon at two magnifications. Both micrographs are taken at a 45° angle.

used in making femtosecond-laser microstructured silicon.

## 2.1 Background

We first reported on the formation of conical microstructures on silicon in 1998 [1, 2]. Irradiation of a silicon surface with several hundred femtosecond-laser pulses of fluence  $10 \text{ kJ/m}^2$  in an atmosphere of sulfur hexafluoride ( $\text{SF}_6$ ) results in a quasi-ordered array of micrometer-sized, conical structures (see Figure 2.1). The morphology of the microstructures exhibits spontaneous ordering and sharpness unmatched by other laser structuring methods at the time.

Since the early 1970's, researchers have reported on the appearance of spontaneous periodic surface ripples following laser irradiation [3, 4, 5]. The ripples, later named Laser Induced Periodic Surface Structures (LIPPS), are small undulations on the surface with spatial periods closely related to the central wavelength of the laser. These structures share the spontaneous ordering seen in femtosecond-laser microstructured silicon, but not the dramatic surface topography. A decade later, the formation of conical microstructures with

laser irradiation was first reported [6]. The laser "sputter-cones" were initially an unwanted byproduct of laser sputtering of targets in pulsed laser deposition experiments. Although conical, sputter-cones are irregular, disordered across the surface, and more blunt than our microstructures. In the mid to late 1990's, a few research groups began examining more exotic structure formation on silicon following laser irradiation [7, 8, 9, 10]. The structures formed in these experiments also lacked the sharpness and ordering of structures formed with femtosecond-laser irradiation in an atmosphere of SF<sub>6</sub>.

Because the morphology of our microstructures is unique, initial experiments focused on formation mechanisms and the influence of experimental conditions on morphology. These early experiments provided clear evidence that the ambient gas plays a critical role in the formation of sharp conical microstructures [1]. Surfaces irradiated in nitrogen, helium, or vacuum have much blunter structures than surfaces structured in sulfur hexafluoride or chlorine. Experiments were performed to determine the effect of laser parameters such as fluence, pulse duration, and polarization on surface morphology [11, 2]. These experiments were carried out in hopes of determining how the sharp, ordered structures are formed. However, determining the formation mechanism proved to be a formidable problem, which we continue to study today (see Chapter 3). After we reported on the formation of conical microstructures, a few other research groups took notice of the unique surface morphologies following laser irradiation in sulfur hexafluoride and began their own work on the subject [12, 13, 14, 15].

While the focus of these other groups has remained solely on unique surface morphologies [16, 17], our work changed significantly in 2000 because of another unique property of femtosecond-laser microstructured silicon. In addition to forming ordered, conical microstructures, laser irradiation transforms the originally grey, mirror-like surface of polished silicon into a dark, velvety black. The structured surface's deep black appearance led us

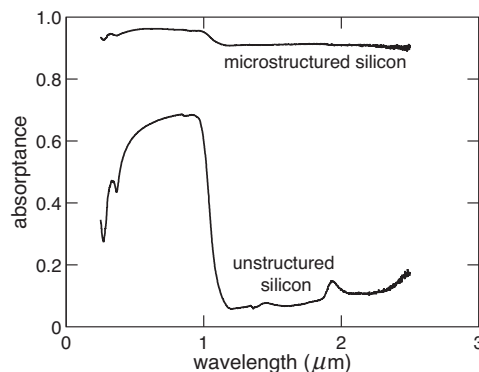


Figure 2.2: Absorbance of femtosecond-laser microstructured silicon as a function of wavelength. The absorbance of unstructured silicon is shown for reference. The large drop in absorbance of unstructured silicon at  $1.1 \mu\text{m}$  corresponds to the band gap energy of crystalline silicon.

to refer to it as "black silicon"<sup>1</sup>. The altered appearance of the surface indicated that the optical properties of the surface are modified during laser irradiation. In order to quantify the change, we measured the absorbance of a microstructured surface for wavelengths from the near-ultraviolet to the near-infrared [18, 19]. Figure 2.2 shows the absorbance of femtosecond-laser microstructured silicon as compared to unstructured silicon. Microstructured silicon has much higher absorbance across the entire spectrum, including near-unity absorbance at below-band gap wavelengths. The increased absorption in the visible is consistent with the black appearance, but high absorbance at wavelengths longer than  $1.1 \mu\text{m}$  was quite surprising. Because crystalline silicon has a band gap energy of  $1.07 \text{ eV}$ , absorbance in crystalline silicon drops precipitously for wavelengths longer than  $1.1 \mu\text{m}$  (shown in the absorbance measurement of unstructured silicon). Though an interesting result from a scientific point of view, the below-band gap absorbance also holds great promise for application in silicon based optoelectronics. At this point, the scope of our work expanded to include both investigating the formation mechanism and the source of

<sup>1</sup>In this dissertation, we refer to the irradiated surfaces as either femtosecond-laser microstructured silicon or, simply, microstructured silicon.

near-unity absorptance at below-band gap wavelengths [20] (see Chapter 4).

This dissertation contains a comprehensive review of our recent work on femtosecond-laser microstructured silicon. We present explanations of both the formation mechanism and the source of below-band gap absorption. In addition, the later chapters represent the latest significant change in our work over the last six years; using what we know about the structured surface, we transitioned from investigation to application and present novel optoelectronic devices made with femtosecond-laser microstructured silicon.

As electronic devices continue to get smaller, researchers are searching for novel ways of achieving small self-assembled active devices over large areas. Although still a very young field, the interaction of intense femtosecond laser pulses with semiconductor surfaces holds great promise. The extreme conditions at the focus of an intense femtosecond pulse give rise to new physics and material interactions. Also, under the proper conditions, short laser pulses can be used to create nanometer-scale self-ordered structures [17, 21]. The combination of self-ordering and unique material properties make femtosecond-laser structuring of semiconductors a valuable tool for future progress of microelectronic devices.

The preceding history, along with the following description of our experimental apparatus and procedures, lays the foundation for discussion of results presented in the remainder of this dissertation.

## 2.2 Apparatus and procedure

The procedure and apparatus for creating microstructured silicon has evolved since the original experiments [1]. Single crystal silicon wafers are cut to the desired size for each experiment, typically 10 mm x 10 mm squares. Each square is then cleaned with a fifteen minute ultrasonic bath in trichloroethylene, followed by a fifteen minute ultrasonic bath

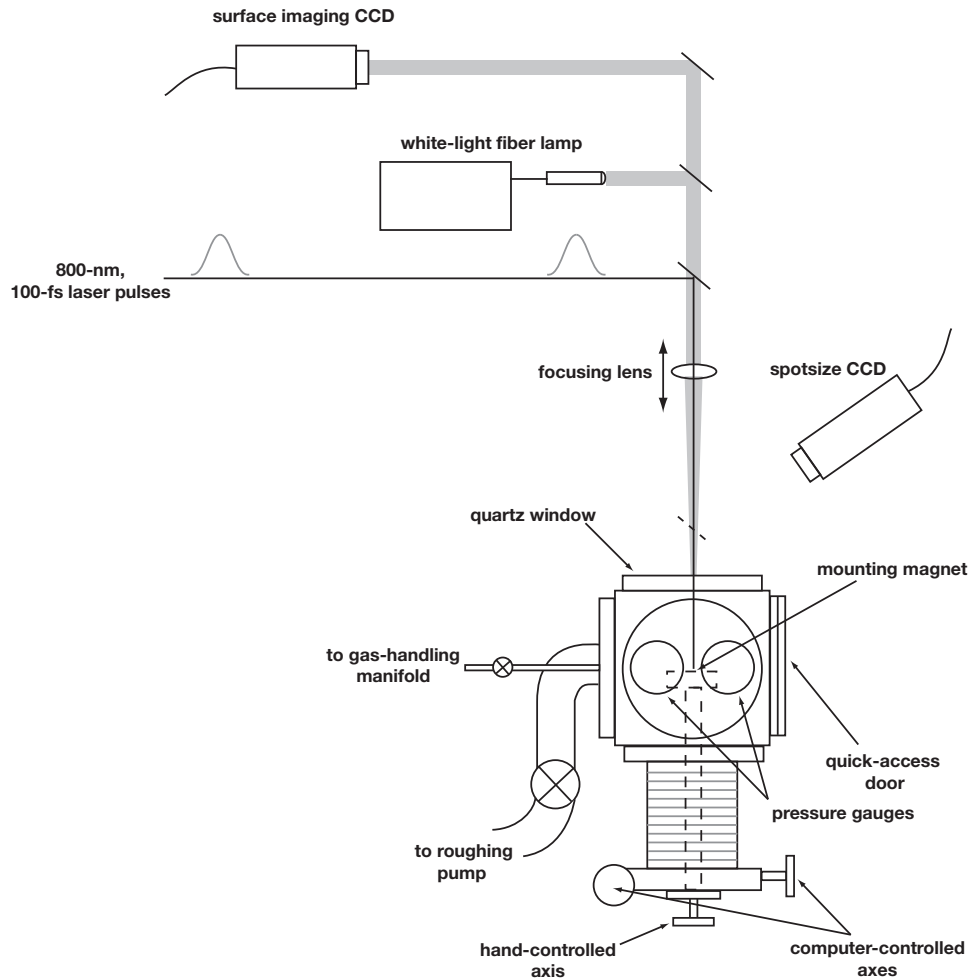


Figure 2.3: A schematic diagram of the apparatus used for microstructuring silicon with femtosecond laser pulses. Samples are loaded through the quick-access door and attached to the mounting magnet.

in acetone, and lastly a fifteen minute ultrasonic bath in methanol. After cleaning, the cut squares are left to soak in a methanol bath. At the time of microstructuring, squares are removed from the methanol bath and dried with a nitrogen gas flow. They are then attached (with carbon tape) to a magnetizable sample holder for mounting on a magnet inside the sample processing chamber.

The main piece of the sample processing chamber is a 4.5 inch stainless steel cube

with Conflat connections on each of the six sides. Attached to the back side of the cube is a three axis, precision motion controller from Thermionics<sup>TM</sup> vacuum products. This controller contains two orthogonal micrometer precision axes driven by computer controlled SilverMax<sup>TM</sup> motors. The third axis is hand controlled with 1 mil precision. The controller translates a one-inch diameter stainless steel rod which supports a 2" diameter mounting magnet in the center of the cube; samples attached to a magnetizable sample holder are attached to the mounting magnet. Attached to the bottom of the cube is a corrosive compatible, Edwards<sup>TM</sup> two-stage roughing pump that can evacuate the chamber to a base pressure of approximately  $10^{-3}$  torr. In order to monitor the chamber pressure, we use two pressure gauges. For measuring higher pressures (1 – 760 torr) we use an MKS<sup>TM</sup> Baratron capacitance manometer; for lower pressure ( $10^{-3}$  – 1 torr) we use a platinum coated Convectron gauge. Attached to one side of the chamber is a leak valve and stainless steel gas-handling manifold. The leak valve and manifold allow us to attach and admit up to five different background gases. An optical grade, 4.5 inch quartz window is attached to the front of the chamber to allow laser access. Lastly, a quick-access viewport door is attached to the remaining side. This door allows for rapid sample loading and removal as well as a means to observe the sample surface safely during microstructuring.

The laser used in the majority of our experiments is a regeneratively amplified, femtosecond Ti:sapphire system with a central wavelength of 800 nm. Femtosecond laser pulses are generated with a Kapteyn-Murnane<sup>TM</sup> kit pumped by a 5-W Coherent<sup>TM</sup> Verdi diode laser. The femtosecond pulses are regeneratively amplified in a second Ti:sapphire crystal that is pumped by a Quantronix<sup>TM</sup> YLF nanosecond laser. Following amplification, the laser pulses are approximately 100 fs, have a center wavelength of 800 nm, and are at a repetition rate of 1 kHz. Further details of this laser system are described elsewhere [22, 23, 2].

The laser is focused through the quartz window and onto the sample surface using a 250-mm focal length, anti-reflection coated, plano-convex lens. The lens is mounted on a single axis linear translation stage and positioned such that the focal point is behind the sample. By moving the lens, and therefore the position of the focus, we can vary the laser spot size at the sample surface from a diameter of 30  $\mu\text{m}$  to 250  $\mu\text{m}$ . In order to measure the spot size, we place a CCD (Charge-Coupled Device) camera at the exact same optical distance (from the lens) as the sample surface. A flipper mounted mirror redirects the laser beam onto the camera and we determine the spot size on the sample surface from the measured spot size on the camera. We image white-light reflected off of the sample surface with a second CCD camera in order to monitor progress during microstructuring.

Samples attached to a magnetizable sample holder are loaded through the access door and attached to the mounting magnet. Samples are then positioned in the center of the magnet to allow for maximum translation. The chamber is evacuated to a base pressure of  $10^{-3}$  torr and then filled to the desired pressure with an ambient gas (typically 0.67 bar of sulfur hexafluoride). The sample is then irradiated with a 1-kHz train of 100-femtosecond, 800-nm laser pulses. The fluence of each pulse is set by picking a spot size (typically 150  $\mu\text{m}$ ) and using a waveplate/polarizing cube combination to vary the pulse energy. We can irradiate either a single spot or use the motion controller to translate the sample relative to the laser beam. If translated, the sample is moved in a simple raster scan pattern. We can pattern square areas up to 20 mm x 20 mm. By using a shutter and varying the horizontal translation speed, the average number of pulses hitting a given spot on the sample can be controlled. Following irradiation, the chamber is evacuated and purged with nitrogen gas. The chamber is then brought up to atmosphere, samples are removed via the access-door, and the optical access window is cleaned to remove material that may have stuck to it during microstructuring. The resulting morphology and optical properties depend heavily on the

parameters of the experiment, including shot number, fluence, pulse duration, ambient gas species, ambient gas pressure, and laser wavelength.

## Chapter 3

# Morphology and chemical composition

The experimental procedure for femtosecond-laser microstructuring silicon involves several variable parameters. Among these parameters are the number of incident laser pulses, the laser fluence, wavelength, pulse duration, ambient gas species and pressure, substrate doping and crystalline orientation, and annealing temperature. We examine the extent to which these parameters affect the final morphology and chemical composition of the microstructured surface. This analysis sheds light on formation mechanisms responsible for the unique microstructures.

The quasi-ordered array of microstructures shown in Chapter 2 (Figure 2.1) are made with the following experimental conditions: irradiation of an *n*-doped silicon wafer (*n*-Si(111), 260  $\mu\text{m}$  thick, resistivity  $\rho = 8 - 12 \Omega\cdot\text{m}$ ) with an average of 500 laser pulses (100 fs, central wavelength 800 nm, fluence 8  $\text{kJ}/\text{m}^2$ ) in 0.67 bar of  $\text{SF}_6$ . For historical reasons we choose these as our standard conditions. We vary the aforementioned parameters and employ microscopy and chemical measurements to monitor changes in the surface

morphology and composition.

## 3.1 Effect of shot number

In this section we investigate how the surface morphology and chemical composition evolves with increasing number of pulses; all other parameters are kept at standard conditions.

### 3.1.1 Surface morphology

Figure 3.1 shows the surface evolution with increasing numbers of pulses, from 1 to 600. Each scanning electron micrograph (SEM) shows a different irradiated spot; the micrographs are not taken of the same spot in between pulses. Over the course of several hundred laser pulses, the quasi-ordered array of microstructures forms without the use a mask. We discuss the formation of conical microstructures in two parts: the early formation stage (for pulses one to ten) and late stage formation (for pulses 10 and up).

#### Early stage

Following the first laser pulse, small defects appear that are randomly scattered across the irradiated area. These defects resemble a burst bubble of molten silicon with a circular ripple pattern surrounding some of the larger defects. They are likely the result of instabilities in temperature of the molten surface at a defect or impurity.

With the second pulse, a distinct, regular ripple pattern appears on the surface. The ripples occur at a wavelength close to the central wavelength of the laser light and their long axis is perpendicular to the laser polarization. The ripple formation is a well-understood phenomenon termed Laser Induced Periodic Surface Structures (LIPSS) [5, 3, 4]. In this fluence regime, the ripples are the result of capillary waves excited in molten silicon

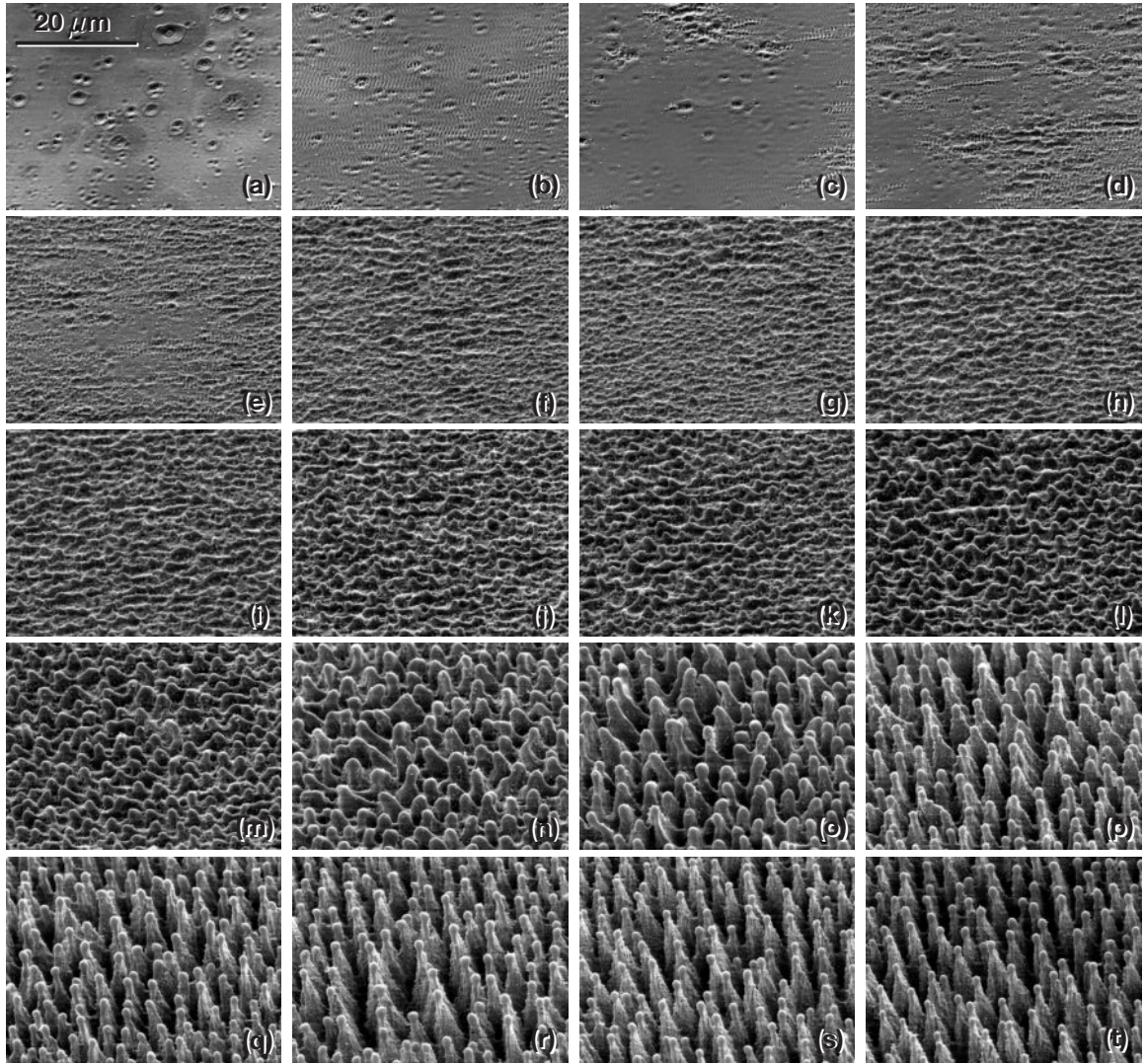


Figure 3.1: Scanning electron micrographs of a silicon surface after (a) 1, (b) 2, (c) 3, (d) 4, (e) 5, (f) 6, (g) 7, (h) 8, (i) 9, (j) 10, (k) 12, (l) 15, (m) 20, (n) 30, (o) 50, (p) 70, (q) 100, (r) 200, (s) 400, and (t) 600 laser pulses. Each SEM is taken at a  $45^\circ$  angle to the surface with the same magnification.

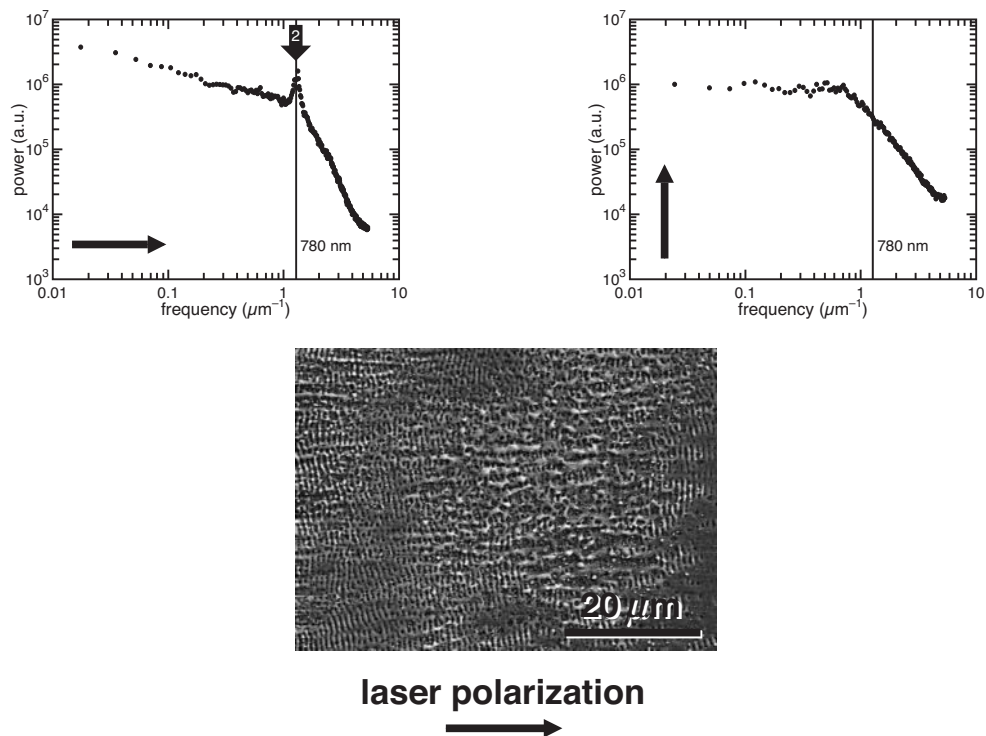


Figure 3.2: Fourier analysis of line-outs taken in the vertical and horizontal direction of a silicon surface after 2 laser pulses. The scanning electron micrograph is taken normal to the surface.

through interference between the incident and scattered laser light [24, 25]. We analyze the periodicity of patterns, like the ripples, with Fourier transforms of scanning electron micrographs for both the vertical and horizontal directions. Figure 3.2 shows the Fourier analysis of a surface after 2 laser pulses. The horizontal direction shows a strong peak at a frequency corresponding to the ripple period. There is no visible pattern in the vertical direction and, likewise, there is no peak in the Fourier power spectrum.

During pulses 3, 4 and 5 the morphology transitions from laser induced periodic surface structures to a stage in the formation process that is not well understood. In this second stage, the ripples begin to coarsen and “bead-up” along their long axis. The peak that appears in the horizontal Fourier power spectrum (after two pulses) diminishes; there is

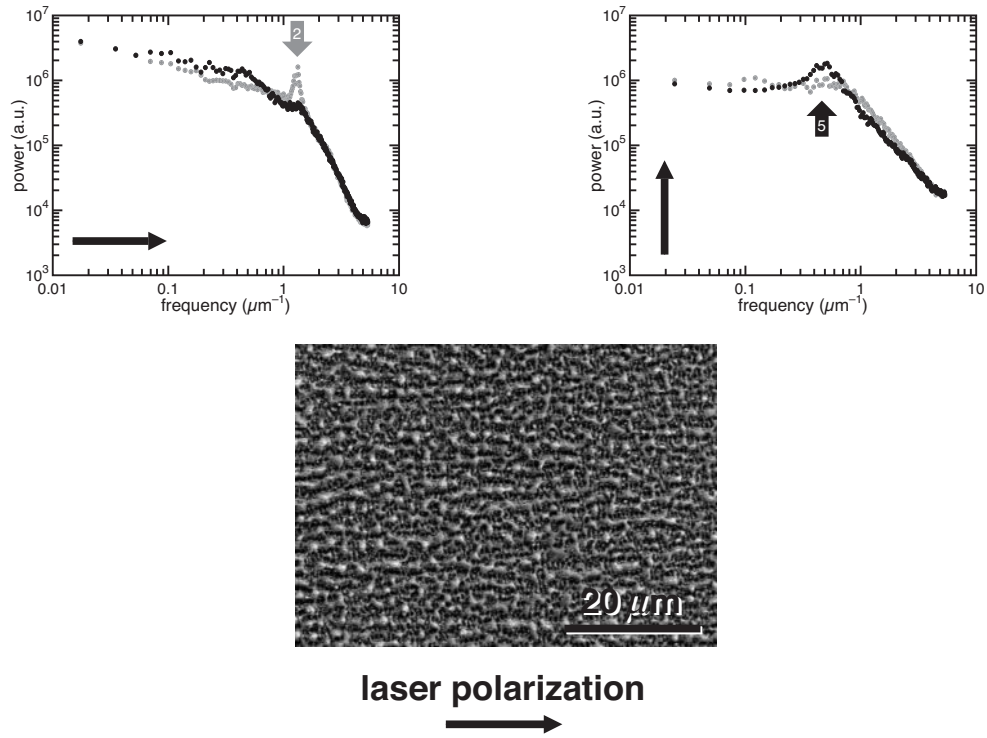


Figure 3.3: Fourier analysis of line-outs taken in the vertical and horizontal direction of a silicon surface after 5 laser pulses. The scanning electron micrograph is taken normal to the surface.

no longer a distinguishable surface pattern in the horizontal direction. However, the beads that form from the ripples are spaced by about  $2 \mu\text{m}$ , parallel to the laser polarization; their spacing leads to a peak in the vertical direction of the Fourier power spectrum. Figure 3.3 shows the Fourier analysis after five incident pulses.

For pulses 5 to 10, the peak in the vertical direction grows and shifts toward slightly smaller frequencies (larger spacing). After the tenth pulse, the peak of this feature is at a frequency corresponding to a bead spacing of about  $3.5 \mu\text{m}$ . In addition, a peak in the Fourier signal is beginning to appear in the horizontal direction. Figure 3.4 shows the Fourier analysis of the surface after ten incident pulses. At this point the characteristic wavelengths/spacings for the final microstructures are set. This marks the end of the early

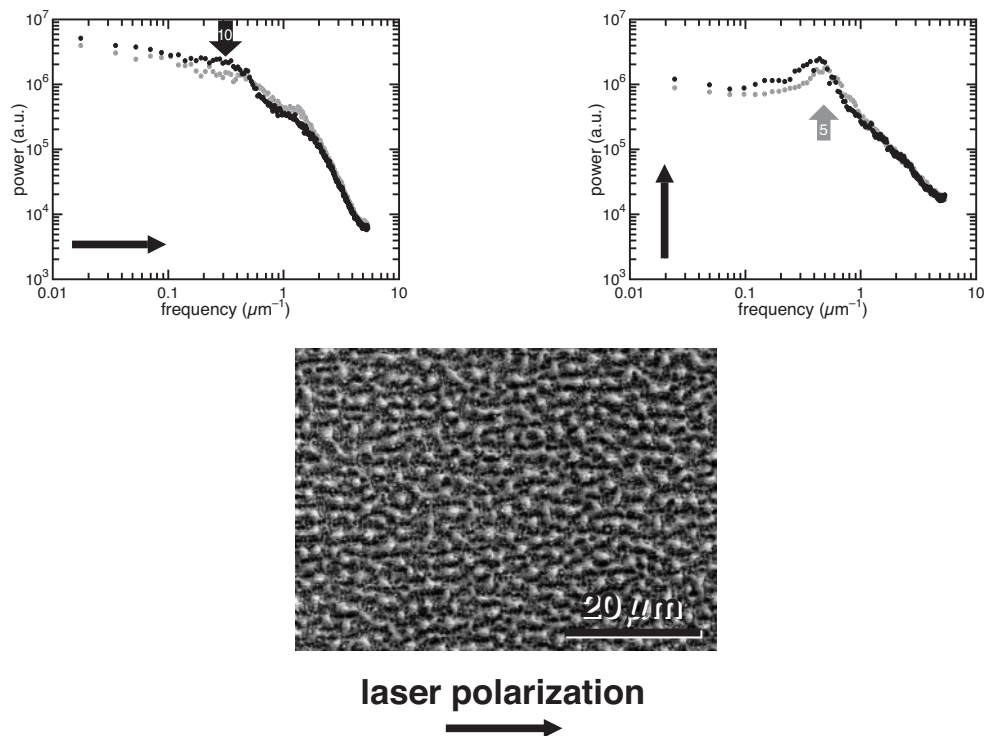


Figure 3.4: Fourier analysis of line-outs taken in the vertical and horizontal direction of a silicon surface after 10 laser pulses. The scanning electron micrograph is taken normal to the surface.

stage of formation.

To summarize, during the early stage of formation we see three important patterns emerge at different pulse numbers. A ripple pattern at the wavelength of the laser forms after the second pulse, with the ripples' long axis perpendicular to the laser polarization. After the fifth pulse, the ripple pattern coarsens significantly and beads begin to form along the ripples at a spacing larger than the wavelength of the laser. By the tenth pulse, the beads become more pronounced and a characteristic spacing for both the vertical and horizontal directions emerges. What causes the transition from the one-dimensional ripple pattern to the two-dimensional pattern of beads is not clear. We speculate that the spacing and size of the beads depends strongly on capillary waves and surface tension, which are in

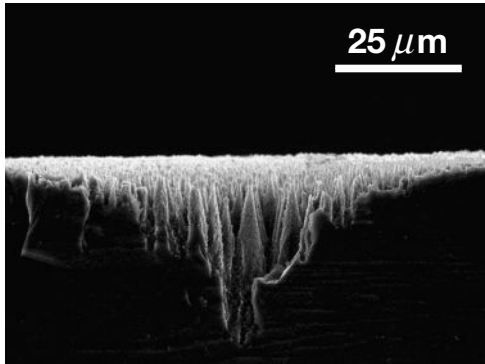


Figure 3.5: A sideview of a microstructured silicon sample, cleaved through an irradiated spot. The tips of the microstructures are all at or below the original wafer surface.

turn influenced by impurities in the surface layer, melt depth, and temperature. We will see later in this chapter that these characteristic spacings and morphology depend heavily on other parameters such as ambient gas and fluence.

### Late stage

At the end of the early formation stage, a two-dimensional pattern of beads emerges (Figure 3.4). This pattern remains in essentially the same arrangement throughout the entire late stage formation. From pulse ten to several hundred pulses, the final conical microstructures are etched out of the surface, with the beads ending up as the peaks of the cones. Incident laser pulses preferentially remove material to the sides of the beads, leaving the conical structures behind. Figure 3.5 shows that the tips of all microstructures are at or below the surface of the original silicon wafer and that the conical structures are etched out rather than grown.

During late stage formation, the beads serve two purposes. First, they act as protective caps from the incident laser energy. The reason for the beads resilience is not well known. However, in similar conical structures formed during ion sputtering, concentrations

of impurity atoms seed cone growth and protect regions of the substrate; implanted impurity atoms lower the sputter yield, thus seeding cone placement and growth [26]. Another example of conical structures are naturally formed snow structures called *penitentes* that form on glaciers or snow fields at high altitudes. For these structures, which resemble meter-scale versions of silicon conical microstructures, higher dirt concentration at the tips reduces melting at the peaks relative to the "cleaner" snow to the sides of the peaks [27]. Likewise, impurity atom implantation during laser irradiation might reduce ablation rates from the beads and is a likely reason for their resilience.

The second effect of the beads is to concentrate laser light into the valleys between the beads. Briefly, incoming photons that strike the side of the beads have a higher incident angle than those that hit the top of the bead. Because reflectivity is high at large incident angles, a majority of the light striking the side of the beads reflects off and is absorbed in the pits where it strikes at an angle closer to normal [18]. An increase in absorbed light raises the energy concentration within the pits and results in more material ablation and preferential etching inside the pits. This effect becomes more pronounced as the beads sharpen into microstructures and the angles of the sides become steeper.

In the late stage of formation, there is little change in the spacing of the surface pattern. The spacings in the horizontal and vertical direction move to slightly longer wavelengths as the microstructures are etched from the surface. A final Fourier analysis of the surface after 500 incident pulses is shown in Figure 3.6. The average spacing of the microstructures is about 3-4  $\mu\text{m}$  in the direction both perpendicular and parallel to the laser polarization.

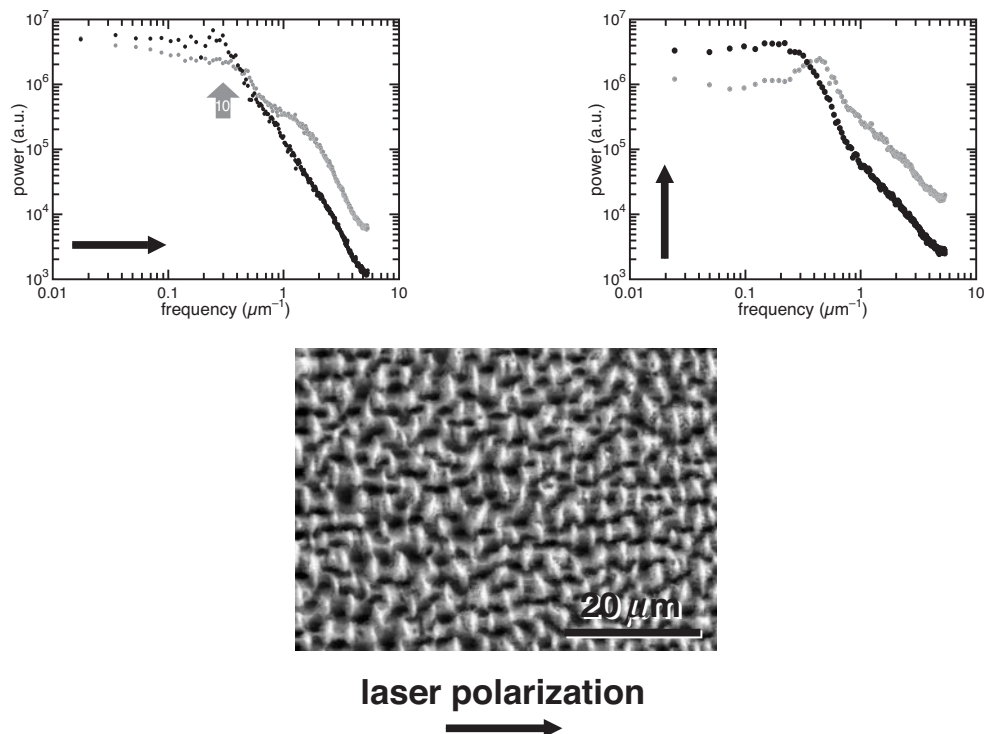


Figure 3.6: Fourier analysis of line-outs taken in the vertical and horizontal direction of a silicon surface after 500 laser pulses. The scanning electron micrograph is taken normal to the surface.

### 3.1.2 Surface layer structure and composition

After discussing the morphology of the surface on a micrometer scale, we now take a closer look and examine chemical composition and nanometer scale structure of the surface.

#### Surface layer structure

In addition to scanning electron micrographs of the surface, we performed bright-field transmission electron microscopy (TEM) on cross-sections prepared from samples after 10 and 500 laser pulses. These micrographs are shown in Figure 3.7<sup>1</sup>. Visual examination

<sup>1</sup>TEM sample preparation, micrographs, and x-ray analysis were provided by M. Wall and Dr. F. Génin from Lawrence Livermore National Laboratory

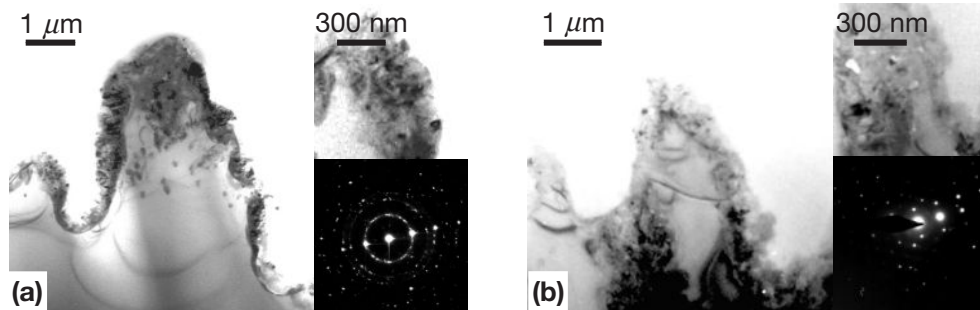


Figure 3.7: Transmission electron micrographs of the surface after (a) 500 and (b) 10 pulses. The disordered surface layer of both samples is similar in thickness and structure. Insets: (upper) high-magnification view of the disordered region at the tip of the microstructure and (lower) selected area electron diffraction pattern obtained from the disordered region.

indicates that (for both samples) there is a disordered layer that is several hundred nanometers thick and made up of nanocrystallites ( $\sim 10\text{--}50$  nm in diameter) and nanopores. The disordered surface layer after 10 pulses is similar to that for 500 pulses, despite much smaller conical microstructures. Although we do not have transmission electron micrographs for other pulse numbers, the fact that the surface layer formed with just 10 pulses is similar in both thickness and structure to that formed with 500 pulses suggests that the surface layer may reform with each laser pulse once the pattern of microstructures is established.

Selected area diffraction (SAD) indicates that for both samples, the surface layer (insets to Figure 3.7) has significant crystalline order. It is also possible that amorphous-like material is present between nanocrystalline grains. Research has shown that the structure of the intergranular phase in nanocrystalline silicon is similar to that of bulk amorphous silicon [28] and amorphous material has long been observed following short pulsed laser irradiation [29, 30]. Selected area diffraction indicates that the substrate below the disordered layer is undisturbed crystalline silicon.

## Chemical composition

To determine the effect of shot number on chemical composition we employed Rutherford backscattering spectrometry (RBS) [31] and energy dispersive X-ray (EDX) [32] emission spectroscopy. As a rough gauge, EDX measurements indicate that there is a large amount of sulfur ( $\sim 1$  at. %) in the disordered surface layer and no measurable amount of impurity species in the crystalline silicon beneath. We used RBS to make more precise measurements of the chemical composition in the surface layer. We measured the backscattering spectrum from 2.0-MeV alpha particles collected with an annular solid state detector. To determine the chemical composition of the microstructured material, we compared the measured RBS spectra to simulated spectra [33] from planar material. The spectra measure only the average sulfur concentration in the uppermost 100 nm of the surface; the RBS signal from deeper sulfur is masked by the silicon signal. However, because EDX indicates that there are no chemical changes below the structurally modified layer, we simulate only the top layer to determine sulfur concentrations. RBS spectra indicate that the modified surface layer consists of oxidized silicon with fluorine and sulfur impurities; etching the samples in 5% HF for 4 minutes removes the fluorine and the oxide without changing the sulfur concentration. To simplify simulation of the spectra, we took RBS spectra for samples etched in HF<sup>2</sup>. These measurements show that the concentration of sulfur increases with increasing shot number up to about 50 pulses. The amount of sulfur increases from roughly 0.2 at. % for the sample made with two pulses to roughly 0.7 at. % for the sample made with 50 pulses. Additional pulses have little effect; the sample made with 500 pulses also has 0.7 at. % sulfur. These results are summarized as a part of Table 3.1 near the end of the chapter.

---

<sup>2</sup>The conditions and considerations for RBS measurements is true for all RBS data presented in this dissertation

## 3.2 Spot samples *vs.* translated samples

Before moving on to other parameters that affect morphology, we discuss a subtlety of the experimental process. As mentioned in the experimental procedure section (Section 2.2), we make samples in two ways: we either leave a sample stationary and irradiate a single spot, or translate the substrate relative to the laser beam in order to structure larger areas. With the rest of the experimental parameters left the same, there are two visible differences between translated and stationary samples. The first is that the microstructures in the stationary samples have a micrometer-sized sphere at the tip while the translated samples are sharper and lack the sphere at the tip. The second is that translated samples have a larger amount of nanoscale particles spread across the surface. An extreme example of these two differences is shown in Figure 3.8. The left frame shows microstructures from a stationary sample and the right shows those made while translating the sample relative to the laser beam. The left frame has fewer nanoscale particulates on the surface and much larger, rounder tips (some of the scanning electron micrographs in this chapter are from stationary samples and some are from translated samples).

The nanoscale particles on translated samples are redeposited material from the ejected plume. For each irradiated spot there is a ring of material around the spot. On a stationary sample all of this debris lies away from the area where microstructures form. However, on a translated sample, the debris from other irradiated regions lands back in previously irradiated regions. The density of nanoscale material varies a great deal along the surface of a translated sample and there is no recognizable pattern to the variation in concentration. In addition, many of these particles can be washed off in a brief ultrasonic methanol bath.

The reason for the presence or lack of spheres at the tip is a little harder to

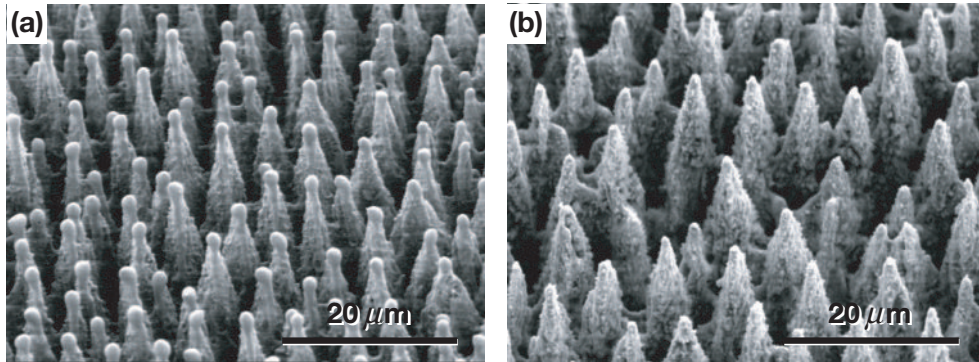


Figure 3.8: Scanning electron micrographs of (a) a stationary sample and (b) a translated sample. The stationary sample has spherical ball tips while the translated sample has sharper tips and more nanoscale debris along the surface.

determine than the presence of nanometer-scale particles. The spherical tips have been observed previously on nanosecond laser formed microstructures and are explained as a resolidified molten droplet of silicon [7, 8, 10]. In addition to the spherical tips, other groups observe microstructure growth above the original substrate surface. These research groups contend that no significant build-up can occur from material “climbing” the sides of the microstructure and that the material at the tip must be redeposited ablated material from the silicon rich plume above the molten surface [10]. The spherical tips of our silicon microstructures are most likely resolidified droplets of redeposited silicon.

However, redeposition does not explain why the spherical balls are only present for stationary samples. We speculate that the varying fluence at each point on the surface during translation melts the spherical ball tips. Under our standard conditions, a single spot on the surface is irradiated with approximately 500 laser pulses. However, the intensity of these pulses is not constant as the Gaussian profile of the beam passes over a spot. That is, a given spot on the surface is first struck by the leading edge of the gaussian beam, which is at a lower fluence than the center of the beam. The higher fluences of the beam center

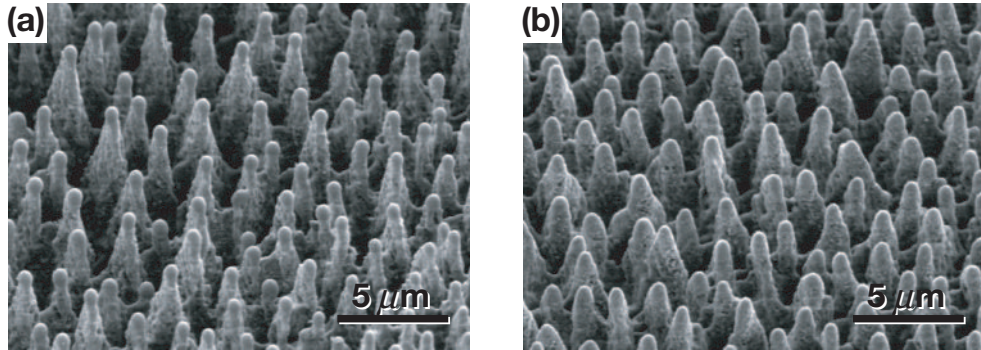


Figure 3.9: Scanning electron micrographs of (a) a single spot irradiated with 500 laser pulses under standard conditions and (b) a single spot irradiated under the same conditions as (a), but with the energy of each pulse varied to simulate the gaussian profile of the laser as it passes over the surface during translation. The spherical balls at the tips disappear with varying the energy of each pulse.

then pass over the spot, but, as the trailing edge passes over, the spot is again exposed to lower fluence irradiation. If a spot is exposed to fluences below the ablation threshold but above the melting threshold, the spherical tips melt, flow, and wet the sides of the conical microstructures. In addition, no material is available for redeposition at the tips because no ablation occurs.

To test this hypothesis, we simulated the changing fluences for a translated sample by leaving the sample stationary but varying the fluence of each incident pulse. To do this we used a low pulse repetition rate and a variable neutral density filter to adjust the power of each pulse and simulate an increasing and then decreasing fluence. We matched the highest fluence of the filtered pulses to match the fluence of pulses at our standard conditions. The results are shown in Figure 3.9. The spherical tips do indeed disappear. In fact, if the experiment is carried out by simply decreasing the fluence with each pulse, we see the same results.

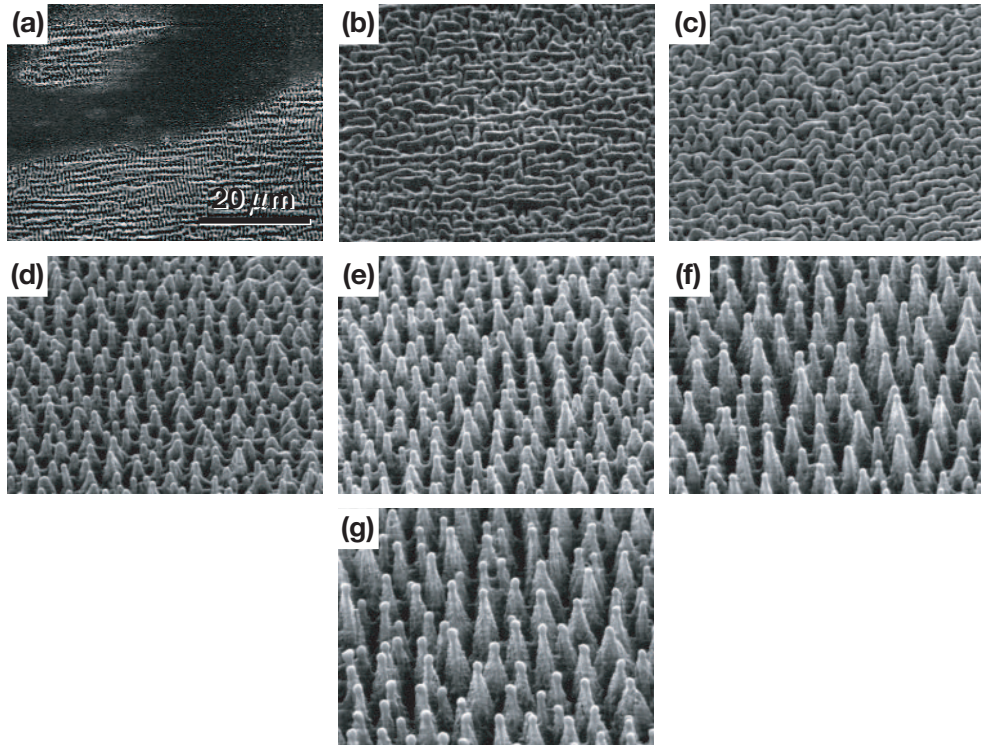


Figure 3.10: Scanning electron micrographs of a silicon surface after irradiation with laser pulses of fluence (a)  $2 \text{ kJ/m}^2$ , (b)  $3 \text{ kJ/m}^2$ , (c)  $4 \text{ kJ/m}^2$ , (d)  $5 \text{ kJ/m}^2$ , (e)  $6 \text{ kJ/m}^2$ , (f)  $7 \text{ kJ/m}^2$ , and (g)  $8 \text{ kJ/m}^2$ . Each SEM is taken at a  $45^\circ$  angle to the surface with the same magnification.

### 3.3 Effect of fluence

The final morphology also greatly depends on the fluence of the incident laser pulses. In this section we examine morphology at different fluences while keeping all other experimental parameters at our standard conditions.

#### 3.3.1 Surface morphology

Figure 3.10 shows the variation in surface morphology for average fluence from  $2 \text{ kJ/m}^2$  to  $8 \text{ kJ/m}^2$ . The change in morphology with increasing fluence strongly resembles the stages of development seen with increasing shot number (Figure 3.1). With increasing

fluence (at constant shot number) the morphology goes from laser induced periodic surface structures, to a coarsened surface, to the sharp microstructures of our standard conditions.

At an average fluence of  $2 \text{ kJ/m}^2$  the surface is altered in sporadic patches and the damage that occurs resembles laser induced periodic surface structures. At this fluence the laser is only melting the surface and no ultrafast melting or ablation occurs [34]. Some of the surface remains undisturbed because this average fluence is just above the threshold fluence for melting ( $1.5 \text{ kJ/m}^2$ ). Continued irradiation at this fluence does not result in development of sharp, conical microstructures. At a fluence of  $3 \text{ kJ/m}^2$ , the surface is covered by a coarsened ripple pattern with spacings longer than the wavelength of the laser light. This fluence is above the ultrafast melting threshold and very close to the ablation threshold for silicon ( $3.1 \text{ kJ/m}^2$ ) [34]. Continued irradiation at this fluence does not result in development of sharp, conical microstructures. At a fluence of  $4 \text{ kJ/m}^2$ , the morphology resembles the surface after 15 laser pulses in the shot number series (Figure 3.1). With continued irradiation at this fluence, conical microstructures *do* develop. As we continue to increase the fluence from 5 to  $8 \text{ kJ/m}^2$ , the changes in morphology resemble the progression from tens of laser pulses to 500 pulses. For fluences above  $8 \text{ kJ/m}^2$  (up to  $12 \text{ kJ/m}^2$ ), the surface morphology looks very similar to the  $8 \text{ kJ/m}^2$  samples with a small increase in microstructure height and a thinning of the cone body. At very high fluences ( $>12 \text{ kJ/m}^2$ ), many times the ablation threshold fluence, material removal becomes extreme and instead of conical structures, we make a gaussian shaped hole in the surface. These high fluences are often used for fast machining and cutting of silicon because a large amount of material is removed with each pulse [35].

An important trend to notice in Figure 3.10 is that, with increasing fluence, there is an increase in both the microstructure height and distance between microstructures. These

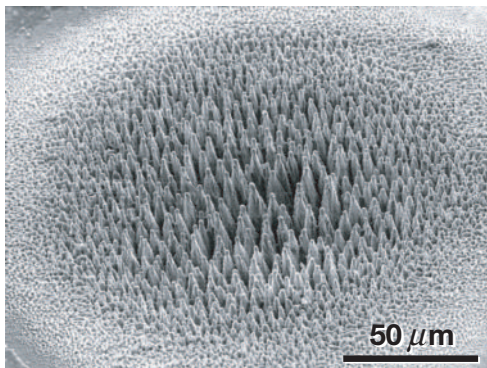


Figure 3.11: A scanning electron micrograph of (a) a single spot irradiated at a fluence of  $10 \text{ kJ/m}^2$ . From the gaussian fluence profile, the different morphologies that occur can be seen in a single spot.

two dimensions are, in fact, correlated according to

$$h \propto d^{2.4 \pm 0.1} \quad (3.1)$$

with microstructure height  $h$ , and separation distance  $d$  [11]. Perhaps the clearest illustration of how fluence affects the morphology of the surface is to look at an entire irradiated spot at  $10 \text{ kJ/m}^2$  (Figure 3.11). One can see all the different morphologies from ripples at the edge to tall conical structures in the center, showing the gaussian fluence profile of the laser beam.

As an aside, if we take a look at the surface at the low end of the tested fluences ( $2 \text{ kJ/m}^2$ ), there are some interesting surface morphologies to note. As we see in Figure 3.10 (a), the surface is altered in sporadic patches; some of the surface appears unchanged. Upon closer examination of areas that appear unchanged, we find regions of ordered silicon islands that are about 10-nm in diameter (Figure 3.12). Similar ordering of nanostructures has been observed by other researchers [16] and are likely the result of scattering from dust particles on the surface. We have not rigorously analyzed this behavior, but we may investigate these morphologies further because self-ordering of nanometer-scale structures

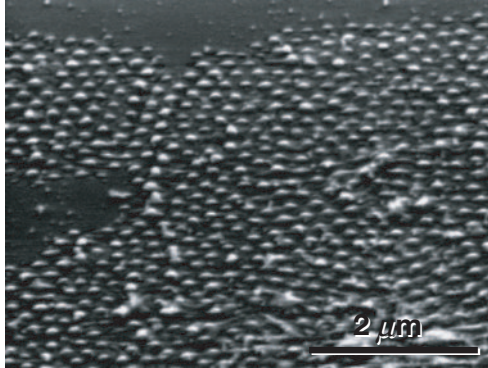


Figure 3.12: Nanometer scale self-ordered silicon islands formed at low fluence ( $2 \text{ kJ/m}^2$ ).

is an active area of research.

### 3.3.2 Surface layer structure and composition

In addition to the micrometer-scale morphology, we take a closer look at the nanoscale structure and chemical composition of the surface for different fluences.

#### Surface layer structure

Figure 3.13 shows transmission electron micrographs of samples made with fluence  $4 \text{ kJ/m}^2$  and  $8 \text{ kJ/m}^2$ . As was the case for shot number, the surface layer for both fluence samples are similar despite differences in microstructure size. Both have a several hundred nanometer thick, disordered surface layer, made up of nano-crystallites ( $\sim 10\text{--}50 \text{ nm}$  in diameter) and nanopores. Selected area diffraction indicates that for both fluences, the surface layer (insets to Figure 3.13) has significant crystalline order with a strong possibility that amorphous-like material is present between the nanocrystalline grains (see Section 3.1.2).

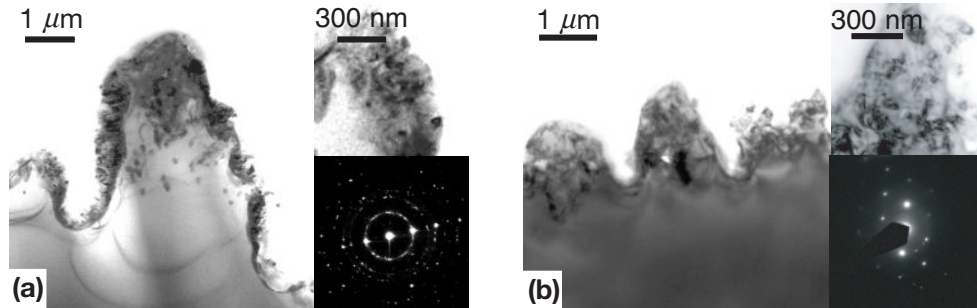


Figure 3.13: Transmission electron micrographs of samples made with (a) 8 kJ/m<sup>2</sup> and (b) 4 kJ/m<sup>2</sup>. The disordered surface layer of both samples is similar in thickness and structure. Insets: (upper) high-magnification view of the disordered region at the tip of the microstructure and (lower) selected area electron diffraction pattern obtained from the disordered region.

### Chemical composition

To determine the effect of fluence on chemical composition we employ the tools listed in section 3.1.2. Rutherford backscattering spectrometry (RBS) indicates that the concentration of sulfur increases with increasing fluence. The amount of sulfur increases from roughly 0.3 at. % for a sample made with 2.5 kJ/m<sup>2</sup> to roughly 0.7 at. % for the sample made with 8 kJ/m<sup>2</sup> pulses. Higher fluences do not increase the concentration significantly; samples made with 10 kJ/m<sup>2</sup> pulses also have 0.7 at. % sulfur. These results are summarized as a part of Table 3.1 near the end of the chapter.

## 3.4 Effect of pulse duration

Varying the duration of the pulse from femtoseconds to nanoseconds changes the overall size and shape of the microstructures. In this section we examine morphology of microstructures for nanosecond and femtosecond pulses. We also comment on the effect of a less drastic change in pulse duration through poor compression of a spectrally dispersed femtosecond pulse.

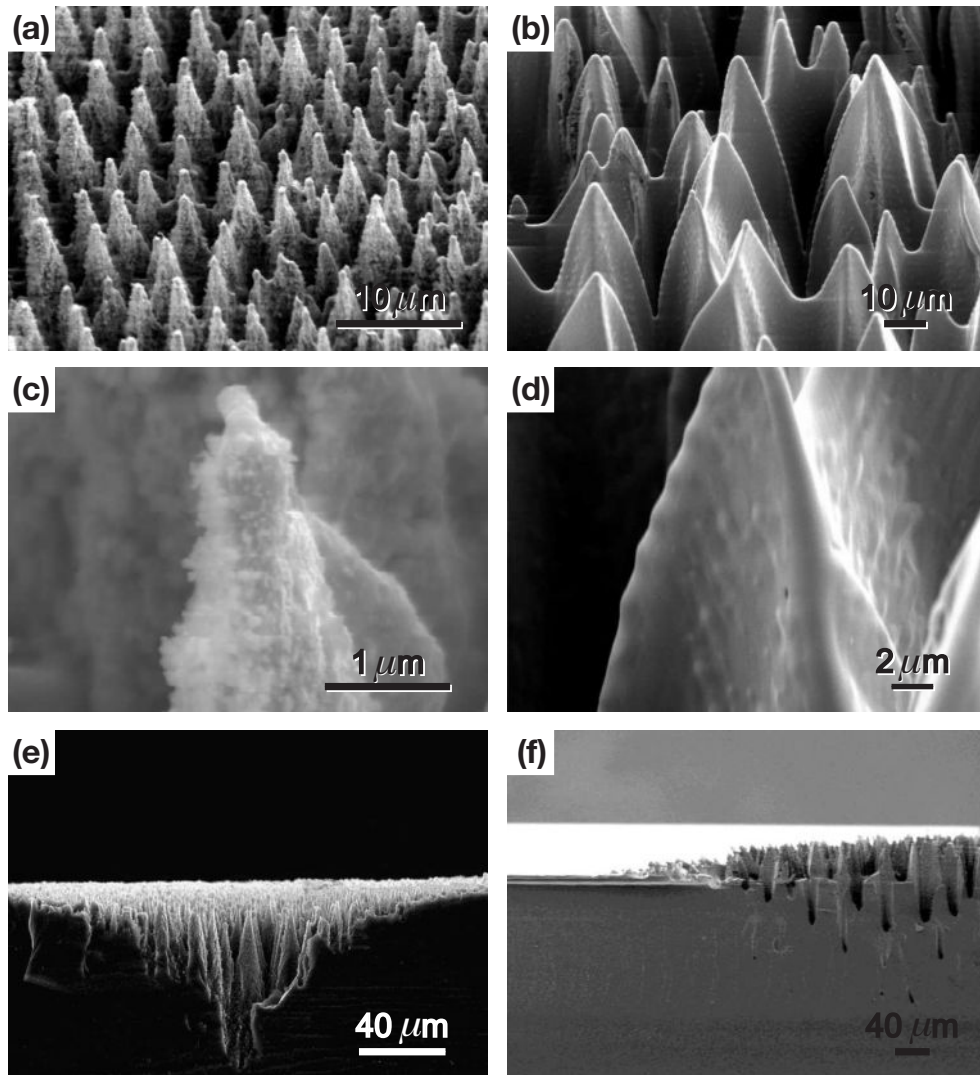


Figure 3.14: Scanning electron micrographs comparing surface morphology for two different pulse durations. ((a), (c), (e)) show microstructures made with 100-fs pulses and ((b), (d), (f)) show microstructures made with 30-ns laser pulses.

### 3.4.1 Surface morphology

The conditions used for creating nanosecond-laser-formed structures were matched with the initial work and conditions of Perdraza *et al.* [10]. A KrF+ excimer laser delivered a train of 248-nm, 30-ns laser pulses with a flat-top spatial profile and a fluence of 30 kJ/m<sup>2</sup>

onto a sample in a vacuum chamber filled with 1 bar of SF<sub>6</sub>. Pedraza *et al.* found that about 1500 laser pulses produce fully-formed conical structures, so we used an average of 1500 pulses per spot.

Figure 3.14 shows the results for the nanosecond-laser-formed microstructures as compared to femtosecond-laser-formed microstructures. In both cases, the microstructures are roughly conical, but the structures formed with the femtosecond laser ((a), (c), (e)) are one-fifth the size of those formed with the nanosecond laser ((b), (d), (f)). The femtosecond-formed structures are roughly 8  $\mu\text{m}$  tall and separated by 4  $\mu\text{m}$ ; the nanosecond-formed structures are roughly 40  $\mu\text{m}$  tall and separated by 20  $\mu\text{m}$ . Again, the tips of the femtosecond-formed structures are at the level of the original surface of the wafer (e), while the nanosecond-formed structures protrude above the original surface (f). Finally, the femtosecond-formed structures are covered with nanoparticles 10–50 nm in diameter deposited on the structures during fabrication (Figure 3.14 (c)), while the surface of the nanosecond-formed structures is much smoother, with 500 nm-size protrusions that appear to grow out of the surface (Figure 3.14 (d))<sup>3</sup>.

We have also examined the effect of increasing the duration of our femtosecond laser pulses from 100 femtoseconds to 10 picoseconds by changing the compression of a spectrally dispersed femtosecond pulse [11]. In this work, the separation between microstructures is plotted as a function of pulse duration (Figure 3.15), but separation distance is related to the height by Formula 3.1. For increasing pulse duration, the microstructure separation decreases from 100 femtoseconds to 5 picoseconds but then begins to increase again. The transition at 5 ps duration might be the point at which microstructures switch from being below the surface to growing above like the nanosecond-formed-microstructures

---

<sup>3</sup>Changing the pulse duration has a drastic effect on the morphology. However, other parameters were changed in the above experiment (pressure, wavelength, fluence). From examining the effects of varying these parameters in this chapter we are confident that it is the pulse duration that causes the morphological differences shown in Figure 3.14.

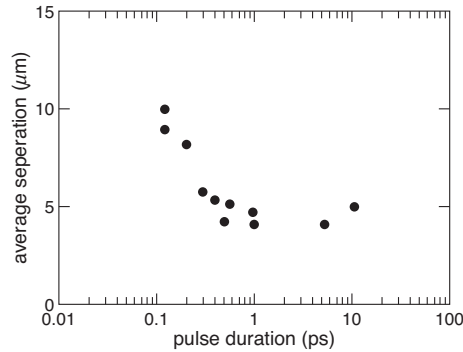


Figure 3.15: Average microstructure separation as a function of pulse duration. Separation distance is correlated to average microstructure height. Adapted from [11].

shown in Figure 3.14.

### 3.4.2 Surface layer structure and composition

The large difference in micrometer-scale morphology indicates a large difference in the formation process for nanosecond pulses and femtosecond pulses. We examine the nanoscale structure and chemical composition to see if there are also large differences in these characteristics.

#### Surface layer structure

Figure 3.16 shows transmission electron micrographs for a femtosecond-laser-formed sample and a nanosecond-laser-formed sample. Again, with the femtosecond-formed structures, there is a highly disordered layer of silicon a few hundred nanometers thick, made up of nanocrystallites and nanopores. Selected area diffraction (SAD) indicates that the core is crystalline and the surface layer is polycrystalline or microcrystalline (upper inset to (a)). The nanosecond-formed structures likewise have a crystalline core, but the disordered layer is thinner (150 nm or less) and covers only parts of the structures; the tips of

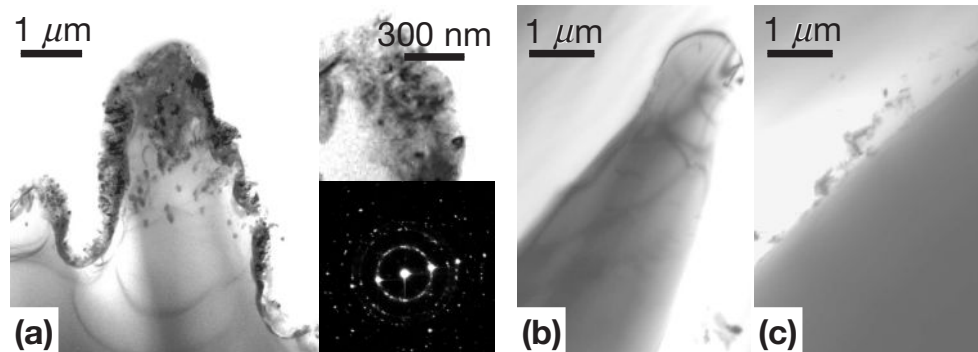


Figure 3.16: Comparison of transmission electron micrographs of (a) cross-section of femtosecond-laser-formed microstructure (insets: (upper) higher magnification view of disordered material, (lower) selected area electron diffraction pattern obtained from the tip of the sample); (b) cross-section of tip of nanosecond-laser-formed microstructure; and (c) cross-section of side of nanosecond-laser-formed microstructure. The disordered layer on the nanosecond-formed microstructures is too thin to take a selected area diffraction pattern.

the structures are single crystal and free of extended defects. Although the bases of the nanosecond-formed structures (visible in Figure 3.14 (f)) cannot be observed in the transmission electron micrographs, they are visible to ion channeling, which averages over the projected surface. We observed good channeling for nanosecond-formed structures, which indicates that, even at the bases, the surface of the nanosecond-formed structures is more ordered than the surface of the femtosecond-formed structures. There is not a thick enough disordered surface layer to perform SAD on the nanosecond-formed microstructures.

### Chemical composition

To determine the concentration of sulfur, we perform Rutherford backscattering spectrometry (RBS) and ion channeling on the femtosecond and nanosecond-structured samples; we compare the measured RBS spectra to simulated [33] spectra from planar material. The RBS spectra of the femtosecond-structured samples indicate that the sulfur concentration in the uppermost 100 nm is about 0.7 at. % before annealing and about 0.5

at. % after annealing (see Section 3.7.2). The sulfur signal obtained with ion channeling is slightly lower than that obtained with randomly aligned RBS, suggesting that some of the sulfur impurities are substitutional. The femtosecond-structured samples, in contrast, channel poorly ( $\chi_{min}^{(Si)} \sim 50\%$ ) and the reduction in sulfur signal with channeling is comparable in magnitude to the possible sources of error. Hence we can only determine that between 20% and 70% of the sulfur in the unannealed femtosecond-structured sample is substitutional, and we cannot determine how much sulfur is substitutional in the annealed femtosecond-structured sample. In the nanosecond-structured samples, the sulfur concentration in the observable near-surface region is about 0.5 at. % before annealing, and about 0.4 at. % after annealing. The nanosecond-structured samples show much stronger silicon channeling ( $\chi_{min}^{(Si)} = 5.6\%$  before and  $6.6\%$  after annealing), and nearly half of the sulfur is substitutional ( $43\% \pm 7\%$  before and  $48\% \pm 8\%$  after annealing). The sulfur concentration is therefore very similar in the two types of structures, but much more of the affected material in the nanosecond-structured samples is single crystal than in the femtosecond-structured samples, and a great deal of the sulfur is definitely substitutional in the nanosecond-structured samples. These results are summarized as a part of Table 3.1 near the end of the chapter.

## 3.5 Effect of laser wavelength

The laser wavelength also affects the final morphology of the microstructures. In this section we use second harmonic generation [36] to examine how laser radiation with a central wavelength of 400 nm (*vs.* 800 nm) affects morphology.

### 3.5.1 Surface morphology

We used second harmonic generation to convert our 800-nm laser pulses into pulses with a central wavelength of 400 nm. Conversion efficiencies below 30% result in a lower

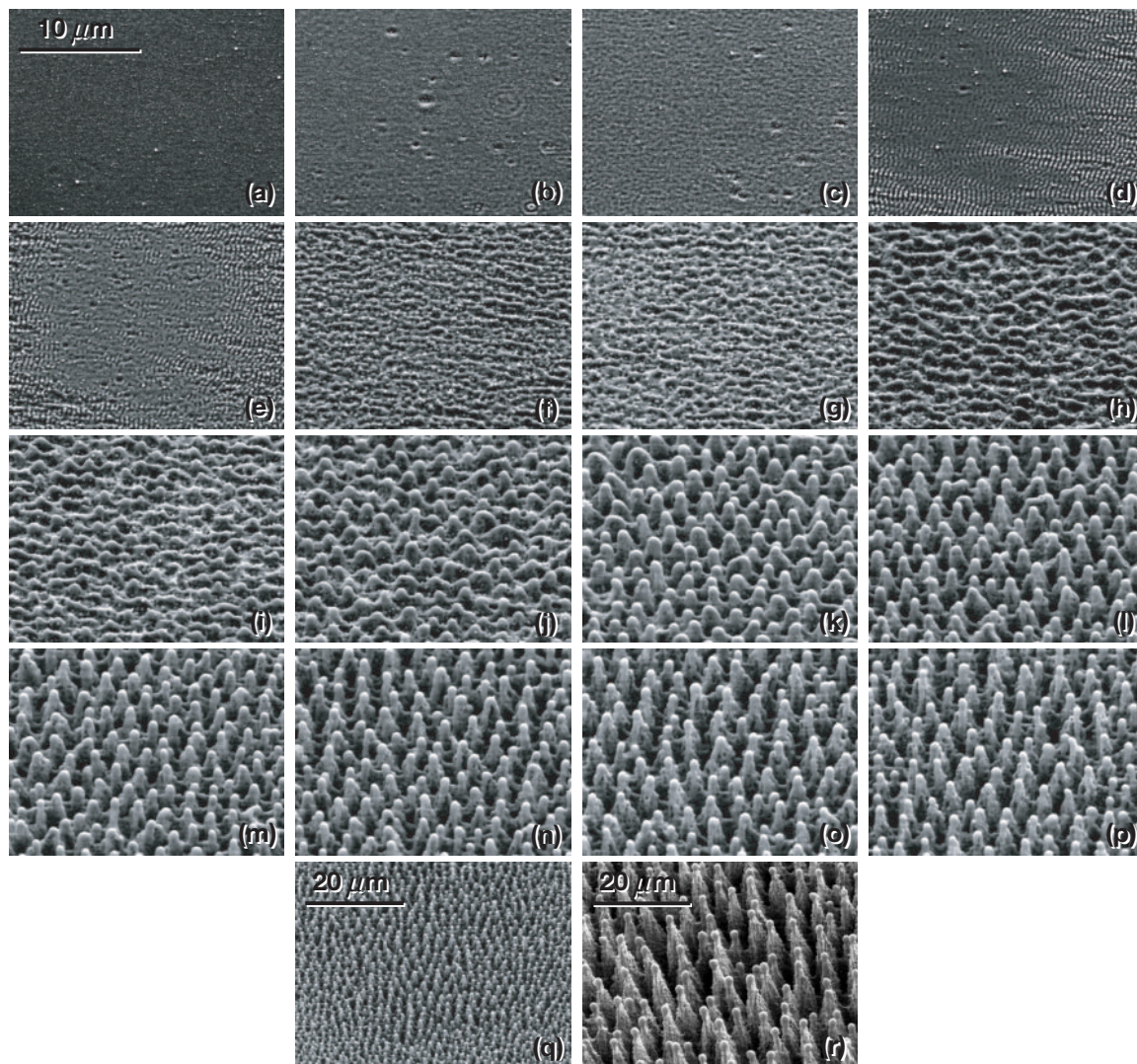


Figure 3.17: Scanning electron micrographs of a silicon surface after (a) 1, (b) 2, (c) 3, (d) 4, (e) 5, (f) 7, (g) 10, (h) 15, (i) 20, (j) 30, (k) 50, (l) 75, (m) 100, (n) 200, (o) 300, (p) 500 laser pulses with a center wavelength of 400 nm. Each SEM is taken at a 45° angle to the surface with the same magnification. Frames (q) and (r) show the final morphology for 400 nm and 800 nm radiation, respectively. The structures are smaller and more dense for 400 nm radiation.

pulse energy so, in order to maintain a fluence of  $8 \text{ kJ/m}^2$ , we use a smaller spot with a diameter of  $85 \text{ }\mu\text{m}$ . Figure 3.17 shows the evolution of the silicon surface irradiated with 400-nm pulses. The development follows the same progression as those made with 800 nm. We see small bubble-like defects after a few pulses and then the appearance of laser induced periodic surface structures after about 4 pulses. These ripples then bead up in a direction perpendicular to the long axis of the ripples. After approximately 10 pulses, a two dimensional pattern of beads is established and the microstructures are then dug out around the beads.

The ripples have a spacing close to the central wavelength of the laser pulses (400 nm), one half the wavelength of those shown in Section 3.1. The result is that the density of the final structures is higher than that with 800 nm (approximately two times higher). In addition, the structures after 500 pulses are smaller than those made with 800 nm laser light. The last two panels of Figure 3.17 show the final morphology for structures made with 400 nm (q) and 800 nm (r).

### 3.5.2 Surface layer structure and composition

At this time we do not have detailed information on the structure of the surface layer and the chemical composition for samples made with 400 nm light. Based on results in the pulse duration section (Section 3.4) and the dependence of melt depth on wavelength [37], we suspect that the disordered surface layer is thinner than the 800 nm irradiated samples.

## 3.6 Effect of polarization and propagation direction

Two additional laser characteristics that affect microstructure morphology are the polarization and laser propagation direction. In this section, we briefly describe how these

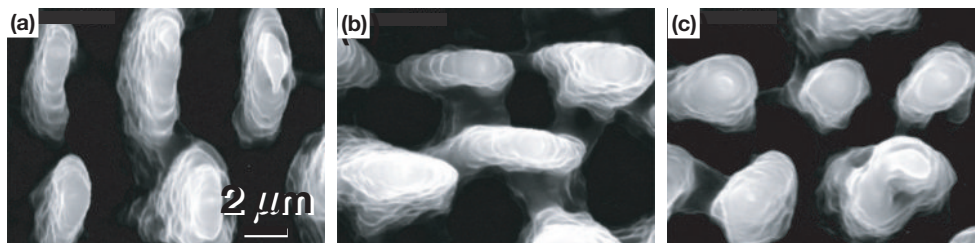


Figure 3.18: Morphology following irradiation with (a) horizontally-polarized, (b) vertically-polarized, and (c) circularly-polarized laser pulses.

two qualities affect the shape and growth direction of the microstructures.

### 3.6.1 Surface morphology

In Figure 3.6, we see that the base of each microstructure is elliptical, with a long and a short axis; the long axis is perpendicular to the polarization of the laser light. This shape is a result of the higher absorption of p-polarized light over s-polarized light [11, 2]. With the initial bead pattern established, laser light hitting the side of a bead along the horizontal direction (for the scanning electron micrographs in Section 3.1.1 this is the left and right side of the beads) is p-polarized light and light hitting the sides of a bead in the vertical direction (top and bottom) strikes as s-polarized light. Therefore higher absorption, and subsequently more ablation, occurs along the sides in the horizontal direction, where the incident light is p-polarized. Figure 3.18 shows the structure of the microstructures from above for three laser polarizations. Figure 3.18 (a) is our initial case of polarization in the horizontal direction, (b) is for light polarized in the vertical direction, and (c) is for circularly polarized light. When the polarization is rotated  $90^\circ$ , the long axis of the microstructure is also rotated  $90^\circ$ . For circularly polarized light there is no preferential ablation and the base of the microstructures is circular instead of elliptical.

The majority of the data presented in this dissertation is for laser irradiation

at normal incidence to the substrate. However, the direction of microstructure growth is always parallel to the direction of incident light, and is independent of the substrate's crystallographic planes [2]. That is, if we irradiate with laser pulses at  $45^\circ$  to the surface, the resulting microstructures point along the direction of the laser,  $45^\circ$  off-normal to the original substrate surface.

### 3.6.2 Surface layer structure and composition

We do not expect the polarization or the propagation direction to affect the structure or chemical composition of the surface layer.

## 3.7 Effect of ambient gas

In addition to laser parameters, we vary the gaseous atmosphere in which the sample is microstructured. In this section we examine the morphology for several different gas species at a pressure of 0.67 bar.

### 3.7.1 Surface morphology

As shown in Figure 3.19, the morphology of the silicon microstructures depends heavily on the gas in which they are formed. Figure 3.19 shows, specifically, the results of laser irradiation in two halogen containing gases, sulfur hexafluoride ( $\text{SF}_6$ ) and chlorine ( $\text{Cl}_2$ ), as well as nitrogen ( $\text{N}_2$ ), air, and vacuum. It should be noted that we used a pressure of 0.67 bar for each gas (except for vacuum, of course), but the laser fluence and shot number were adjusted to yield microstructures with heights of approximately 10–15  $\mu\text{m}$  for each gas. Using  $\text{SF}_6$  or  $\text{Cl}_2$  leads to sharp-tipped conical structures with a radius of curvature of approximately 500 nm. Structures made in air,  $\text{N}_2$ , and vacuum are much

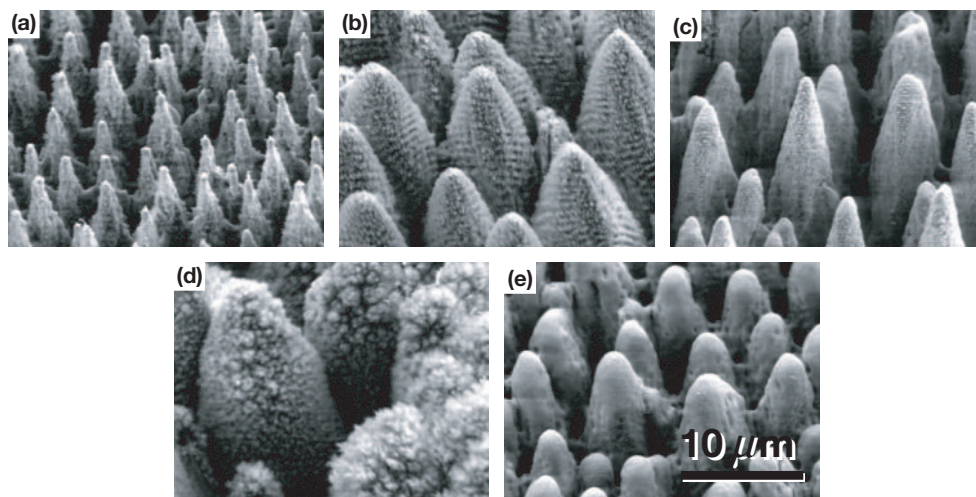


Figure 3.19: Scanning electron micrographs comparing surface morphology for different ambient gas species: (a) sulfur hexafluoride ( $\text{SF}_6$ ), (b) Nitrogen ( $\text{N}_2$ ), (c) Chlorine ( $\text{Cl}_2$ ), (d) air, and (e) vacuum. Each SEM is taken at a  $45^\circ$  angle to the surface with the same magnification.

more rounded than those made in the halogen-containing gases; the radius of curvature of their tips is approximately  $2\text{--}3\ \mu\text{m}$ .

We examined the effect of ambient gas on the number density of conical structures, as well as partial pressures of  $\text{SF}_6$  with  $\text{N}_2$  and  $\text{Cl}_2$  with  $\text{N}_2$  [20]. For a pure ambient gas, higher densities are achieved using  $\text{SF}_6$  or  $\text{Cl}_2$ . Surfaces prepared with  $\text{SF}_6$  give the greatest number density, followed by  $\text{Cl}_2$ . The number densities produced with  $\text{N}_2$  and air are approximately equal and are roughly a factor of two less than that of the  $\text{SF}_6$ -prepared surfaces. The number density of vacuum prepared samples lie roughly halfway between these two cases. In addition, we measured the number density of structures for surfaces patterned in either a  $\text{SF}_6$  ( $\text{Cl}_2$ ) alone, or in a mixture of  $\text{SF}_6$  ( $\text{Cl}_2$ ) and  $\text{N}_2$ . We made stationary samples of microstructures in background pressures of  $0\text{--}0.67$  bar of  $\text{SF}_6$  ( $\text{Cl}_2$ ). We then made similar stationary samples while varying the partial pressure of the  $\text{SF}_6$  ( $\text{Cl}_2$ ), but keeping the total pressure constant at  $0.67$  atm by adding  $\text{N}_2$ . In both cases,

the number density of microstructures increases with the partial pressure of SF<sub>6</sub> (Cl<sub>2</sub>). A plateau is reached for both SF<sub>6</sub> and Cl<sub>2</sub>; the maximum number density is reached at roughly 0.13 bar for Cl<sub>2</sub> and 0.54 bar for SF<sub>6</sub>.

Some important observations made from varying the ambient gas are that the ambient gas affects the sharpness, density, and ordering of the structures. It is also clear that the nanoscale features on the surface are different for each gas; we will address this shortly. The halogen-containing gases give sharper structures and it seems that reactivity and chemically reactive species in these gases is an important factor. However, recent results using other sulfur containing gases (H<sub>2</sub>S) show similar morphologies to the SF<sub>6</sub> samples despite the lack of a highly reactive species.

As we did for the shot number series in SF<sub>6</sub> in Section 3.1, we analyzed the evolution of samples made in vacuum (with no possible contribution from chemical interaction for the ambient environment) to understand in more detail the ambient gas contribution to the final morphology.

### **Early stage: vacuum**

As with SF<sub>6</sub>, following the second pulse a distinct, regular ripple pattern appears on the surface. These ripples are laser induced periodic surface structures at the wavelength of the laser light, perpendicular to its polarization. The area covered by ripples is larger for samples made in vacuum than in SF<sub>6</sub>, indicating that either the pressure or the surface/gas interaction suppresses the size of the melted/rippled area. Fourier analysis of the horizontal direction shows a strong peak at a frequency corresponding to the ripple period. There is no visible pattern in the vertical direction and, likewise, there is no peak in the Fourier power spectrum.

For vacuum samples, it takes many more pulses for the ripples to give way to

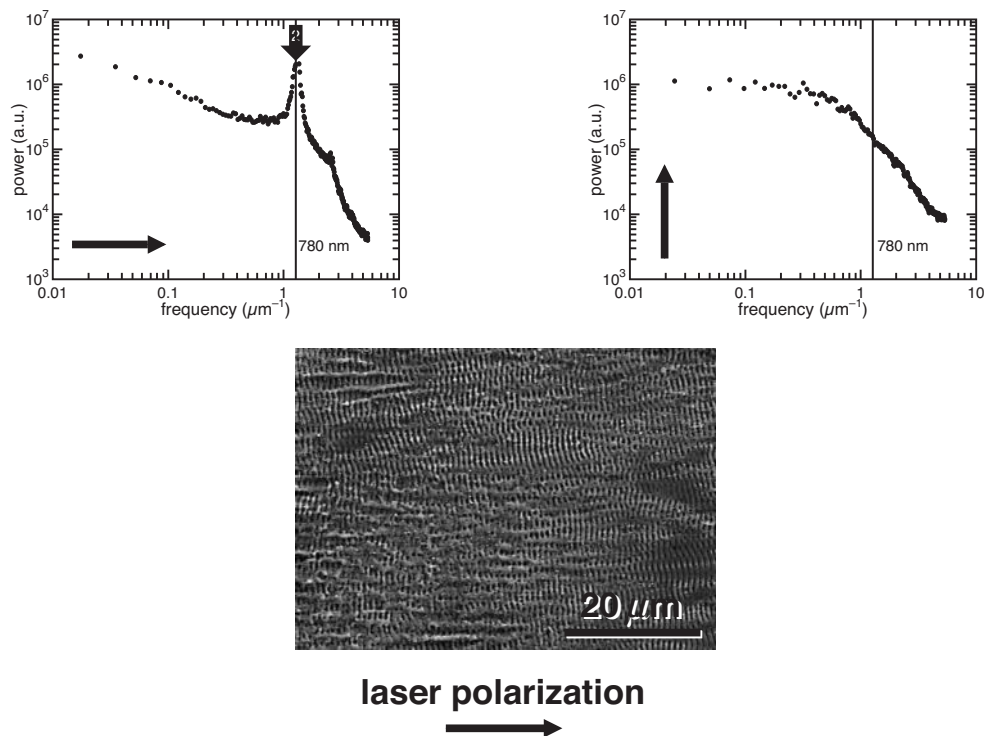


Figure 3.20: Fourier analysis of line-outs taken in the vertical and horizontal direction of a silicon surface after 2 laser pulses in vacuum. The scanning electron micrograph is taken normal to the surface.

beading. In addition, the beads formed during coarsening are much larger in vacuum than in  $\text{SF}_6$  (about  $2 \mu\text{m}$  vs.  $500 \text{ nm}$  in diameter). It takes about 50 pulses for the strong peak in the horizontal Fourier power spectrum to decrease. At this point, the beads have a strong periodicity in the direction perpendicular to the laser polarization. Figure 3.21 shows the Fourier transforms after fifty incident pulses in vacuum.

From 50 pulses to several hundred, the peak in the vertical direction broadens and shifts toward longer wavelengths. In addition, a peak in the Fourier power spectrum appears in the horizontal direction. Figure 3.22 shows the Fourier analysis of the surface after two hundred incident pulses. The characteristic spacings for the vacuum structures is constant for higher number of pulses; this marks the end of the early stage of formation.

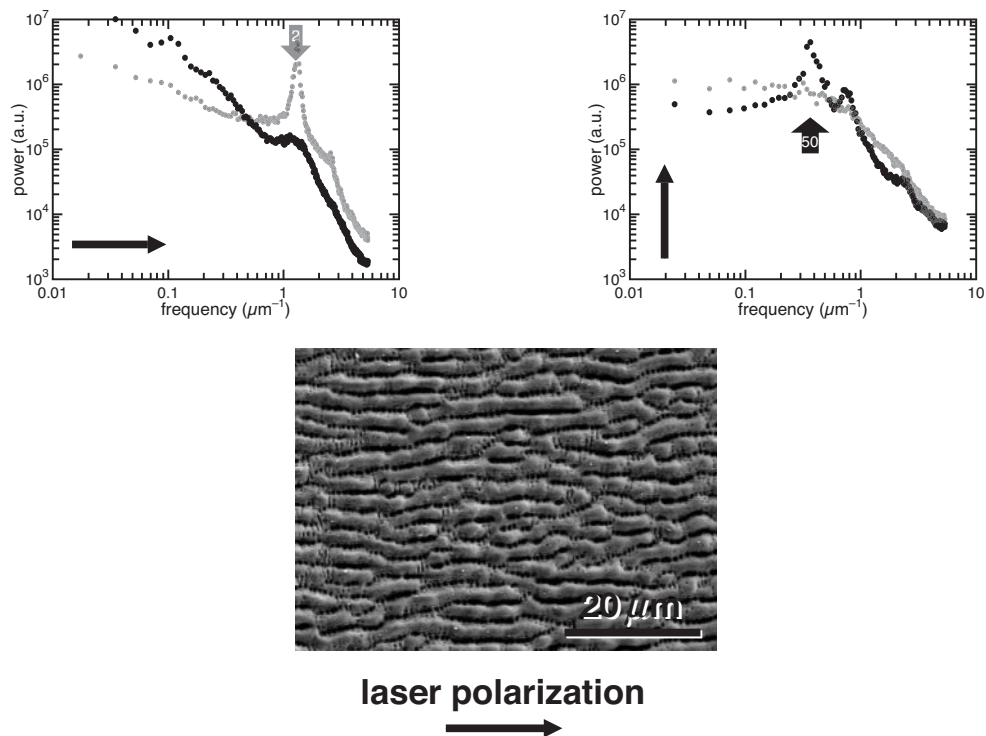


Figure 3.21: Fourier analysis of line-outs taken in the vertical and horizontal direction of a silicon surface after 50 laser pulses in vacuum. The scanning electron micrograph is taken normal to the surface.

Note that it takes 10 to 20 times more pulses for this to occur than in the  $\text{SF}_6$  samples. The beads, which become the peaks of the final structures, are much larger and blunter than those in the  $\text{SF}_6$  samples.

Although the morphologies are very different and the progression is much slower in vacuum, the stages of formation are similar for vacuum and  $\text{SF}_6$  samples. First, a ripple pattern at the wavelength of the laser forms after the second pulse, with the ripples long axis perpendicular to the laser polarization. By the fiftieth pulse, the ripple pattern has coarsened significantly and beads form along the ripples at a spacing larger than the wavelength of the laser. After a few hundred pulses, the beads become more pronounced and a characteristic spacing for both the vertical and horizontal directions emerges. Note

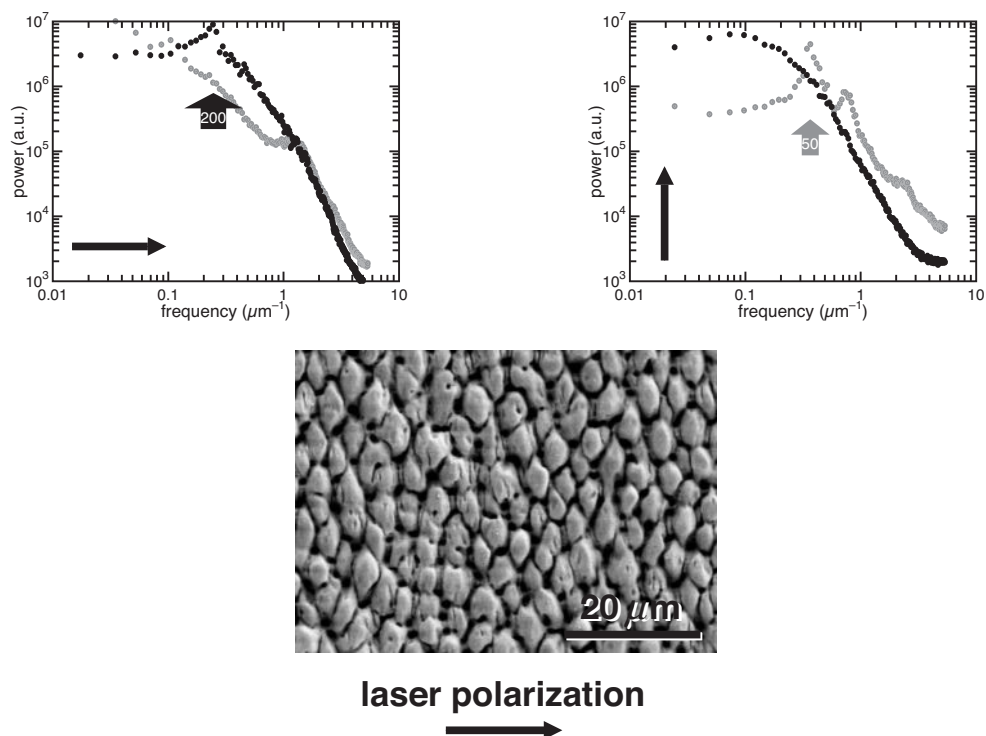


Figure 3.22: Fourier analysis of line-outs taken in the vertical and horizontal direction of a silicon surface after 200 laser pulses in vacuum. The scanning electron micrograph is taken normal to the surface.

that the spatial frequencies in vacuum samples are similar to those with made in  $\text{SF}_6$  despite the differing morphologies.

### Late stage: vacuum

At the end of the early formation stage, a two dimensional pattern of beads is established. This two dimensional pattern of beads remains in essentially the same arrangement throughout the entire late stage formation. From two hundred pulses to the end of formation, the final conical microstructures are etched out of the surface, with the beads formed at the end of the early stage ending up as the peaks of the cones. As with microstructures formed in  $\text{SF}_6$ , incident laser pulses preferentially remove material to the

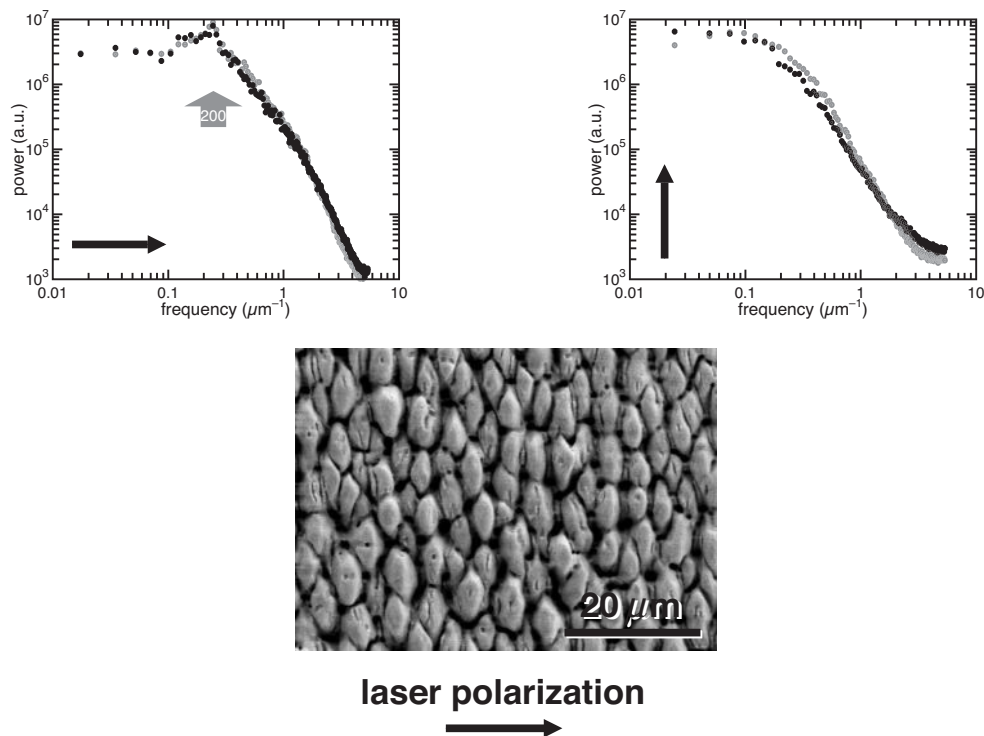


Figure 3.23: Fourier analysis of line-outs taken in the vertical and horizontal direction of a silicon surface after 500 laser pulses in vacuum. The scanning electron micrograph is taken normal to the surface.

sides of the beads, digging out the conical structures with each pulse. Again, the beads from the end of the early stage act as protective caps and focus laser energy into the spaces between them. A final Fourier analysis is shown in Figure 3.23 for a scanning electron micrograph after 500 incident pulses. In summary, the vacuum samples went through the same stages of development as  $\text{SF}_6$  samples, but the number of pulses required to reach each stage was higher for vacuum. The final structures are blunter and larger than those formed in  $\text{SF}_6$ , are less dense, and appear less ordered.

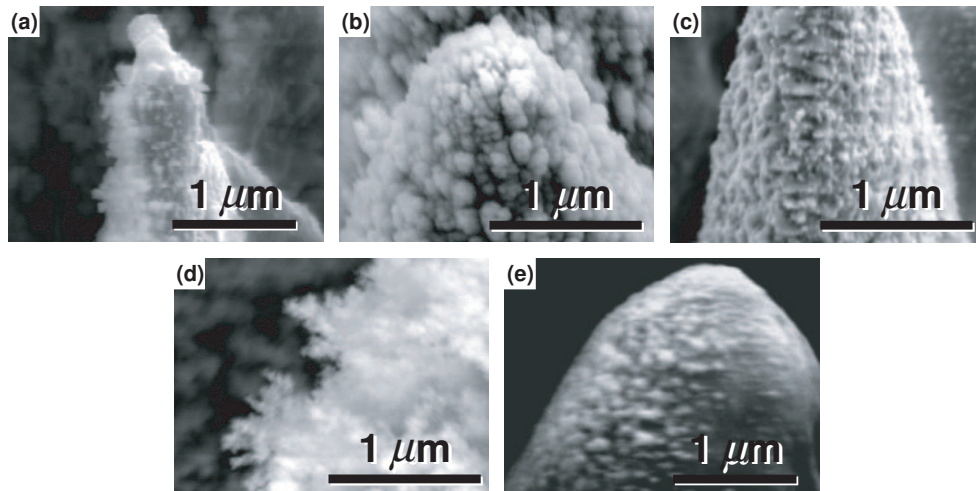


Figure 3.24: Scanning electron micrographs of nanoscale morphology for different ambient gas species: (a) sulfur hexafluoride ( $\text{SF}_6$ ), (b) nitrogen ( $\text{N}_2$ ), (c) chlorine ( $\text{Cl}_2$ ), (d) air, and (e) vacuum.

### 3.7.2 Surface layer structure and composition

The micrometer-scale morphology varies a great deal depending on the ambient gas, as does the nanoscale structure and chemical composition.

#### Surface layer structure

At this point, we have been unable to analyze transmission electron micrograph samples of the various gas species. However, high magnification scanning electron micrographs of each surface reveal large differences in the nanoscale structure on the surface (Figure 3.24)<sup>4</sup>. Samples made in  $\text{SF}_6$  have the sharpest tips as well as some dendritic nanoscale material on the surface. As mentioned in section 3.2, this material is not present for stationary samples. The nanoscale material is very similar in appearance to material collected from the ejected plume during irradiation in  $\text{SF}_6$  [20]. Samples made in  $\text{N}_2$  have complex nanoscale features; there are rough, 50-nm clusters of material covering the entire

<sup>4</sup>Each gas sample shown was made while being translated.

surface and a visible ripple variation with a period near 800 nm along the sides of the microstructures. Samples made in  $\text{Cl}_2$  have a relatively smooth surface with a comparatively small amount of nanoscale material on the surface. There is 5–10 nm scale roughness along the side of each microstructure. Samples made in air are covered in clusters of dendritic material over the microstructures. At high magnification these fractal-like growths look similar to ice crystals or clumps of snow flakes. Lastly, the nanoscale features on the vacuum samples are similar to the  $\text{Cl}_2$  samples. There is little nanoscale material on the surface but 10–15 nm roughness along the sides of the microstructures.

### Chemical composition

To characterize the chemical species present in each surface, we used secondary ion mass spectrometry (SIMS). Briefly, in SIMS, an energetic beam of ions is used to sputter secondary ions from a surface; the chemical composition of the sputtered material is then analyzed with mass spectrometry. To determine the chemical composition of each microstructured surface, the ratio of the mass spectrometry signal from a given chemical species is normalized relative to silicon using literature values for the relative sensitivity factor of each chemical species in a silicon matrix. The relative sensitivity factors are calculated with data taken from flat silicon surfaces, so the compositions reported are approximate due to the topology of the microstructured silicon.

For each gas, the chemical species present in the ambient gas becomes incorporated into the surface in large amounts; different elements are incorporated at different levels. Figure 3.25 shows the fractional concentration of chemical species in the microstructured silicon surfaces. The smaller amount of fluorine incorporated in the  $\text{SF}_6$  samples is attributed to its high reactivity with silicon and likely removal of silicon-fluorine complexes during the microstructure formation process. All of the samples contain oxygen from the

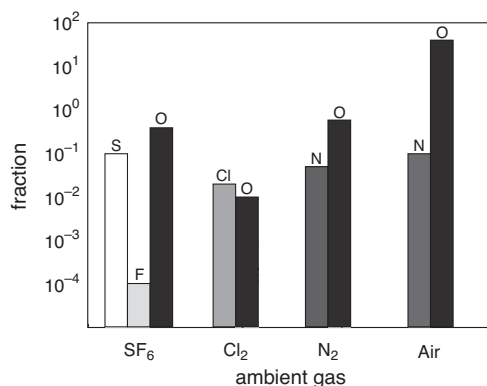


Figure 3.25: Fractional concentration of chemical species as measured by secondary ion mass spectrometry for different ambient gas species: (a) sulfur hexafluoride (SF<sub>6</sub>), (b) nitrogen (N<sub>2</sub>), (c) chlorine (Cl<sub>2</sub>), and (d) air.

native oxide layer that grows on the surface after texturing, but the air sample contains two orders of magnitude more oxygen than the other samples. The high oxygen content and further analysis using Rutherford backscattering spectrometry and transmission electron microscopy suggest that a silicon rich layer of silica, SiO<sub>x</sub> ( $x < 2$ ) [38], is formed. The amount of oxygen in the SF<sub>6</sub>, Cl<sub>2</sub>, and N<sub>2</sub> samples is correlated with surface area (roughness). Samples analyzed with SIMS were not treated with an HF dip and, therefore, the oxygen signal for the SF<sub>6</sub>, N<sub>2</sub> and Cl<sub>2</sub> samples is likely due to a native oxide layer. Following an HF dip to remove the native oxide layer and surface contaminants, samples made in vacuum do not show the presence of any elements other than silicon.

### 3.8 Effect of ambient gas pressure

In this section we examine morphology differences brought about by varying the pressure of SF<sub>6</sub>.

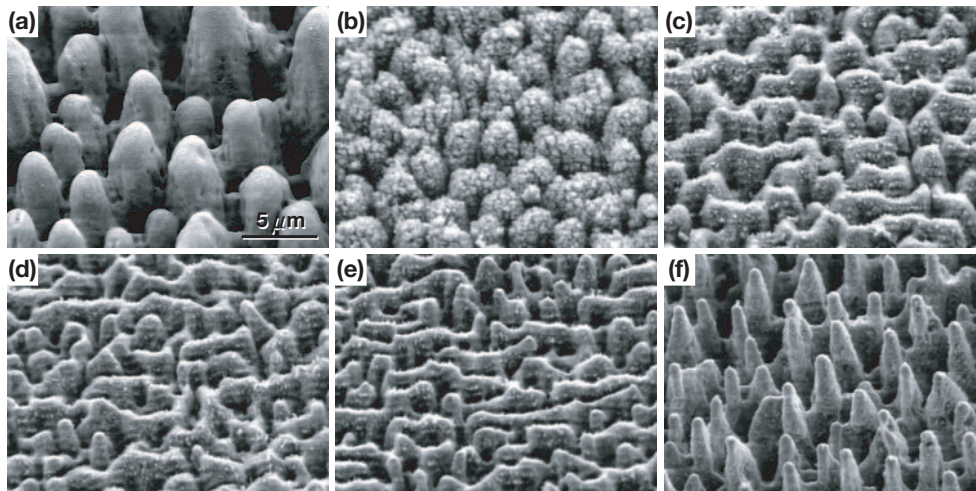


Figure 3.26: Scanning electron micrographs of the surface morphology for different pressures of  $\text{SF}_6$ : (a) vacuum ( $10^{-6}$  torr), (b) 0.007 bar, (c) 0.027 bar, (d) 0.13 bar, (e) 0.40 bar, and (f) 0.67 bar. Each SEM is taken at a  $45^\circ$  angle to the surface with the same magnification.

### 3.8.1 Surface morphology

Figure 3.26 shows the morphology for microstructures with increasing pressures of  $\text{SF}_6$ . At a very low pressure of  $\text{SF}_6$  (0.007 bar), the surface has a great deal of nanostructure. It looks similar to vacuum samples covered in clumps of nanoparticles. For pressures between 0.027 and 0.40 bar, ridges form and the beginnings of smaller, sharper structures occur. Above 0.533 bar the surface begins to resemble the conical microstructures we see at our standard conditions. Increasing the pressure from 0.67 bar to 1 bar does not affect the final morphology.

### 3.8.2 Surface layer structure and composition

At this time we do not have data on the effect of gas pressure on the surface layer structure or composition.

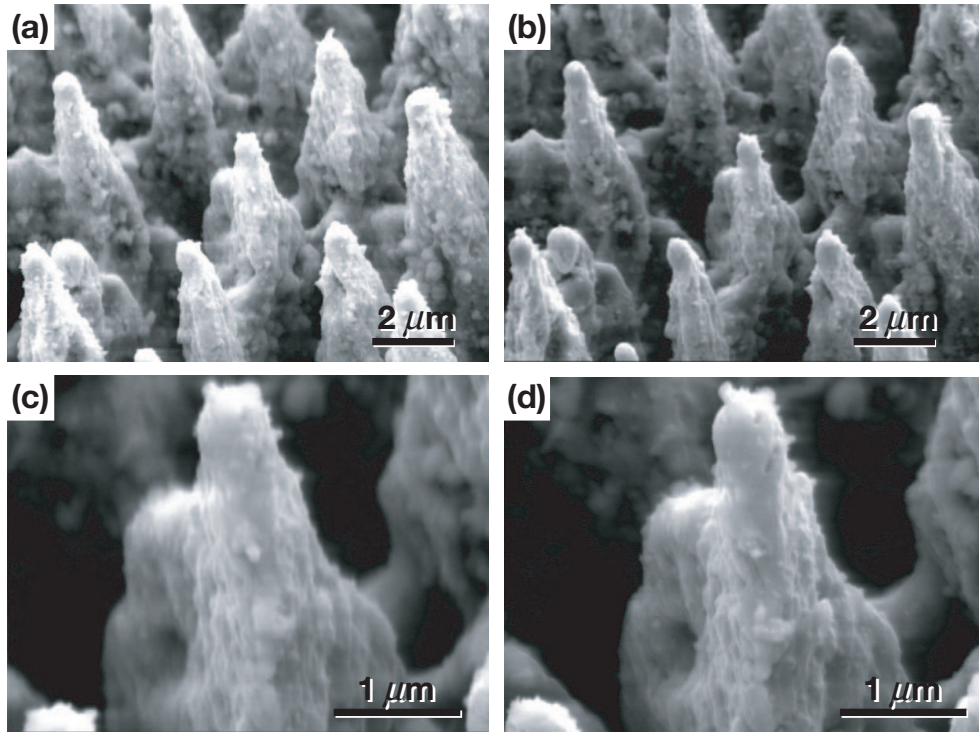


Figure 3.27: Scanning electron micrographs of microstructured silicon ((a) and (c)) before annealing and ((b) and (d)) after annealing at 1075 K for 3 hours.

### 3.9 Effect of annealing

As a part of our post-processing analysis, we often anneal samples following laser microstructuring. Annealing will be an important step later in this dissertation and here we analyze any morphological or chemical changes brought about by annealing.

#### 3.9.1 Surface morphology

As shown in Figure 3.27, annealing has no visible effect (within the resolution of the SEM) on microstructure morphology or the surface-nanoparticle morphology. The same area of a microstructured surface is shown before and after annealing for 3 hours at 1075 K.

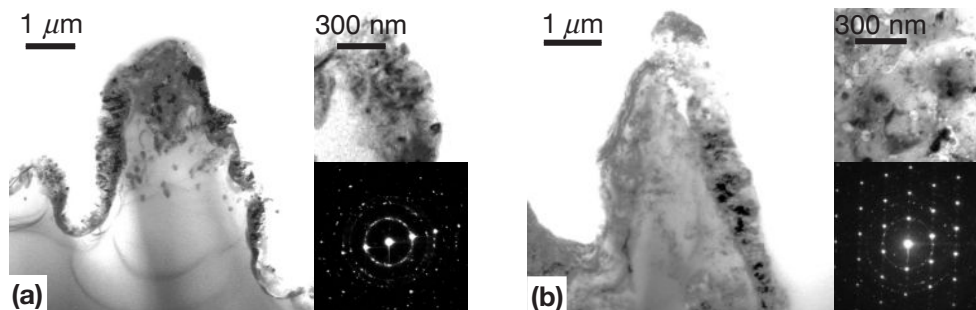


Figure 3.28: Transmission electron micrographs of the surface before (a) and after (b) annealing. The annealed sample has sharper features in the diffraction pattern. Insets: (upper) high-magnification view of the disordered region at the tip of the microstructure and (lower) selected area electron diffraction pattern obtained from the disordered region.

### 3.9.2 Surface layer structure and composition

Although we do not see any change in the microstructure morphology, there are some effects in both the nanoscale structure and chemical makeup of the surface layer.

#### Surface layer structure

Figure 3.28 shows transmission electron micrographs of an annealed and a non-annealed sample. The surface layer is similar in thickness and structural composition before and after annealing. However, the diffraction rings are sharper for the annealed sample. The sharper rings most likely indicate that annealing increases the crystallinity of the sample somewhat. Other factors, such as the crystalline plane in focus, could sharpen the diffraction pattern as well.

#### Chemical composition

We use Rutherford backscattering spectrometry and simulation to characterize the chemical content of the surface before and after annealing. After an anneal of 30 minutes at 725 K, the amount of sulfur in the surface layer drops from about 0.7 at % to

0.5 at %. Annealing at 875 K for 30 minutes also results in a concentration of 0.5 at % sulfur. The decrease in the observed sulfur concentration upon annealing most likely reflects sulfur diffusing deeper into the sample than can be observed by Rutherford backscattering spectrometry (RBS)<sup>5</sup>. These results are summarized as a part of Table 3.1 near the end of the chapter.

### 3.10 Effect of silicon substrate properties

In our work thus far, we have found little, if any, effect on micrometer-scale morphology and chemical composition from the following substrate properties: crystalline orientation, dominant carrier (*n*- or *p*-doping), doping level, and presence or absence of a native oxide layer before irradiation.

### 3.11 Summary of chemical composition (RBS data) and trends

Before moving onto the discussion section, we summarize some of the important information presented in this chapter. Table 3.1 summarizes all of the chemical composition data we have from Rutherford backscattering measurements; the important parameter varied in each section is in bold<sup>6</sup>. Table 3.2 summarizes trends that we see in morphology and composition with experimental parameters. The trends are listed for increasing values of the experimental parameter.

---

<sup>5</sup>The diffusion length of S in *c*-Si in 30 minutes at 775K was estimated to be 25 nm by extrapolation from data in [39], p. 68. In microcrystalline or amorphous silicon, the diffusion length may be somewhat different but is unlikely to increase more than threefold.

<sup>6</sup>The RBS spectra may be affected slightly by the changing morphology of the surface, as the surface area of the samples changes as processing conditions change. However, we are confident in comparing the sulfur concentrations for the microstructures made with 2, 3, and 5 laser pulses and the microstructures made with 3, 4, and 5 kJ/m<sup>2</sup> because they are similar in size and shape. As the shape of the microstructures is unchanged by annealing, the concentrations before and after annealing can also be compared with confidence.

Average laser fluence (kJ/m <sup>2</sup> )	Number of pulses	Annealing temperature (30 minutes)	Pulse duration	Sulfur concentration ( $\pm 0.1$ at. %)
<b>2.5</b>	500	-	100 fs	0.3
<b>3.0</b>	500	-	100 fs	0.3
<b>4.0</b>	500	-	100 fs	0.4
<b>4.9</b>	500	-	100 fs	0.6
<b>8.0</b>	500	-	100 fs	0.7
<b>10.0</b>	500	-	100 fs	0.7
8.0	<b>2</b>	-	100 fs	0.2
8.0	<b>3</b>	-	100 fs	0.4
8.0	<b>5</b>	-	100 fs	0.4
8.0	<b>10</b>	-	100 fs	0.5
8.0	<b>20</b>	-	100 fs	0.6
8.0	<b>50</b>	-	100 fs	0.6
8.0	<b>500</b>	-	100 fs	0.7
8.0	500	<b>725 K</b>	100 fs	0.5
8.0	500	<b>875 K</b>	100 fs	0.5
30.0	1500	-	<b>30 ns</b>	0.5
30.0	1500	875 K	<b>30 ns</b>	0.4

Table 3.1: Summary of sulfur concentration in samples determined by Rutherford backscattering spectrometry. The bolded values highlight the important parameter being varied from standard conditions.

Observables					
Parameter	Morphology			Composition	
	Height	Density	Tip Size	Sulfur	Crystallinity
Shot number	↑	↓	↓	↑	–
Fluence	↑	↓	↓	↑	–
Wavelength	↑	↓	↓	–	–
Gas pressure	↑	↑	↓	↑	–
Anneal temp.	–	–	–	–	↑

Table 3.2: Summary of the trends in observable morphology and composition characteristics with experimental parameters. The ↑ symbol indicates that the observable increases as the experimental parameter is increased; the ↓ symbol indicates a decrease in the observable.

### 3.12 Discussion

Although a rigorous model for the formation mechanism is not yet determined, we can use the observations made in this chapter to speculate on the mechanisms responsible in creating these quasi-ordered array of microstructures. We hope that this chapter instills in the reader a sense of the large parameter space involved in our experimental procedure. The experimental complexity and intense conditions created in the focal region of the laser make direct observation and modeling rather difficult. However, using the information in this chapter and existing research on similar microstructures formed on a variety of materials (including silicon), we speculate on the important factors for microstructure formation.

Periodic surface ripples, conical microstructures, whisker-like structures, and pyramidal microstructures have all been observed following high-energy ion-bombardment during sputtering experiments [40, 41, 42, 43, 44, 45, 46, 47]. In work that is closely related to our research, conical structures formed after irradiation with nanosecond laser pulses

have been observed by several research groups [7, 8, 10, 12, 13, 14, 15, 17, 48, 49, 50]. Although the two means of irradiation (ion-bombardment and laser) are very different, the morphology of the resulting structures is similar. In these papers, there are several proposed formation mechanisms for the microstructures, but there is no complete explanation and most of the papers only address one aspect of the formation mechanism. However, despite the lack of a rigorous explanation, there are four significant factors included in most of the proposed mechanisms: ablation/sputtering, melting, chemical etching/interaction, and redeposition. The degree to which these factors contribute to the final morphology of the surface depends heavily on experimental conditions.

We begin with a chronological description of what occurs during irradiation with each laser pulse. As a laser pulse strikes the surface (at fluences above the ablation threshold), material is ablated from the surface; a thin layer of material that is not ablated, but melts, either by ultrafast melting or thermal melting, is left behind. This melted layer evolves and interacts with its surroundings until it resolidifies. While the surface is melted, chemical species from the ambient gas interacts with the melt layer either through etching or implantation into the surface [51]. Some of the ambient gas molecules inside the focal region of the laser dissociate in the intense electric field [52], so numerous derivatives of the ambient gas could be present at the surface. The possible chemical reactions for our standard conditions are covered in both [18] and [20]. The main chemical interactions between dissociated  $\text{SF}_6$  and the melted surface layer are etching of the silicon surface by fluorine and incorporation of sulfur into the silicon surface. Lastly, ablation results in a rich cloud of the the substrate material above the molten surface and redeposition of removed material occurs. After about a microsecond, the surface resolidifies and energy deposited by the laser diffuses out of the focal region. At this point the surface is permanently altered and, when another laser pulse strikes the surface, the process occurs again with different initial

conditions.

Before suggesting a formation mechanism, we comment on the significance of observations made earlier in this chapter. The first observation we highlight comes from the effect of fluence (Section 3.3) on our final microstructures. Conical microstructures do not form unless the fluence is above the ablation threshold for silicon. This indicates that ablation is a critical component to the formation mechanism. Pedraza *et al.* observe growth of conical structures while working with nanosecond pulses *below* the ablation threshold. In our attempt to mimic their work, we also used fluences below the ablation threshold and see conical structures form. However, the fluence is an average fluence for a spot hitting a *flat* surface. The surface is only flat for the first few pulses, and, after several hundred pulses, it is far from flat. After a few hundred pulses of nanosecond duration, the surface has protrusions much like the femtosecond case after 10 pulses. These protrusions concentrate light into the pits beside them and, inside these pits, the fluence rises *above* the ablation threshold. In fact, while structuring with nanosecond laser pulses, we do not observe the presence of a plasma spark (a strong indication of ablation) until several hundred laser pulses have struck the surface. Also, Fowlkes *et al.* observe that, at high pulse count, the nanosecond-laser-formed structures begin to decrease in height and eventually end up below the surface; indicating that ablation becomes a more dominant effect once the microstructures are formed [13].

From this information, we conclude that ablation is a necessary condition for microstructure formation. But it is important to keep in mind that, in general, the energy density quoted is an average value for a *flat* surface and that a roughened surface topology can result in higher energy concentrations in places. We feel that energy concentration on a roughened surface is the reason for the similarity in morphology evolution for increasing shot number and fluence. As the structures evolve with shot number, they become sharper

and effectively increase the fluence deposited in the pits to the side of the structures. The same morphology is seen with lower fluence and higher shot number as with higher fluence and lower shot number.

Another important observation to be made is that redeposition is definitely occurring during the formation process. The strongest evidence for this is that nanosecond-laser-formed structures are tens of microns above the substrate surface (Section 3.4). From a fluid dynamics discussion, Pedraza *et al.* conclude that capillary motion of molten material cannot yield the microstructure shape we see. They conclude that the dominant mechanism is redeposition of gaseous material (removed from the pits around the structures) at the molten tips. This process is akin to whisker growth by the vapor-liquid-solid (VLS) mechanism [53]. Also, the presence of the spherical tips on both the femtosecond and nanosecond-laser-formed structures is indicative of a VLS process and evidence that redeposition is occurring. It appears that the most dominant change brought about by increasing pulse duration from femtoseconds to nanoseconds is that redeposition becomes dominant over ablation and etching.

For all experiments, the chemical species in the ambient gas are implanted into the surface layer during irradiation (Section 3.7). In the ns-formed structures, sulfur incorporation process is probably similar to gas immersion laser doping (GILD) [54], in which a semiconductor is doped by melting the surface with nanosecond-laser pulses in the presence of a gas that contains the desired dopants. The dopants are incorporated into the melt and the rapid solidification that follows laser melting produces highly supersaturated solid solutions [55]. Sulfur may be incorporated into the femtosecond-formed structures by a similar process.

Also, the final morphology depends a great deal on the ambient gas and the interaction of the chemical environment with the molten surface. For many years, we felt

that the reactivity of the elements in the ambient gas was the important factor. However, recent evidence that a non-halogen containing gas ( $\text{H}_2\text{S}$ ) yields sharp conical microstructures indicates that perhaps it is the inclusion of elements into the molten surface and the subsequent effect on fluid dynamics that is more important. Incorporation of some elements yields sharp, ordered microstructures (S and Cl), while others yield blunt, disordered structures (O and N).

Lastly, the presence of a molten layer following laser irradiation is necessary for formation of conical microstructures. The femtosecond-laser fluences used are not far above the ablation threshold, and so we expect a molten layer to form at the surface after the laser-induced plasma recombines and the electrons equilibrate with the lattice [51]. The presence of laser induced periodic surface structures after a few pulses leaves little doubt that the surface is molten following irradiation. The way in which this molten surface evolves and interacts with its environment determines the final micrometer-scale morphology, chemical composition, and nanoscale structure of the surface layer. From the evidence we have collected, we feel that it is a combination of fluid dynamics, material removal/redeposition, and implantation of chemical species that yield sharp, conical microstructures [56]. All of these processes require the presence of a molten surface layer.

Using the observations highlighted above, we present a formation process for femtosecond-laser-formed conical microstructures. Following the first laser pulse, the surface is pocked with randomly dispersed defects (Figure 3.1 (a)). These act as scattering centers for the next pulse, resulting in laser induced periodic surface structures through capillary wave excitation in the molten surface. The next few laser pulses strike the surface and melt the ripple pattern. The ripples can be thought of as one half of a silicon column on the surface. A liquid cylinder whose length is larger than its radius is unstable and tends collapse into a row of equally sized and equally spaced drops to reduce surface tension (a

phenomenon called cylindrical collapse described by Joseph Plateau in the 1800s) [57]. In our case, the laser melted ripples collapse, or bead-up, along the long axis of the ripple. The periodicity and size of these beads is affected by several parameters. First, the wavelength of the laser induced periodic surface structures is important in the spacing of the beads, which is clearly shown by comparing structures made with 400 nm light with those made with 800 nm light. Furthermore, capillary waves and surface tension influence the evolution of the final bead spacing and size. Surface tension and capillary waves are, in turn, influenced by melt depth, temperature, ambient gas pressure, and inclusion of impurity atoms in the melt layer. We feel that the inclusion of sulfur into the surface and its effects on surface tension are extremely important in creating small, regularly spaced beads. Once the bead pattern is formed, preferential removal of material to the sides of the beads (ablation) takes over as the dominant factor and the final conical microstructures are dug out of the surface. Redeposition continues to occur at the molten tip, but ablation dominates the changes in morphology. At the end of several hundred pulses, we have a quasi-ordered array of sharp conical microstructures.

This proposed formation mechanism is strictly for femtosecond-laser-formed microstructures in the presence of SF<sub>6</sub>. Consequently, the mechanism will vary somewhat for different conditions, but the major themes and observations should apply to other experimental conditions.

## Chapter 4

# Optical and electronic properties

In addition to microstructuring the surface, femtosecond-laser irradiation in the presence of SF<sub>6</sub> turns the normally grey, mirror-like surface of silicon into a deep, velvet black. The black surface is clear indication that laser microstructuring alters the optical properties of the silicon surface. In this chapter, we again vary numerous experimental parameters as we did in Chapter 3, but now we examine how experimental parameters affect the optical and electronic properties of microstructured silicon.

Again, our standard conditions are as follows: irradiation of an *n*-doped silicon wafer (*n*-Si(111), 260 μm thick, resistivity  $\rho = 8 - 12 \Omega\cdot\text{m}$ ) with an average of 500 laser pulses (100 fs, central wavelength 800 nm, fluence 8 kJ/m<sup>2</sup>) in 0.67 bar of SF<sub>6</sub>. We vary the number of incident laser pulses, the laser fluence, wavelength, pulse duration, ambient gas species and pressure, substrate doping and crystalline orientation, and annealing temperature. We then measure the effect on the optical and electronic properties of microstructured silicon.

## 4.1 Optical measurements

In order to measure optical properties, we use a Hitachi U-4001 spectrophotometer equipped with an integrating sphere. With the spectrophotometer, we measure the total hemispherical (specular and diffuse) reflectance ( $R$ ) and transmittance ( $T$ ) of a sample. The integrating sphere ensures that both specular and diffuse reflectance, as well as both direct and scattered transmittance, are measured accurately. Light from two lamp sources, one for the UV and one for the visible and near-IR, is sent into a monochromator that selects a single wavelength and directs it onto a sample; the amount of light, transmitted or reflected, is then measured relative to a baseline reading taken using a highly reflective titanium oxide blank. The operational wavelength range for this device is 250 nm to 2500 nm.

For reflectance measurements, samples are carefully taped on an optical quality, calcium fluoride window for support; the window is used because samples are smaller than the access ports of the integrating sphere. The calcium fluoride window is then placed on the back port of the integrating sphere in order to reflect light back into the integrating sphere detector. The reflectance of the calcium fluoride window is low ( $< 6\%$ ) in the operational wavelength range [20]. For transmittance, samples are suspended at the front port of the integrating sphere; all transmitted light (scattered or direct) enters the integrating sphere detector. The spectrophotometer setup is described in more detail by Younkin [20].

By measuring both the reflectance ( $R$ ) and transmittance ( $T$ ) from 250 nm to 2500 nm, we calculate the absorptance of each sample with

$$A(\lambda) = 1 - T(\lambda) - R(\lambda). \quad (4.1)$$

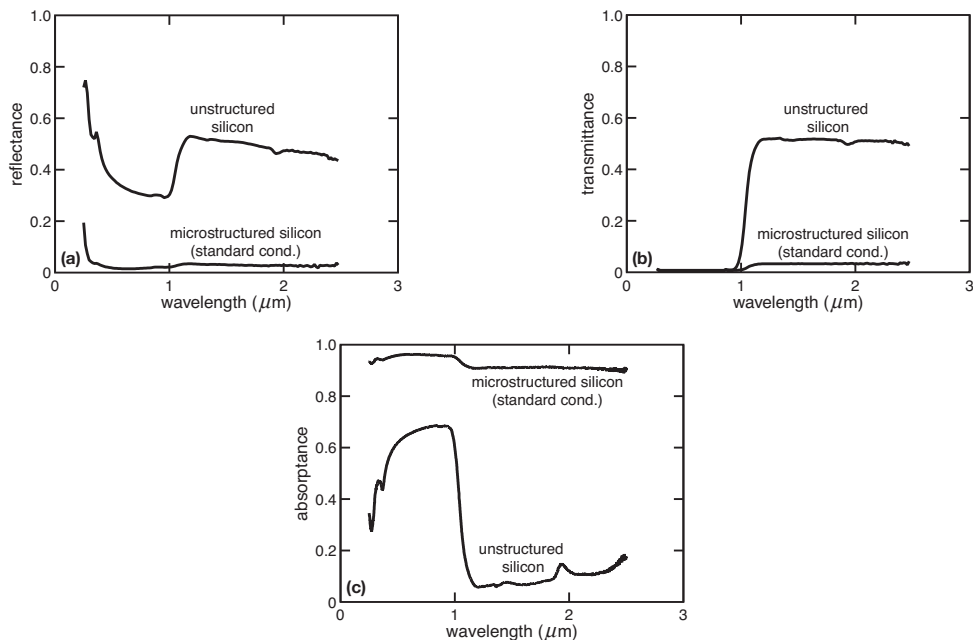


Figure 4.1: (a) Reflectance, (b) transmittance, and (c) the calculated absorptance of microstructured silicon for standard conditions. For reference, the same measurements are shown for unstructured, crystalline silicon.

#### 4.1.1 Optical properties of femtosecond-laser microstructured silicon

Figure 4.1 shows the measured reflectance, transmittance, and calculated absorptance for an unstructured silicon wafer and microstructured silicon. The drop in the absorptance for crystalline silicon near 1100 nm corresponds to the band-gap energy of crystalline silicon (1.07 eV). Light at longer wavelengths does not contain enough energy to promote an electron from the valence band to the conduction band and absorption becomes negligible for crystalline silicon.

Microstructured silicon has a drastically decreased reflectance and transmittance over the entire measured spectrum. The lowered transmittance and reflectance results in near-unity absorptance in the entire wavelength region  $250 \text{ nm} < \lambda < 2500 \text{ nm}$ . The increased absorption in the visible is consistent with the black appearance and, indeed, across

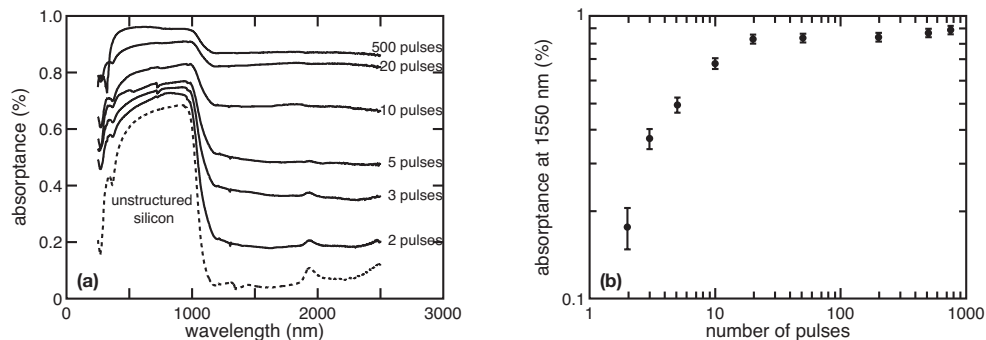


Figure 4.2: (a) Wavelength dependence of absorptance on the number of laser pulses used in microstructuring and (b) the dependence of absorptance at 1550 nm on the number of laser pulses used in microstructuring. All samples were made with  $8 \text{ kJ/m}^2$  and  $0.67 \text{ bar SF}_6$

this large range of wavelengths the surface is quite "black." By varying experimental parameters we examine what is responsible for the high, featureless absorption. In the following sections, we present only absorptance, which is calculated from a measured reflectance and transmittance (Equation 4.1). All optical measurement samples are made by translating the substrate in order to microstructure a  $10 \times 10 \text{ mm}^2$  area.

#### 4.1.2 Effect of shot number

In this section, we examine the effect of shot number on the optical properties of microstructured silicon. Figure 4.2 (a) shows that the absorptance increases over the entire wavelength range as the number of laser pulses increases. Figure 4.2 (b) shows that the absorptance at 1550 nm (a below-band gap wavelength) increases strongly with the number of pulses delivered to the sample, up to 20 pulses; additional pulses have little effect. For each microstructured sample, the absorptance is essentially constant and featureless between 1.2 and  $2.5 \mu\text{m}$ , increasing with the number of pulses. It should be noted that the increase in absorptance for below-band gap wavelengths saturates around 20 pulses, the same number of pulses at which the sulfur content saturates (see Table 3.1).

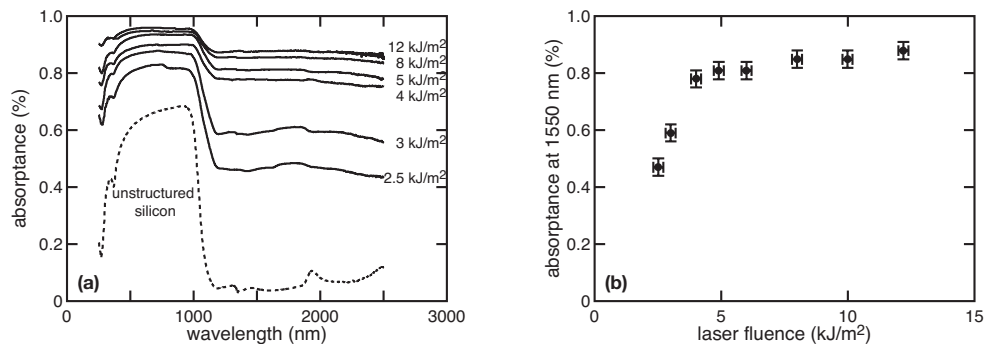


Figure 4.3: (a) Wavelength dependence of absorptance on the laser fluence used in microstructuring and (b) the dependence of the absorptance at 1550 nm on the laser fluence used in microstructuring. All samples were made with 500 laser pulses and 0.67 bar SF<sub>6</sub>.

### 4.1.3 Effect of fluence

In this section, we examine the effect of laser fluence on the optical properties of microstructured silicon. Figure 4.3 (a) shows that absorptance increases with fluence across the entire measured spectrum. Figure 4.3 (b) shows that the absorptance at 1550 nm increases strongly with fluence for fluences up to about 5 kJ/m<sup>2</sup> and increases more slowly for higher fluences. Surfaces made with a fluence of 4 kJ/m<sup>2</sup> or higher display constant absorptance *vs.* wavelength at below-band gap wavelengths; at lower fluences, the absorptance decreases gradually with increasing wavelength. With 500 laser pulses, fluences below 2.5 kJ/m<sup>2</sup> do not produce uniform microstructuring of the surface (see Figure 3.10). Fluences less than 2 kJ/m<sup>2</sup> neither alter the surface nor affect the optical properties. Again, it should be noted that the increase in absorptance at below-band gap wavelengths saturates at around 5 kJ/m<sup>2</sup>, the fluence at which the sulfur content saturates (see Table 3.1).

### 4.1.4 Effect of pulse duration

In this section, we examine the effect of changing the pulse duration from femtoseconds to nanoseconds on the optical properties of microstructured silicon. The femtosecond-

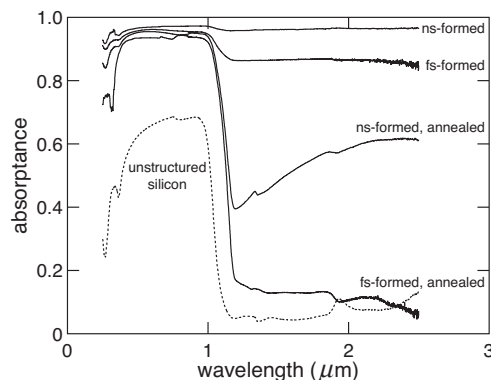


Figure 4.4: Wavelength dependence of absorbance for femtosecond-laser-formed and nanosecond-laser-formed microstructures, before and after thermal annealing at 875 K for 30 minutes (see Section 4.1.8). The absorbance of an unstructured silicon substrate is also shown.

formed structures were made using our standard conditions and the nanosecond-formed structures were made using the conditions listed in Section 3.4.1. Figure 4.4 shows the wavelength dependence of the absorbance of both structured surfaces and of the unstructured substrate silicon. The absorbance of the nanosecond- and femtosecond-formed structures is very similar: near-unity, featureless absorbance from  $0.4 \mu\text{m}$  to  $1 \mu\text{m}$ , a small decrease in absorbance around  $1.1 \mu\text{m}$  (the band edge of ordinary silicon), and strong featureless absorbance from  $1.1 \mu\text{m}$  to  $2.5 \mu\text{m}$ . The absorbance of the nanosecond-structured material (98% in the visible, 95% in the infrared) is somewhat higher than that of the femtosecond-structured material (95% in the visible, 85% in the infrared) across the measured spectral range. Annealing the structured surfaces at 875 K for 30 minutes (see Section 4.1.8) leaves the visible absorbance essentially unchanged, but dramatically decreases the below-band gap absorbance. The below-band gap absorbance of the nanosecond-structured samples changes less with annealing than that of the femtosecond-structured samples; further annealing of the nanosecond-structured samples for up to 12 hours causes little additional

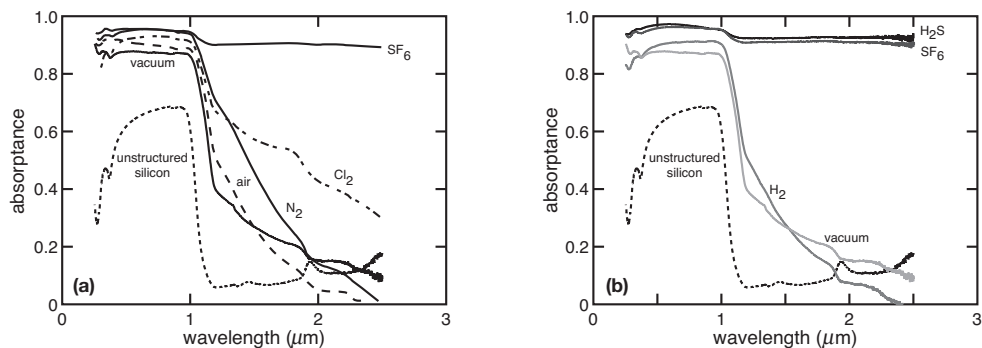


Figure 4.5: (a) Wavelength dependence of absorbance on the gas species used in microstructuring. The gases shown are those used in the morphology study (Section 3.7). The vacuum chamber was at a base pressure of less than  $10^{-6}$  bar for the vacuum sample. (b) Absorbance for a selection of gases that more directly shows the importance of sulfur in the high below-band-gap absorbance. All samples were made with 500 laser pulses and  $8 \text{ kJ/m}^2$  laser fluence.

change <sup>1</sup>.

#### 4.1.5 Effect of laser wavelength, polarization, and propagation direction

There is no measurable difference between the absorbance of silicon microstructured with 400 nm light and silicon microstructured with 800 nm light. Similarly, changing the polarization and propagation direction of the laser does not affect the measured absorbance.

#### 4.1.6 Effect of ambient gas

In this section, we examine the effect of the ambient gas species on the optical properties of microstructured silicon. We investigate the optical properties of microstructured silicon surfaces prepared in a number of gases (in addition to SF<sub>6</sub>). Figure 4.5 (a)

<sup>1</sup>In the  $40 \mu\text{m}$ -deep nanosecond-formed structures, the below-band gap absorbance should be significantly amplified by multiple reflections; geometric effects may be less important to the below-band gap absorption in the femtosecond-formed structures because these infrared wavelengths are not much less than the  $8 \mu\text{m}$  structure depth.

shows the absorptance of samples prepared in gases used in Section 3.7 (SF<sub>6</sub>, Cl<sub>2</sub>, N<sub>2</sub>, air, and vacuum). Microstructuring in SF<sub>6</sub> and Cl<sub>2</sub> brings about the most dramatic change in absorptance, with SF<sub>6</sub> having the highest absorptance of all the gases for the entire measured wavelength range. Samples made in air, N<sub>2</sub>, and vacuum show increased absorptance relative to unstructured silicon for most of the measured wavelengths ( $\lambda < 1.5 \mu\text{m}$  for air,  $\lambda < 1.77 \mu\text{m}$  for N<sub>2</sub>, and  $\lambda < 2.3 \mu\text{m}$  for vacuum). The reason the absorptance for these gases falls below that of unstructured silicon is unknown.

Although all samples show an increase in infrared absorption over unstructured silicon, samples structured in SF<sub>6</sub> are the only ones with near-unity, featureless absorptance across the entire measured spectrum. For samples made in air, N<sub>2</sub>, and vacuum, the gradual decrease of absorptance for wavelengths longer than  $1.2 \mu\text{m}$  is consistent with the presence of band tails of Urbach states due to a high density of defects [58]. Samples microstructured in Cl<sub>2</sub> have significantly increased infrared absorption; the infrared absorption for Cl<sub>2</sub> samples may be a combination of band tails from Urbach states and the large aspect ratio microstructures formed in this gas (Figure 3.19).

From this information, it appears that structuring in SF<sub>6</sub> is critical to the near-unity, below-band gap absorptance. To demonstrate that it is the presence of sulfur in the ambient gas that is critical, we compared the optical properties of samples structured in another set of gases (SF<sub>6</sub>, H<sub>2</sub>S, H<sub>2</sub>, and vacuum). Figure 4.5 (b) shows the absorptance for these gases as compared to unstructured silicon. The most significant chemical difference between H<sub>2</sub> and H<sub>2</sub>S is the presence (or lack) of sulfur. As shown in Figure 4.5 (b), the absorptance of H<sub>2</sub>S is nearly identical to that of samples made in SF<sub>6</sub>, while samples made in H<sub>2</sub> have absorptances that resemble samples made in vacuum. The information shown in Figure 4.5 (b) is compelling evidence that sulfur plays a vital role in the near-unity, below-band gap absorptance.

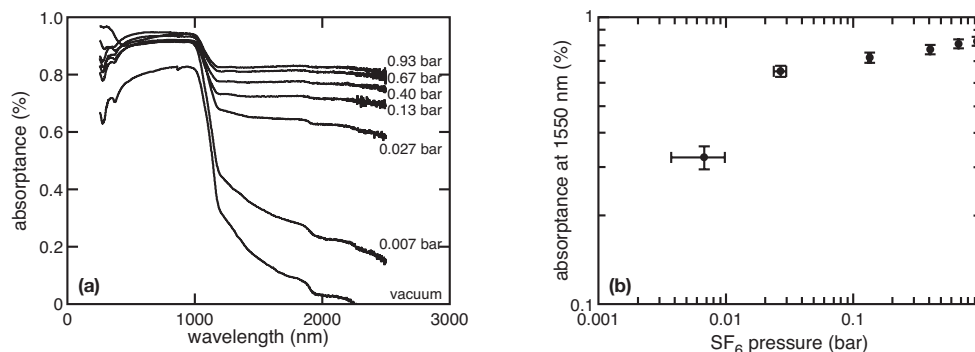


Figure 4.6: (a) Wavelength dependence of absorptance on the pressure of SF<sub>6</sub> used in microstructuring and (b) the dependence of absorptance at 1550 nm on the pressure of SF<sub>6</sub> used in microstructuring. The vacuum chamber was at a base pressure of less than  $10^{-6}$  bar for the vacuum sample.. All samples were made with 500 laser pulses and  $8 \text{ kJ/m}^2$  laser fluence.

#### 4.1.7 Effect of gas pressure

In this section, we examine the effect of the pressure of SF<sub>6</sub> on the optical properties of microstructured silicon. Figure 4.6 (a) shows that the absorptance increases with increasing SF<sub>6</sub> pressure. The largest variation in absorptance occurs for below-band gap wavelengths (Figure 4.6 (b)). The greatest rate of increase is observed at low pressures. Above 27 mbar, the below-band gap absorptance does not vary with wavelength, while at lower pressure, it decreases with increasing wavelength.

#### 4.1.8 Effect of annealing

In this section, we examine the effect of annealing on the optical properties of microstructured silicon. Figure 4.7 (a) shows the effect of annealing for thirty minutes at several temperatures on the absorptance of samples made under standard conditions. Annealing at temperatures below 575 K has little effect on the absorptance. Annealing between 575 K and 875 K does not affect absorptance above the band gap, but lowers

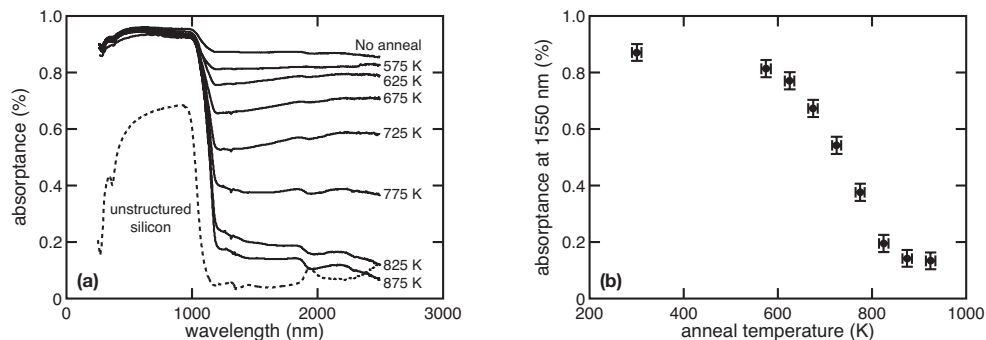


Figure 4.7: (a) Wavelength dependence of absorbance on anneal temperature (following microstructuring). The data point at room temperature (300 K) corresponds to a microstructured sample that was not annealed. (b) The dependence of absorbance at 1550 nm on anneal temperature (following microstructuring). All samples were made with 500 laser pulses and  $8 \text{ kJ/m}^2$  laser fluence in 0.67 bar  $\text{SF}_6$ , and were annealed for 30 minutes.

the below-band gap absorbance; the higher the temperature, the greater the decrease in absorbance (Figure 4.7 (b)). Raising the annealing temperature above 875 K does not produce any additional change. As shown in the last chapter (Figure 3.27), annealing has no visible effect on the shape of either the microstructures or the surface nanoparticles.

It should be noted that sulfur concentrations in the annealed samples, however, do not mirror the below-band gap absorbance (Table 3.1). Annealing is the only parameter (that we have Rutherford backscattering data on) for which below-band gap absorbance does not mirror sulfur concentration. Upon annealing a standard sample at either 725 K or 875 K for 30 minutes, the sulfur content in both cases decreases by only 40%, while the infrared absorbance decreases by almost an order of magnitude. The concentration of sulfur in the annealed samples is comparable to that of the sample made with  $4 \text{ kJ/m}^2$  and 500 pulses, or the sample made with ten pulses and  $8 \text{ kJ/m}^2$ ; for these samples, the infrared absorbance is only 20% less than that of a standard sample.

### 4.1.9 Effect of silicon substrate properties

In our work thus far, we have found little, if any, effect on the optical properties of microstructured silicon from the following substrate properties: Crystalline orientation, dominant carrier ( $n$ - or  $p$ -doping), dopant concentration (resistivity), and presence or absence of a native oxide layer before irradiation.

## 4.2 Electronic measurements

For a limited number of parameters, we took a combination of resistivity and Hall effect measurements [59] in order to determine the electronic properties of the disordered surface layer following microstructuring in  $\text{SF}_6$ . From this information we are able to determine the sheet resistance, dominant carrier sign, sheet carrier density, Hall mobility, and approximate values for resistivity and bulk-carrier density.

### 4.2.1 Hall effect and resistivity measurements: procedure and apparatus

Much of the information presented in this section, along with design elements for our apparatus, is found at a wonderful online-tutorial from the National Institute of Standards and Technology (NIST) [59]. If the reader is interested in learning more about these measurements, they are strongly recommended to visit this website.

For resistivity and Hall effect measurements, we employ the van der Pauw technique, a widely used technique for accurately determining resistivity of semiconductor samples [60]. Briefly, one uses an arbitrarily shaped, thin-plate sample containing four very small ohmic contacts placed at the edges of the sample and measure two characteristic resistances associated with the contacts. With these characteristic resistances, the sheet resistance and bulk electrical resistivity of the sample can be calculated. The strength of

the van der Pauw technique is that it minimizes error from asymmetries in sample geometry and resistances introduced by contacts.

### Sample preparation

For the van der Pauw technique, we need to make ohmic electrical contact to four points on the disordered surface layer. For accurate measurements, it is preferable to have a thin sample and to have a suitable geometry for the electrical contacts. We naturally fulfill the first condition because the measurements we are making are for the thin surface layer<sup>2</sup>. For a suitable contact geometry, the average diameters ( $D$ ) of the contacts, and sample thickness ( $d$ ) must be much smaller than the distance between the contacts ( $L$ ). Relative errors caused by non-zero values of  $D$  are of the order of  $D/L$ . The preferred geometry for the contacts is a cloverleaf setup, but a square or rectangle geometry (with the contacts at the four corners) is acceptable; we use a square geometry for our measurements.

In order to make electrical contact to our samples, we do the following: first a microstructured sample is dipped in a 5% HF solution for 5 minutes to remove the native oxide layer. Next, with a mask covering all but the very corners of  $10 \times 10 \text{ mm}^2$  microstructured areas, samples are placed in a thermal evaporator and we evaporate chrome/gold (Cr/Au) contacts onto the four corners. We then use a dicing saw to cut 0.25 mm slivers from each side. Cutting the sample edges ensures that the contacts are only connected to the surface layer and do not touch the substrate layer. Finally, we use a wire bonder to connect the contacts on the corner of the samples to four Cr/Au contact pads evaporated onto a glass slide. This arrangement allows us to make repeatable contact to each of the corner contacts on the microstructured surface. For clarity, we number each of the corners

---

<sup>2</sup>Although not apparent at this point, it is a reasonable assumption that we only measure the properties of the microstructured layer because it has drastically different electronic properties than the substrate wafer. This will become more clear later in this chapter.

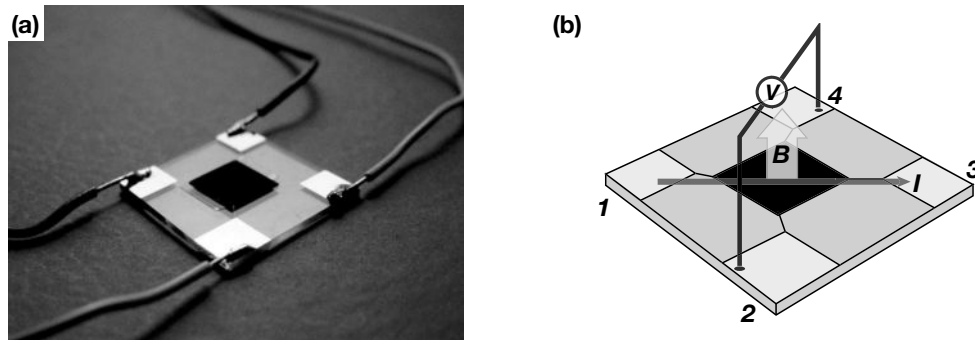


Figure 4.8: (a) A picture of a sample prepared for resistivity and Hall effect measurements. (b) A schematic diagram of how Hall voltage measurements are done. The current flowing through a strong magnetic field creates a voltage normal to both the current and the magnetic field. This is called the Hall effect. The numbers are indices used to keep track of how the current/voltage is being applied/measured.

(1,2,3,4) in counter-clockwise ascending order (See Figure 4.8 (b)). From this point on, when we refer to voltages or currents between two corners we use  $V$  and  $I$  with the corner numbers as indices. For example, a voltage measured from corner 1 and 2 ( $V_1 - V_2$ ) is listed as  $V_{12}$ . Figure 4.8 (a) shows a sample prepared for measurement.

### Resistivity

The procedure for making resistivity ( $\rho$ ) measurements is as follows: we first apply a small DC current ( $10 \mu\text{A}$ ) from corner 2 to corner 1 ( $I_{21}$ ). The current should be small enough to ensure that power dissipation is negligible. In general, for a measured resistance  $R$  between corners,  $I$  should satisfy

$$I < (200R)^{-0.1}. \quad (4.2)$$

We then measure the voltage from corner 3 to corner 4 ( $V_{34}$ ). We repeat this measurement for the reversed polarity (apply  $I_{12}$  and measure  $V_{43}$ ). Similarly, we measure six more voltages ( $V_{41}$ ,  $V_{14}$ ,  $V_{12}$ ,  $V_{21}$ ,  $V_{23}$ , and  $V_{32}$ ). From these measurements we calculate eight resistances,

$$R_{21,34} = V_{34}/I_{21}, R_{12,43} = V_{43}/I_{12}, \quad (4.3)$$

$$R_{32,41} = V_{41}/I_{32}, R_{23,14} = V_{14}/I_{23}, \quad (4.4)$$

$$R_{43,12} = V_{12}/I_{43}, R_{34,21} = V_{21}/I_{34}, \quad (4.5)$$

$$R_{14,23} = V_{23}/I_{14}, R_{41,32} = V_{32}/I_{41}. \quad (4.6)$$

The second half of this sequence of measurements is redundant. Also, as will become apparent in the next chapter, these measurements should be made in the dark to remove contributions from photovoltaic and photoconductive effects.

From these four measured resistances we calculate two characteristic resistances  $R_A$  and  $R_B$ ,

$$R_A = (R_{21,34} + R_{12,43} + R_{43,12} + R_{34,21})/4, \quad (4.7)$$

$$R_B = (R_{32,41} + R_{23,14} + R_{14,23} + R_{41,32})/4. \quad (4.8)$$

With these characteristic resistances we calculate the sheet resistance,  $R_S$ , by numerically solving the van der Pauw equation,

$$e^{-\pi R_A/R_S} + e^{-\pi R_B/R_S} = 1, \quad (4.9)$$

by iteration. The bulk electrical resistivity ( $\rho$ ) is the sheet resistance ( $R_S$ ) times the sample thickness ( $d$ ).

### Hall measurements

For readers unfamiliar with the Hall effect or Lorentz force, it is recommended that they visit the NIST website listed above [59]. Briefly, the Lorentz force refers to the force on a charged particle while it moves in an applied magnetic field. Electrons (or holes)

moving perpendicular to an applied magnetic force experience a force normal to both the direction of flow and the direction of the applied field; the direction of deflection depends on the sign of the charge. For a current flowing through a semiconductor in the presence of a strong magnetic field, the Lorentz force causes a build up of charge to one side of the semiconductor. The charge build up results in a voltage, the Hall voltage, across the sample in the direction of carrier deflection. By experimentally measuring this voltage, we can determine the sign of the carrier and the sheet carrier density ( $n_s$  for electrons and  $p_s$  for holes). This, combined with resistivity measurements, can be used to determine the Hall mobility ( $\mu$ ).

Our Hall measurement procedure is as follows: we take the same samples used for resistivity measurements and place them inside a strong applied magnetic field (several thousand gauss). The sample is oriented such that the magnetic field is perpendicular to the silicon surface and defined as positive if the field lines enter the back and leave from the front of the sample. We then apply a small AC current (about 1–2  $\mu\text{A}$ ) from contact one to contact three ( $I_{13}$ ) and measure the voltage across contacts 2 and 4 ( $V_{24P}$ , where P indicates a positive magnetic field). Figure 4.8 shows a schematic diagram of this procedure<sup>3</sup>. We then reverse the current ( $I_{31}$ ) and measure the voltage ( $V_{42P}$ ). Similarly we measure  $V_{13P}$  and  $V_{31P}$ , then reverse the direction of the magnetic field, and measure  $V_{24N}$ ,  $V_{42N}$ ,  $V_{13N}$ , and  $V_{31N}$ . With these measurements made we can calculate four characteristic voltages,

$$V_C = V_{24P} - V_{24N}, \quad (4.10)$$

$$V_D = V_{42P} - V_{42N}, \quad (4.11)$$

$$V_E = V_{13P} - V_{13N}, \quad (4.12)$$

$$V_F = V_{31P} - V_{31N}. \quad (4.13)$$

---

<sup>3</sup>The Hall voltage can be very small at times and, as such, we used a lock-in amplifier, locked to the frequency of the input current, to measure the voltage. In addition, the applied current and magnetic field strength were varied to maximize signal and minimize noise.

If the the sum of these four voltages,

$$V_S = V_C + V_D + V_E + V_F, \quad (4.14)$$

is negative, the dominant carriers are electrons ( $n$ -type). If the sum is positive, the dominant carriers are holes ( $p$ -type). We then calculate the sheet carrier density (in units of  $\text{cm}^{-2}$ ) with

$$p_s = \frac{8 \times 10^{-8} IB}{qV_S} \quad (4.15)$$

$$n_s = \left| \frac{8 \times 10^{-8} IB}{qV_S} \right|, \quad (4.16)$$

where  $B$  is the magnetic field in gauss and  $I$  is the current in amperes (A). The bulk carrier density is then simply the sheet carrier density ( $n_s$  or  $p_s$ ) divided by the sample thickness ( $d$ ). With the sheet carrier density and the sheet resistance determined, we calculate the Hall mobility (in units of  $\text{cm}^2\text{V}^{-1}\text{s}^{-1}$ ) with

$$\mu = \frac{1}{qn_s R_S}. \quad (4.17)$$

### 4.2.2 Results

To ensure that our measurement technique is valid, we performed these measurements on an  $n$ -doped,  $\rho = 800 - 1200 \Omega\cdot\text{cm}$ , unstructured wafer. We measured a resistivity of  $957 \Omega\cdot\text{cm}$  and a mobility of  $1101.2 \text{ cm}^2\text{V}^{-1}\text{s}^{-1}$  (in close agreement with literature values [39]). The data we present is in the form of sheet carrier density and sheet resistance instead of bulk density and bulk resistivity. We present the data in terms of sheet values rather than bulk values because these are the actual measured quantities and we do not know the thickness ( $d$ ) of our surface layer with good precision.

Original doping	Average fluence (kJ/m <sup>2</sup> )	Doping after structuring	Sheet resistance $R_S$ ( $\Omega$ )	Sheet carrier density $n_s$ (cm <sup>-2</sup> )	Hall mobility $\mu$ (cm <sup>2</sup> V <sup>-1</sup> s <sup>-1</sup> )
$n$	unstructured	-	31931	$1.78 \times 10^{11}$	1101
$n$	4.0	$n$	4865	$7.37 \times 10^{12}$	174
$n$	6.0	$n$	4992	$7.15 \times 10^{12}$	175
$n$	8.0	$n$	6253	$4.52 \times 10^{12}$	221
$n$	10.0	$n$	4554	$8.83 \times 10^{12}$	155

Table 4.1: Electronic properties of microstructured silicon for several fluences. The original substrate used for all samples is an  $n$ -doped,  $\rho = 800$ – $1200 \Omega\cdot\text{cm}$  wafer.

### Effect of fluence

There is no recognizable trend in the electronic properties with increasing fluence. The sheet resistance, carrier density, and mobility for all four fluences is similar. However, there are some important results contained within Table 4.1. Microstructuring silicon results in a higher sheet carrier density than the original substrate, which means that microstructuring  $n$ -dopes the surface. We somewhat expected  $n$ -doping because sulfur is incorporated into the surface and a sulfur atom has two more valence electrons than silicon. The increase in carrier density is likely the reason for the drop in sheet resistance. Also, the mobility of electrons in the disordered surface layer is an order of magnitude less than the unstructured crystalline wafer. The mobility is decreased because of disorder in the structure of the surface layer; with crystalline order over only tens of nanometers, the carriers' mean free path is greatly diminished compared to the mean free path of carriers in a single crystal substrate.

**Effect of annealing**

Original doping	Average fluence (kJ/m <sup>2</sup> )	Annealing temperature (30 minutes)	Sheet resistance $R_S$ ( $\Omega$ )	Sheet carrier density $n_s$ (cm <sup>-2</sup> )	Hall mobility $\mu$ (cm <sup>2</sup> V <sup>-1</sup> s <sup>-1</sup> )
$n$	4.0	-	4865	$7.37 \times 10^{12}$	174
$n$	4.0	825 K	8433	$7.34 \times 10^{12}$	101
$n$	4.0	1075 K	2749	$1.88 \times 10^{13}$	121
$n$	8.0	-	6253	$4.52 \times 10^{12}$	221
$n$	8.0	825 K	6147	$1.92 \times 10^{13}$	53

Table 4.2: Electronic properties of microstructured silicon for two annealing temperatures. The original substrate used for all samples is an  $n$ -doped,  $\rho = 800\text{--}1200 \Omega\text{-cm}$  wafer.

Table 4.2 shows the effect of annealing to two different temperatures on the electronic properties of microstructured silicon. Although these data do not represent a large cross section of samples, we see that annealing to high temperatures increases sheet carrier density. We saw in the last chapter that annealing does not change the sulfur content significantly and, if anything, the sulfur content is diminished. However, the level of  $n$ -doping increases significantly with annealing at 1075 K. The second observation to note is that an anneal at 825 K does not affect the sheet carrier density significantly but seems to frustrate the conduction of carriers; the resistance increases and the mobility is significantly decreased. Annealing at 1075 K, however, greatly increases the sheet carrier density but does not decrease the mobility as significantly.

### Effect of original substrate properties

In this section, we examine the effect of using a  $p$ -doped substrate (rather than  $n$ -doped) and how annealing and fluence affect the electronic properties of structured  $p$ -doped substrates.

Original doping (resistivity)	Average fluence (kJ/m <sup>2</sup> )	Doping after structur- ing/annealing	Sheet resistance $R_S$ ( $\Omega$ )	Sheet carrier density $n_s(p_s)$ (cm <sup>-2</sup> )	Hall mobility $\mu$ (cm <sup>2</sup> V <sup>-1</sup> s <sup>-1</sup> )
$n$ ( $\rho=900 \Omega\cdot\text{cm}$ )	4.0	$n$	4865	$7.37 \times 10^{12}$	174
$p$ ( $\rho=10 \Omega\cdot\text{cm}$ )	4.0	$p$	164	$1.4 \times 10^{14}$	271
$p$ ( $\rho=100 \Omega\cdot\text{cm}$ )	4.0	$p$	5167	$(7 \times 10^{14})$	(1)
$p$ ( $\rho=10 \Omega\cdot\text{cm}$ )	3.0	$p$	199	$1.34 \times 10^{14}$	1392
$p$ ( $\rho=100 \Omega\cdot\text{cm}$ )	3.0	$p$	1492	$4.77 \times 10^{13}$	27

Table 4.3: Electronic properties of microstructured silicon for  $p$ -doped substrates. The measurement for sheet carrier density of a  $p$ -doped, 100  $\Omega\cdot\text{cm}$  substrate and an average fluence of 4.0 kJ/m<sup>2</sup> is likely imprecise.

Table 4.3 shows electronic measurements of  $p$ -doped substrates following structuring with two different fluences. The most significant result is that, after microstructuring a  $p$ -doped substrate with low fluence (3 or 4 kJ/m<sup>2</sup>), the surface remains  $p$ -doped. The  $n$ -doping from the sulfur-implantation is not enough to cancel out the original  $p$ -doping<sup>4</sup>. The measurement of sheet carrier density and mobility of a  $p$ -doped ( $\rho = 100 \Omega\cdot\text{cm}$ ) sample irradiated with a fluence of 4.0 kJ/m<sup>2</sup> is likely imprecise. The Hall voltage for this sample was extremely small and difficult to distinguish from the noise. We think that this is because these conditions lead to a near perfect cancellation of original hole-doping and

<sup>4</sup>It should be noted that, in order to reach resistivities in  $p$ -doped substrates that are comparable to  $n$ -doped substrates, the sheet carrier density of holes must be significantly higher due to their lower mobilities [39]

implanted electrons. Effectively, the disordered surface layer was near to intrinsic silicon and, combined with the highly disordered structure, the Hall voltage is small and difficult to measure.

Original doping (resistivity)	Average fluence (kJ/m <sup>2</sup> )	Doping after structur- ing/annealing	Sheet resistance $R_S$ ( $\Omega$ )	Sheet carrier density $n_s(p_s)$ (cm <sup>-2</sup> )	Hall mobility $\mu$ (cm <sup>2</sup> V <sup>-1</sup> s <sup>-1</sup> )
$p$ ( $\rho=10 \Omega\cdot\text{cm}$ )	4.0	$p$	164	$1.4\times 10^{14}$	271
$p$ ( $\rho=10 \Omega\cdot\text{cm}$ )	4.0 (annealed)	$n$	2080	$1.14\times 10^{14}$	26
$p$ ( $\rho=10 \Omega\cdot\text{cm}$ )	3.0	$p$	199	$1.34\times 10^{14}$	1392
$p$ ( $\rho=10 \Omega\cdot\text{cm}$ )	3.0 (annealed)	$n$	1492	$1.54\times 10^{14}$	27
$p$ ( $\rho=100 \Omega\cdot\text{cm}$ )	4.0	$p$	5167	$(7\times 10^{14})$	(1)
$p$ ( $\rho=100 \Omega\cdot\text{cm}$ )	4.0 (annealed)	$n$	2607	$4.56\times 10^{13}$	53
$p$ ( $\rho=100 \Omega\cdot\text{cm}$ )	3.0	$p$	1492	$4.77\times 10^{13}$	27
$p$ ( $\rho=100 \Omega\cdot\text{cm}$ )	3.0 (annealed)	$n$	3351	$3.71\times 10^{13}$	50

Table 4.4: Electronic properties of microstructured silicon for  $p$ -doped substrates after annealing. The dominant carrier changes from holes to electrons upon annealing. All annealed samples were annealed to 1075 K for 30 minutes.

Table 4.4 examines the effect of annealing on the electronic properties of microstructured  $p$ -doped wafers. Following microstructuring at lower fluences (3 and 4 kJ/m<sup>2</sup>) the originally  $p$ -doped wafers remain  $p$ -doped. However, after annealing at 1075 K for 30 minutes, the surface layer becomes  $n$ -doped. The sulfur content does not change significantly, but the change in carrier concentration is so drastic that it *reverses* the sign of the dominant carrier. We believe that this indicates that annealing causes a change in the local bonding/electronic environment of implanted sulfur atoms, increasing the number of

free carriers by decreasing the coordination number or annihilating defects. We discuss this further in the following section.

### 4.3 Discussion

Silicon surfaces microstructured in the presence of  $\text{SF}_6$  have interesting and unique optical properties, namely near-unity absorptance from 250 nm to 2500 nm; This spectral range includes wavelengths well below the band-gap of crystalline silicon, which normally pass through silicon unabsorbed. In addition to being scientifically interesting, it is also of great interest in optoelectronic applications (see Chapter 5). For several years, we have tried to identify the mechanism responsible for the remarkable optical properties. We use the information contained in this chapter to speculate on the subject.

For visible wavelengths, the increased absorption is a result of the morphology of the microstructured surface. The conical nature of the microstructures leads to multiple reflections for incoming light. That is, a photon incident onto the structured surface is likely to undergo more than one reflection before leaving the surface. With the steep conical geometry of our microstructures, calculations show that, on average, a photon undergoes approximately four reflections before escaping [20]. At each reflection, incident light absorbed by the intrinsic visible absorptance of ordinary silicon ( $\sim 65\%$ ) quickly raises the total absorptance to over 90%.

Surface roughening is a common method for decreasing reflectance and increasing absorption. For decreasing acoustic reflections, anechoic surfaces are commonly seen in lecture halls and airports. Nature uses roughened surfaces to enhance night vision in nocturnal insects [61] and for more efficient absorption in flower petals [62]. In silicon optoelectronics, many different surface structuring techniques are used to increase absorption, such as wet

etching [63, 64], reactive ion etching [65, 66], and thin-films of porous silicon [67].

A roughened surface morphology explains the increased absorption in the visible but does not explain the near-unity absorption for below-band gap wavelengths. Simply roughening a surface does not increase absorption for wavelengths of light that are not absorbed in the first place. For instance, roughened glass still transmits visible light, albeit diffusely, as one sees with frosted glass. At best, the absorptance of crystalline silicon at wavelengths longer than  $1.1 \mu\text{m}$  is 5-6%, and four reflections does not bring the absorptance up to 90%. Therefore, for below-band gap wavelengths, the only way to have near-unity absorptance is if microstructuring alters the band structure of the surface layer. However, determining how the band is altered is not an easy task. It is apparent from information presented in this chapter that sulfur plays a critical role in the high below-band gap absorption (Figure 4.5). We contend that it is not just the presence of sulfur, but, more importantly, the local electronic environment of the sulfur atoms that alters the band structure and leads to the unique optical properties.

There is ample evidence that sulfur is, in some way, responsible for the below-band gap absorption. Samples microstructured in  $\text{SF}_6$  or  $\text{H}_2\text{S}$  (Figure 4.5) are the only ones that exhibit near unity absorption across the entire measured spectrum; microstructuring in gases that do not contain sulfur does not produce comparable below-band gap absorption. Changing the pulse duration drastically changes the surface morphology but femtosecond-formed and nanosecond-formed structures have similar optical properties and sulfur content (Figure 4.4). Recently we found that using a powder of elemental sulfur spread across a sample surface has the same effect on the optical properties as using  $\text{SF}_6$  as an ambient gas [68]. Chemical composition information from Chapter 3 shows that sulfur is incorporated at very high levels for all experiments with  $\text{SF}_6$ . We also know that sulfur content and absorptance are intimately connected; both of these values increase with shot number and

fluence (and likely with gas pressure).

We are therefore able to assert with confidence that sulfur incorporation is responsible for below-band gap absorptance. However, the way in which sulfur incorporation alters the band structure is more difficult to determine. To propose an answer, we use the information we have on the disordered surface layer structure and chemical composition, and how these factors correlate with optical and electronic properties.

The one particular experimental parameter that sticks out from the others is annealing. It sticks out because, unlike other experimental parameters, annealing causes the below-band gap absorptance to decrease in a manner that does not mirror the sulfur concentration. For example, samples annealed at 725 K and at 875 K have the same sulfur concentration, but the absorptance at 1550 nm of the sample annealed at 725 K is five times that of the sample annealed at 875 K. Also, the observed sulfur concentration in the sample annealed at 875 K is the same as that from the 10-pulse or 4-kJ/m<sup>2</sup> samples, but the 10-pulse and 4-kJ/m<sup>2</sup> samples display 80% of the below-band gap absorptance of a standard sample, while the below-band gap absorptance of the sample annealed at 875 K is reduced to essentially the same value as the original substrate silicon.

The most likely explanation of the below-band gap absorption is that laser microstructuring incorporates the sulfur impurities into the silicon matrix in optically active states, and annealing causes bond rearrangement within the silicon matrix that renders the sulfur impurities optically inactive. Following irradiation with an intense shot-pulse laser, the resolidification front of the molten layer is sufficiently fast that it can trap impurity atoms in a nonequilibrium configuration [69]. Indeed, sulfur concentrations we measure in microstructured surfaces exceed the equilibrium solubility of sulfur in crystalline silicon [70] by many orders of magnitude, indicating that sulfur is incorporated through a highly nonequilibrium process. Annealing then allows the lattice to relax toward a more ther-

modynamically stable configuration. The optically active states could be the result of any number of defects including changes in coordination number, bond length, and/or bond angle of neighboring atoms. The concentration levels of sulfur we measure in the surface are more than sufficient to create an impurity/defect band of energy levels within the band gap [71]. Deactivation during annealing is likely from rearrangement of these bonding properties or annihilation of defects toward a more stable configuration. Annealing at 875 K for 30 minutes would permit defect annihilation [72] and diffusion of sulfur over several hundred nanometers [39].

Another strong piece of evidence that supports bonding rearrangement and defect annihilation comes from the effect of annealing on the electronic properties. Following microstructuring, p-doped substrates still have holes as their dominant charge carrier, despite the addition of nearly 1 at. % sulfur with two possible donor electrons per atom. However, after annealing, the dominant carrier in the microstructured surfaces switches to electrons. This change in dominant carrier occurs with no significant change in the sulfur content. Before annealing the sulfur is incorporated in the surface in such a way that its donor electrons do not contribute to conduction; the donor electrons are likely locked up in a trap, or perhaps the coordination number of the implanted sulfur is larger than four. Then, during annealing, the bonding arrangements change and donor electrons are freed up to contribute to conduction. The number of electrons being released is large enough to eliminate the holes as charge carriers and turn the surface into an  $n$ -doped one with sheet carrier concentrations on the order of  $10^{14} \text{ cm}^{-2}$ .

We do not expect that crystallinity plays an important role. Annealing temperatures that completely eliminate the below-band gap absorptance are much lower than the temperatures at which significant grain growth would be expected in microcrystalline or polycrystalline silicon [73]. In addition, the pulse duration experiments indicate that the

disordered layer covering the femtosecond-formed structures is not essential for below-band gap absorption, as both transmission electron microscopy and Rutherford backscattering spectrometry indicate that the nanosecond-formed structures are nearly single-crystal. The optically active configuration of sulfur may be able to exist in either the single crystal nanosecond-formed structures or the highly disordered femtosecond-formed structures; the optical deactivation process must not require a significant increase in the crystallinity of the femtosecond-formed structures. Alternatively, different optically active configurations of sulfur could be present in the femtosecond-formed and nanosecond-formed structures, although none of our results directly suggest this interpretation. Also, collaborators of ours have been able to demonstrate below-band-gap absorption in a crystalline silicon surface doped with comparable levels of sulfur using ion-implantation followed by laser-annealing [74].

The location and electronic environment of the sulfur atoms before and after annealing is not well known and further work is needed to understand the mechanism by which the sulfur incorporation leads to below-band gap absorption. The disordered surface layer of femtosecond-formed structures is likely to provide a wide variety of possible electronic environments for the sulfur impurities. We are getting much closer to understanding the mechanism and work is ongoing towards solving this problem. We have recently demonstrated that implantation of other chalcogens (selenium and tellurium) also leads to near-unity below-band gap absorptance [68]. From these experiments we are learning a great deal about the local electronic and structural environment of the impurity atoms.

In summary, it is the incorporation of sulfur atoms into an optically active, nonequilibrium, and highly defective configuration that leads to the unique below-band gap absorptance for samples microstructured in  $\text{SF}_6$ . Annealing causes bond rearrangement and defect annihilation within the silicon matrix that renders the sulfur impurities optically inactive.

## Chapter 5

# Femtosecond-laser microstructured silicon photodiodes

In the previous two chapters, we presented all that we know about how experimental parameters affect the morphology, chemical composition, optical properties, and electronic properties of laser microstructured silicon. Of these results, the near-unity absorptance from ultraviolet wavelengths to the near-infrared for samples microstructured in SF<sub>6</sub> is of particular interest. Extending the spectral range of silicon-based photodetectors is an active area of research because of silicon's low cost and ease of integration with microelectronics. In this chapter, we describe our efforts toward creating a silicon-based photodiode that takes advantage of the extended optical absorption range of silicon microstructured in SF<sub>6</sub>. We use the information from the last two chapters to help us design our photodiode and understand the resulting behavior.

We begin the chapter with a basic discussion of photodiode operation by describing the most basic and prevalent type of photodiode, the *p-n* photodiode. We then describe the procedure for making laser-microstructured silicon photodiodes and examine how ex-

perimental parameters affect the performance of these devices. The information from the previous chapters assist us in optimizing and understanding the behavior of our photodiodes.

## 5.1 Introduction to photodiodes: the $p$ - $n$ junction

Before we discuss the creation of laser microstructured silicon photodiodes, we must first describe the basic operation and principles of a photodiode. That is, we must understand the structure of a photodiode and, most importantly, how a photodiode detects light. We present here a basic description of photodiodes and refer the reader to several references for further information on these thoroughly studied devices [39, 75, 36, 76].

There are many types of semiconductor photodiode devices ( $p$ - $n$  or  $p$ - $i$ - $n$  photodiodes, avalanche photodiodes, Schottky-barrier photodiodes, heterojunction photodiodes, *etc.*). For the purposes of this dissertation, we discuss one of the more basic devices, the  $p$ - $n$  photodiode; this particular photodiode is created by the junction between two of the same semiconductor material (a homojunction) with different impurity concentrations. Specifically, a homojunction where the impurity concentration changes abruptly from acceptor impurities ( $p$ -doped) to donor impurities ( $n$ -doped)<sup>1</sup>. Although the  $p$ - $n$  homojunction is a simplified example, the ideas presented can be extended to other photodiode devices and, for that matter, *all* other semiconductor devices.

We begin by considering two separated pieces of similar semiconductor material, one doped with acceptor impurity atoms ( $p$ -type) and one doped with donor impurity atoms ( $n$ -type), both electrically neutral. If we bring the two pieces into contact with one another, there will be a large gradient in carrier concentration at the interface (junction).

---

<sup>1</sup>Much of the basic theory of  $p$ - $n$  junctions was developed by Shockley shortly after he helped invent the transistor [77].

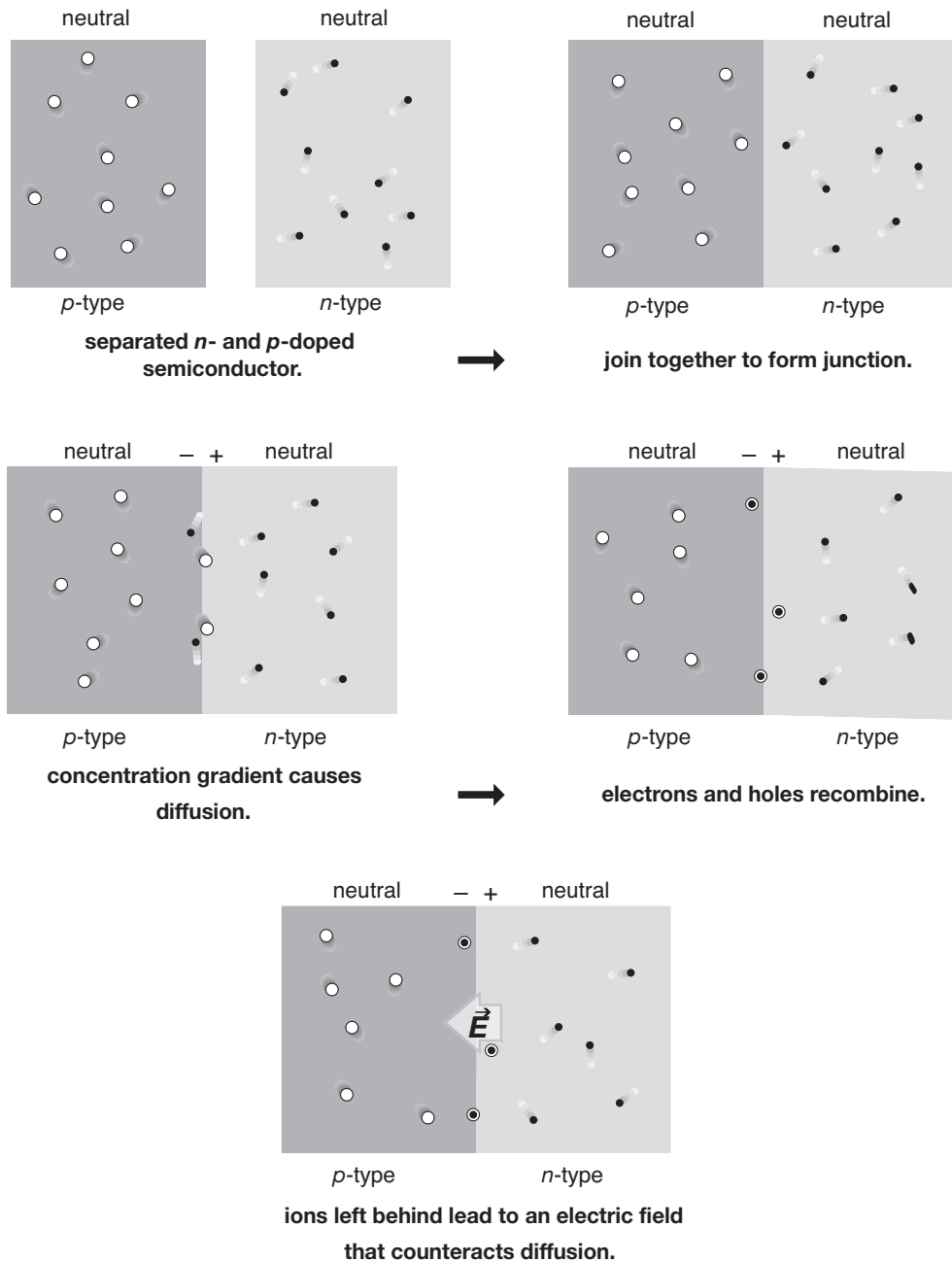


Figure 5.1: Cartoons illustrating the steps that lead to the contact potential and electric field build up in a *p-n* junction.

After all, one side is doped with electrons and the other, holes. The difference in carrier concentration causes a diffusion potential across the junction; electrons and holes begin to

diffuse across the junction to areas of lower concentration. As they cross to the other side of the junction they recombine with their oppositely charged electrical counterparts in the region very close to the junction. The recombined carriers are trapped on the far side of the junction and leave behind immobile ions (called space charges) on the side from which they came. As the number of space-charges increases (positively charged for the  $n$ -type side and negatively for the  $p$ -type), a potential difference builds up, which results in an electric field in the direction opposite the diffusion potential. If this process progresses to thermal equilibrium, the internal electric field exactly cancels the diffusion potential and charge diffusion stops. Once thermal equilibrium is reached, there is a thin insulating layer near the junction in which all charge carriers have been depleted by recombination (depletion region) and a strong electric field and large potential difference (the contact potential  $V_c$ )<sup>2</sup> exist. Figure 5.1 illustrates the steps resulting in the build up of a contact potential and internal electric field. Figure 5.2 shows the junction at thermal equilibrium, along with potential variation near the junction and energy-band diagram. Again, this explanation is conceptual and simplifies the considerations necessary for a rigorous physical description of the  $p$ - $n$ -junction.

Now, let us consider what happens if we take the junction out of equilibrium by applying an external electric field<sup>3</sup> (see Figure 5.3). The first case we consider is an applied electric field that reinforces the internal field. The field pushes the holes in the  $p$ -doped side to the left and the electrons in the  $n$ -doped to the right. This expands the insulating depletion region and increases both the internal electric field and the potential difference across the junction. In this case, no current flows; this arrangement is called the back bias condition. Next, we consider an applied electric field that is opposite the internal field.

---

<sup>2</sup>Typical potential differences in silicon based devices are around 0.8 V [39] over a depletion region of a few hundred nanometers.

<sup>3</sup>For clarification, the way in which we apply an external electric field is to apply a bias voltage across the two sides of the junction.

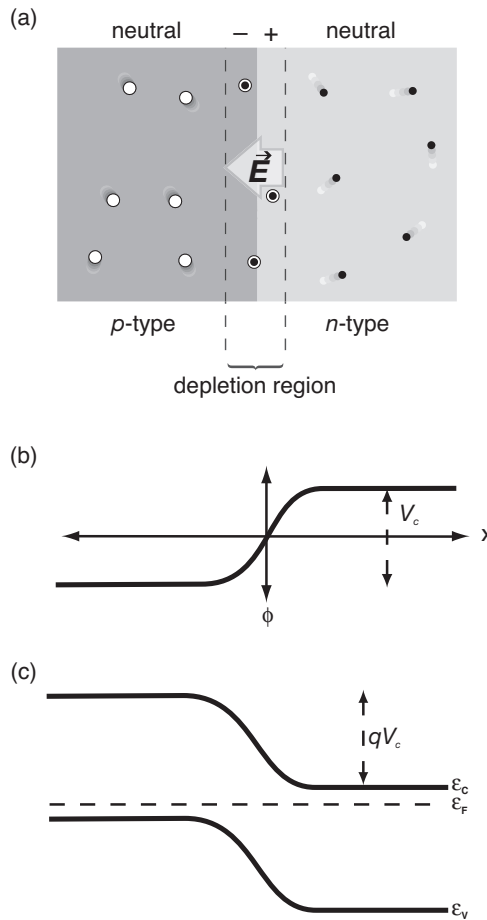


Figure 5.2: (a) A cartoon illustrating the final state of a  $p$ - $n$  junction in thermal equilibrium. Also shown are the (b) potential variation with distance and (c) the energy-band diagram.  $V_c$  is the contact potential.

In this case, the applied field shrinks the depletion region, diminishing the internal electric field and potential difference across the junction. Current flows with electrons being injected from the right and holes injected (electrons leaving) from the left, replenishing carriers that recombine at the junction. The current increases quickly with increasing external field; this arrangement is called the forward bias condition. From this discussion, we see that the  $p$ - $n$  junction allows current to flow in only one direction, *i.e.* it rectifies the current. This is the familiar electronic behavior of a diode. The characteristic current-voltage ( $I$ - $V$ ) behavior

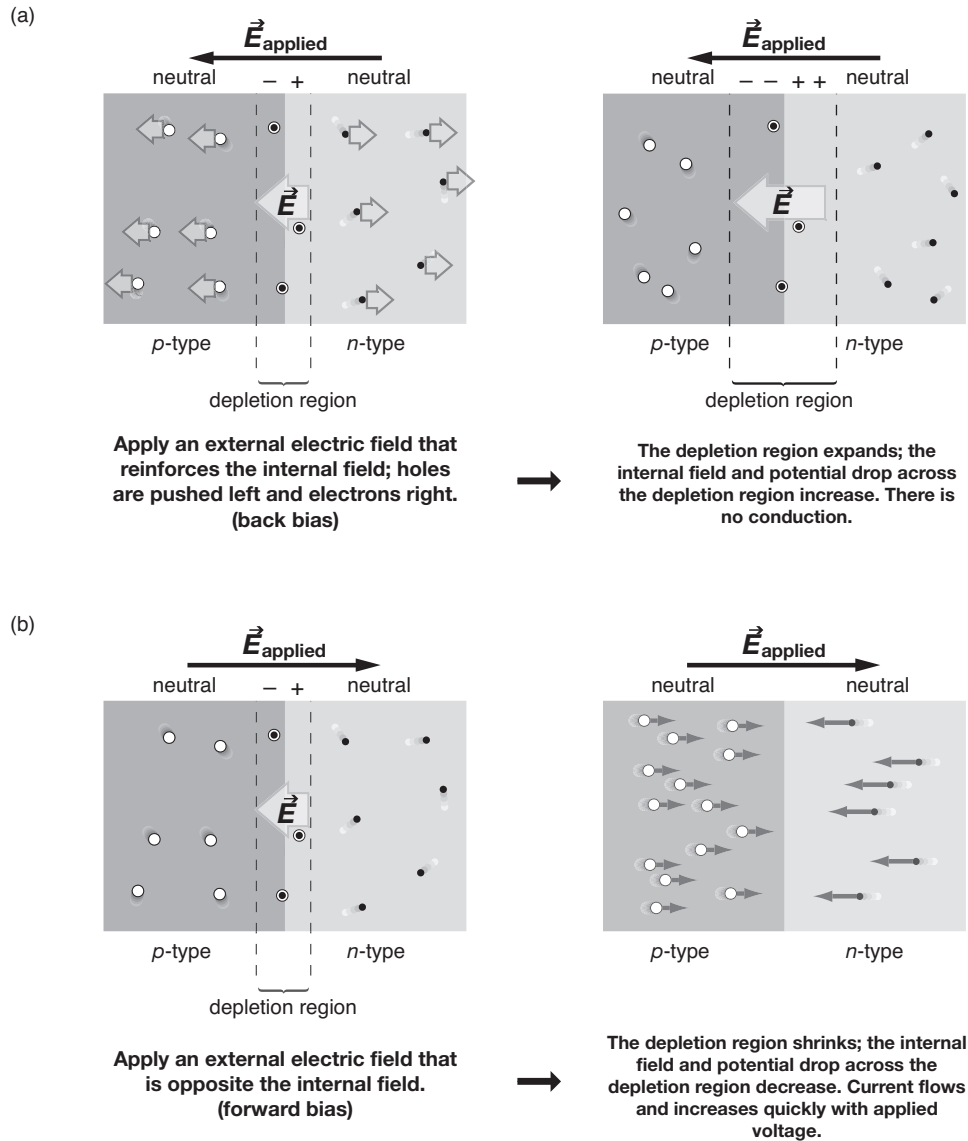


Figure 5.3: (a) Cartoon illustrating a *p-n* junction under the influence of an externally applied electric field that reinforces the internal field. This is called the back biased condition. (b) Cartoon illustrating a *p-n* junction under the influence of an externally applied electric field opposite the internal field. This is called the forward biased condition.

of a diode is critical in the operation of photodiodes.

Let us now consider the rectification behavior a little more closely by looking at the factors that contribute to current flow. For this discussion, we define a positive current

contribution as that coming from a hole moving from left to right or, similarly, an electron moving from right to left in the above cartoons. In an ideal  $p$ - $n$  diode there are two major contributions to the current across the junction. These are the the generation current ( $I_{gen}$ ) and the recombination current ( $I_{rec}$ ). The generation current refers to the current from electron-hole pairs that are thermally created within the depletion region. For a given set of conditions (mobility, temperature, carrier lifetime, carrier concentration, *etc.*) there is a statistical rate at which electron-hole pairs are spontaneously generated within the depletion region (thus the name generation current). If an electron-hole pair is created in the depletion region, the strong internal electric field immediately separates the pair and the electron and hole contribute to current flow across the junction. The generation current is negative by our definition, typically small ( $< 1 \mu\text{A}$ ), and has many names including the saturation current and the dark current. The generation current is, for the most part, independent of the magnitude of the potential difference across the depletion region because *any* potential difference results in an electric field to separate generated carriers. The recombination current comes from the statistical probability that there are electrons (holes) in the  $n$ -doped ( $p$ -doped) side that have enough thermal energy to surmount the potential barrier at the junction. The number of carriers with enough thermal energy follows Fermi-Dirac statistics and the recombination current has an exponential dependance on the temperature and the size of the potential step. The size of the potential step depends on both the contact potential at thermal equilibrium and the size of the applied voltage. The recombination

current is positive based on our definition. So, we have

$$I_{gen} \propto \text{generation rate} \quad (5.1)$$

$$\begin{aligned} I_{rec} &\propto e^{\frac{V_{applied} - V_{contact}}{k_b T}} \\ &\propto e^{V_{applied}} \end{aligned} \quad (5.2)$$

$$I_{tot} = I_{rec} - I_{gen}. \quad (5.3)$$

With no applied field and at thermal equilibrium, the total current flow must be zero and  $I_{rec}$  must equal  $I_{gen}$ . If we solve for this condition and substitute the solution back in, we have

$$I_{tot} \propto I_{gen}(e^{V_{applied}} - 1). \quad (5.4)$$

From this equation, it is easy to see how the characteristic current-voltage ( $I$ - $V$ ) behavior of a diode is achieved (see Figure 5.4 (a)). If we apply a negative voltage (back bias), the exponential term quickly goes to zero and the total current flow saturates at the small value of  $-I_{gen}$ . If we apply a positive voltage (forward bias), the current increases exponentially. This result is simply a reiteration of what the cartoon in Figure 5.3 illustrates. That is, a  $p$ - $n$  junction only allows current flow in one direction, it rectifies.

Now, let us consider what happens when light is incident onto the junction. If a photon of sufficient energy enters into the depletion region, it is absorbed and creates an electron-hole pair. Again, this electron-hole pair is separated immediately due to the internal electric field in the depletion region and we add negative contribution to the total current; this contribution is the photocurrent ( $I_L$ ) and it is proportional to the number of incident photons. We return to the equation for the total current and add on the contributing term from the photocurrent,

$$I_{tot} \propto I_{gen}(e^{V_{applied}} - 1) - I_L. \quad (5.5)$$

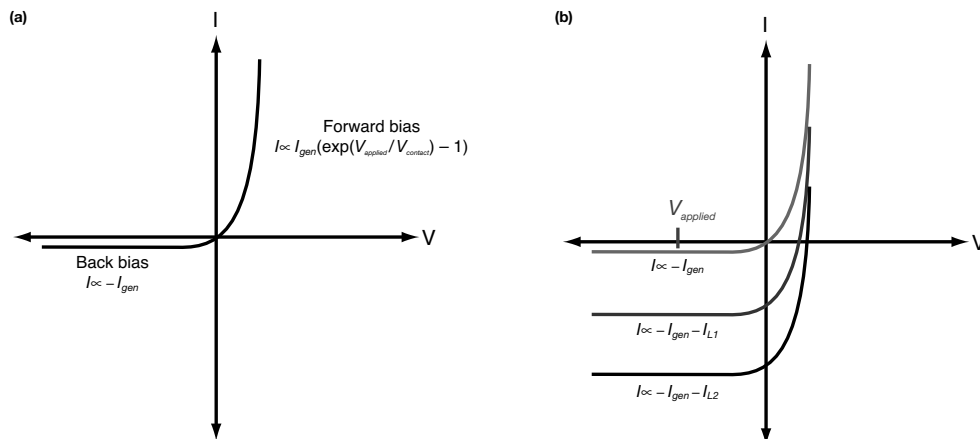


Figure 5.4: (a) The characteristic current-voltage characteristics of a  $p$ - $n$  diode. For positive applied voltage the current increases exponentially; this is the forward bias condition. For negative applied voltage the current saturates at a small negative value close to the generation current; this is the back bias condition. (b) If we shine light onto the junction, there will be a negative contribution to the total current from the generated photocurrent. The size of this contribution will be proportional to the power of the incident light. The incident power of  $L_2$  is larger than  $L_1$  and, therefore, the  $I$ - $V$  curve drops further.

The photocurrent contribution lowers the  $I$ - $V$  curve by an amount proportional to the number of incident photons (incident power). This is how a photodiode works. We set a specific back bias voltage<sup>4</sup> to operate at, shine light at the junction, and measure the contribution to the overall current from the photocurrent. Because the amount of photocurrent is proportional to the power of the incoming light, we can detect the light and determine the relative power. Figure 5.4 (b) illustrates how a photodiode is used to detect light.

## 5.2 Femtosecond-laser microstructured silicon photodiodes

Silicon is the most commonly used semiconductor in microelectronics and optoelectronic devices. It is widely used for solar cells and photodetectors, but because the band gap of crystalline silicon is 1.07 eV, the absorption and photoresponse decrease precipitously

<sup>4</sup>Operating at a back bias voltage improves detector speed and efficiency by increasing the strength of the internal electric field.

for wavelengths longer than 1100 nm. Unfortunately, there are several near-infrared wavelengths longer than 1100 nm that are widely used for both telecommunications and scientific instrumentation. For instance, crystalline silicon photodetectors are insensitive to the two primary telecommunications wavelengths, 1300 nm and 1550 nm. Currently, more expensive and exotic semiconductors, such as germanium and indium gallium arsenide, are used to detect these wavelengths, but a silicon-based near-infrared detector would lower production costs and facilitate integration with other microelectronics. Most researchers have all but given up on using pure silicon in this wavelength range and, consequently, there is a significant amount of research being done on overcoming silicon's shortcomings by using alloys or gradual integrations of more exotic semiconductors with silicon [78, 79, 80, 81, 82, 83].

Although we only discussed the  $p$ - $n$  photodiode, the same principles and ideas hold for all photodiodes. When two dissimilar materials are contacted an internal potential step builds up and a diode is formed; in the case of a  $p$ - $n$  junction, the difference between materials is the impurity carrier concentration. Photocurrent generation contributes to the total current and is a measurable way to detect light. The difference between the two sides of the junction need not come from just carrier concentration differences; there are many ways to make photodiodes. Different doping concentrations, different crystalline structure, dissimilar semiconductor materials (heterojunction), and any combination of these three differences can be used to create a photodiode.

With femtosecond-laser microstructured silicon, we have two distinct layers; the disordered surface layer and the undisturbed crystalline layer below. These two layers are different in crystalline structure, chemical composition, and doping concentration (see Chapters 3 and 4). In addition, the microstructured surface has very unique optical properties with high absorptance from the near ultraviolet deep into the near-infrared (Chapter 4). In following sections, we describe our efforts in making a photodiode that takes advantage

of the unique optical properties of silicon microstructured in the presence of SF<sub>6</sub>. We aim to use the junction between the sulfur-doped disordered surface layer and the undisturbed silicon substrate to form a diode and then characterize its photoresponse. We use all the information we know about the morphology, chemical composition, optical properties, and electronic properties of microstructured silicon to design and understand our photodiode.

### 5.2.1 Experimental

All of the photodiodes described in this chapter are silicon substrates microstructured in with a 1-kHz train of 800-nm, 100-fs pulses in 0.67 bar of SF<sub>6</sub>. The photodiodes are made while translating the substrates such that an average of 200 laser pulses strike a given area. Except for the section on the effect of original substrate doping, the silicon substrates used are *n*-doped silicon (*n*-Si(111), 260 μm thick, resistivity  $\rho = 8 - 12 \Omega \cdot \text{m}$ ).

#### Fabrication process

We microstructure approximately a  $5 \times 5 \text{ mm}^2$  area of silicon in the presence of SF<sub>6</sub>. Depending on the experiment, samples are either left alone or annealed for 30 minutes to a specified temperature following microstructuring. We then dip the samples in a 5% HF solution in order to remove the native oxide layer before making electrical contact. With the oxide layer removed, we place the samples in a thermal evaporator and make electrical contact to the microstructured side and the undisturbed substrate by evaporating chromium/gold (Cr/Au) contacts. On the microstructured side, the electrical contact is a finger grid geometry and, on the back side (undisturbed substrate), the entire surface is covered with a Cr/Au layer. Figure 5.5 (a) shows a schematic diagram of the final sample. With this contact structure, we make electrical contact to both sides of the junction and make our measurements across the junction. Figure 5.5 (b) shows a schematic diagram of

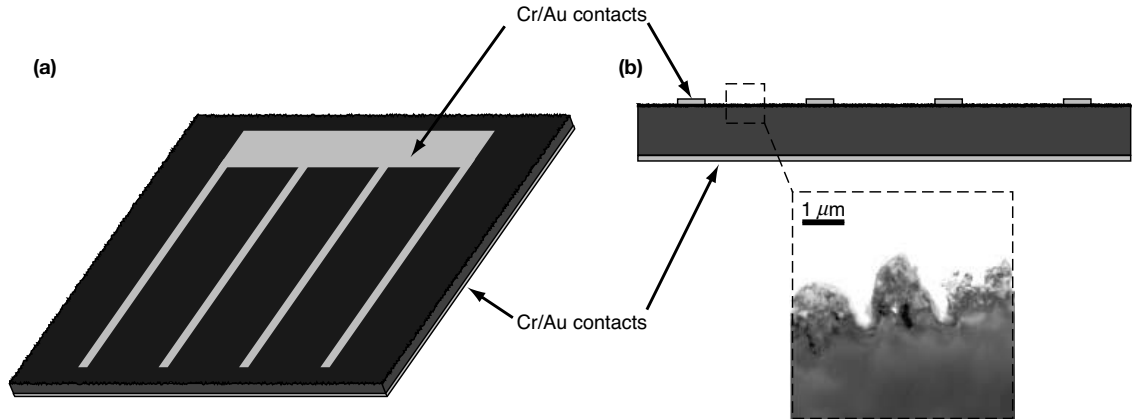


Figure 5.5: (a) A schematic diagram of a microstructured sample with electrical contacts. (b) Cross-section of a microstructured sample showing that we have contacts on either side of the junction between the disordered surface layer and the undisturbed silicon substrate. Inset: Transmission electron micrograph of a typical junction.

a cross section of a finished sample.

## Measurements

We present two types of measurement results in this chapter: the current-voltage ( $I$ - $V$ ) characteristics of the junction and spectral responsivity of the finished photodiode. The  $I$ - $V$  measurements are fairly straightforward. We apply a range of voltages across the junction and measure the resulting current. With this information we plot the  $I$ - $V$  curve for each sample. Measurements are done in the dark so no contribution from photocurrent is included. Responsivity is a way of quantifying the sensitivity of a photodiode and is the amount of photocurrent generated per unit of power of incident light (units of A/W). Spectral responsivity is measured using a 300-W xenon arc lamp light source that is passed through a monochromator with a spectral resolution of 0.1 nm. The monochromator is scanned to wavelengths over the range 400 – 1600 nm. Using a calibrated photodiode and a variable neutral density filter, we adjust the power at each wavelength to 1  $\mu$ W and then

measure the generated photocurrent. All samples are at a small back bias of  $-0.5$  volts for responsivity measurements.

## 5.2.2 Results

The results section is presented in terms of how experimental parameters affect our photodiodes'  $I$ - $V$  characteristics and responsivity. In general, the logic flow follows our efforts to optimize and understand photodiode performance.

### Effect of annealing

Before we can have a photodiode, we must first have a diode. To determine if we indeed have a diode, we perform  $I$ - $V$  measurements of finished samples. Figure 5.6 (a) shows the  $I$ - $V$  characteristics for microstructured samples<sup>5</sup> at several anneal temperatures. Immediately following laser microstructuring, with no anneal,  $I$ - $V$  measurements yield a disappointing result. The  $I$ - $V$  curve is not diodic and the current and voltage are linearly related. The difference in crystalline structure and inclusion of sulfur in the surface is not sufficient to create a significant junction between the two layers. However, Hall measurements indicate that the number of donor electrons from the microstructuring process increases dramatically with anneal temperature. Therefore, we annealed samples at several temperatures and looked for changes in the shape of the  $I$ - $V$  curves. An anneal at 725 K shifts the curve slightly and we begin to see different slopes for positive and negative biases. However, the shape is still far from what we would expect from a diode. If we increase our anneal temperature at 825 K, the curve is now diodic, with exponentially increasing current for forward bias and a smaller, less quickly increasing current for back bias. At 1075 K, the  $I$ - $V$  characteristics are similar to the ideal case, with very small current in the

---

<sup>5</sup>The samples in the annealing section were microstructured at a fluence of  $4 \text{ kJ/m}^2$ . The reason for using this fluence as the standard is discussed in the next section.

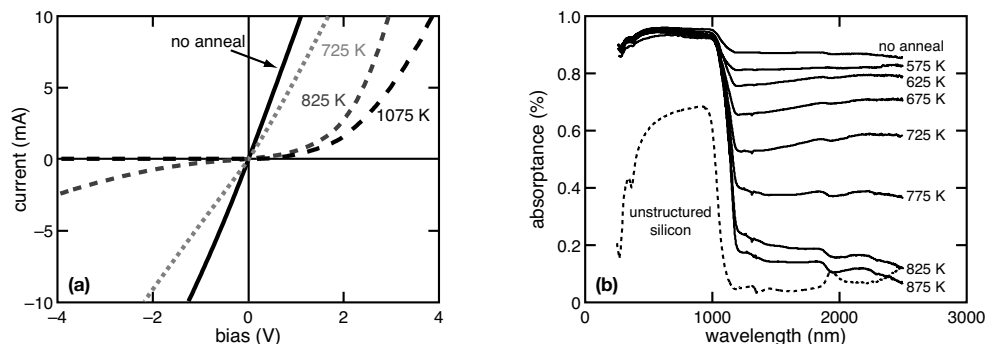


Figure 5.6: (a) The current-voltage characteristics for microstructured samples annealed to four different temperatures. Without annealing, the curve is virtually linear, indicating that the junction is not diodic, but more resistive in nature. The current-voltage characteristics get more like an ideal diode with increasing anneal temperature. (b) Wavelength dependence of absorbance on anneal temperature. Although the diodic characteristics improve with increasing anneal temperature, the near-infrared absorption drops.

back bias condition. However, there is a problem with annealing at high temperatures. The absorbance measurements for increasing anneal temperature are shown in Figure 5.6 (b). The below-band gap absorbance, that we are so interested in, decreases with increasing anneal temperature. Therefore, although we get better diodic behavior with higher anneal temperature, we start to lose the near-infrared absorbance.

The responsivity measurements for four different anneal temperatures (no anneal, 725 K, 825 K, and 1075 K) are shown in Figure 5.7. The responsivity of a commercially available silicon photodiode is also included for reference. The measurement range for the nonannealed sample is limited because the noise is very high and the response is moderate. From Figure 5.6 (a), we see that the  $I$ - $V$  characteristics for this sample are poor; it is not diodic and the current at  $-0.5$  V bias is significant. The sample annealed at 725 K exhibits very high response but is noisy (see Figure 5.6 (a)), making measurements of responsivity at these low light powers ( $1 \mu\text{W}$ ) excessively noisy for wavelengths longer than 1200 nm. The responsivity of the sample annealed at 825 K is enormous. It has nearly 100 times

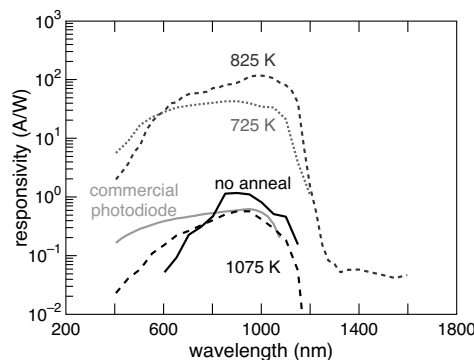


Figure 5.7: Responsivity measurements for samples annealed to four different temperatures. The measurement range for the "no anneal" sample is limited by noise. Similarly, measurements past 1200 nm were too noisy for the sample annealed at 725 K and the response was too small for the sample annealed at 1075 K. For reference, the responsivity of a commercially available silicon photodiode is shown.

larger response than a commercially available photodiode for the visible and responsivity near 100 mA/W in the near-infrared. The  $I$ - $V$  characteristics are diodic and the current at  $-0.5$  V bias is small. There is a large reduction in responsivity for the sample annealed at 1075 K. The  $I$ - $V$  characteristics of this sample are the most ideal and therefore the noise during measurement is small, but the response is much lower than the 825 K sample and there is no measurable response at wavelengths longer than 1200 nm. However, the samples annealed to 1075 K have much better responsivity at 0 V bias (quantum efficiency). We will discuss the topic of quantum efficiency *vs.* responsivity at nonzero bias later in this chapter. The commercial silicon photodiode data stops at 1100 nm because responsivity drops steeply to around  $10^{-6}$  A/W for wavelengths longer than 1100 nm [84].

From these results, we see that annealing is a crucial step in producing a photodiode with good rectification and response. Annealing at a temperature that is too low leads to a noisy photodiode, but annealing to too high a temperature lowers the response to both visible and near-infrared wavelengths. For the remaining experiments in this chapter, we present results for samples annealed at 825 K and 1075 K. The samples annealed at 825 K

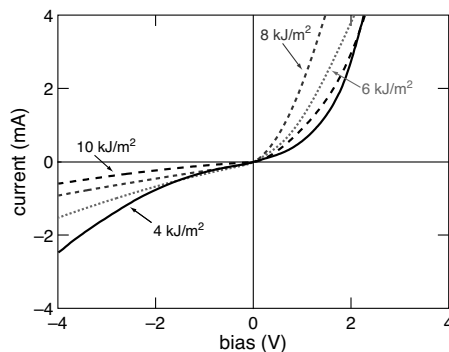


Figure 5.8: Current-voltage characteristics for microstructured samples made with four different fluences and annealed at 825 K. Increasing fluence results in lower dark current for a given back bias.

exhibit the highest response in both the visible and infrared, but the samples annealed at 1075 K are less noisy and their quantum efficiencies are higher.

### Effect of fluence

In the previous section, we presented results for annealing samples made with a fluence of  $4 \text{ kJ/m}^2$ . We will see in this section that this choice of fluence was not arbitrary. Samples made with  $4 \text{ kJ/m}^2$  are the best overall photodiodes of the fluences tested. However, it was necessary to discuss annealing before fluence in order to familiarize the reader with the importance of annealing and the reasons behind the anneal temperatures we present in this section.

In this section, we discuss the effect of laser fluence on the photodiode characteristics of microstructured silicon. Figure 5.8 shows the current-voltage characteristics for samples made with four different laser fluences ( $4 \text{ kJ/m}^2$ ,  $6 \text{ kJ/m}^2$ ,  $8 \text{ kJ/m}^2$ , and  $10 \text{ kJ/m}^2$ ) and annealed at 825 K for 30 minutes. Increasing the fluence decreases the amount of dark current for a given back bias. This behavior is likely a result of increased sulfur content in the surface layer with higher fluences (see Section 3.11). Current-voltage characteristics for

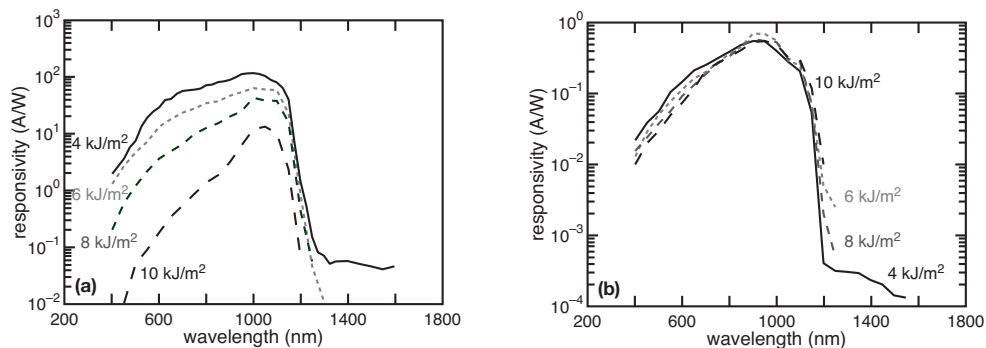


Figure 5.9: (a) Responsivity measurements for samples made with four different fluences and annealed at 825 K for 30 minutes. Samples made with 4 kJ/m<sup>2</sup> have the highest response for both the visible and near-infrared. (b) Responsivity measurements for samples made with four different fluences and annealed at 1075 K for 30 minutes. There is little variation in responsivity with fluence.

samples made with the same fluence but annealed at 1075 K do not vary significantly.

Figure 5.9 shows the responsivity for samples microstructured with four different fluences and annealed at (a) 825 K and (b) 1075 K for 30 minutes. There is a large variation in the responsivity with fluence for samples annealed at 825 K. The responsivity decreases with increasing fluence; samples made with 4 kJ/m<sup>2</sup> have the highest response. In addition, the samples made with 4 kJ/m<sup>2</sup> are the only samples with near-infrared response high enough to be measured with the low incident light power used in our measurements (1  $\mu$ W). The wavelength of peak response shifts to longer wavelengths with increased fluence. This shift is likely because of a deeper junction depth with higher fluence combined with low mobility for samples annealed to 825 K (see Section 4.2.2). The decrease in responsivity with fluence disappears for samples annealed at 1075 K, as does the shift in peak wavelength. The responsivity for samples annealed at 1075 K is nearly 100 times lower than those annealed at 825 K. However, the samples annealed at 1075 K are less noisy and have higher quantum efficiency. If the fluence is below the ablation threshold (3 kJ/m<sup>2</sup>), the current-voltage characteristics and responsivities are very poor. However, these samples were made with

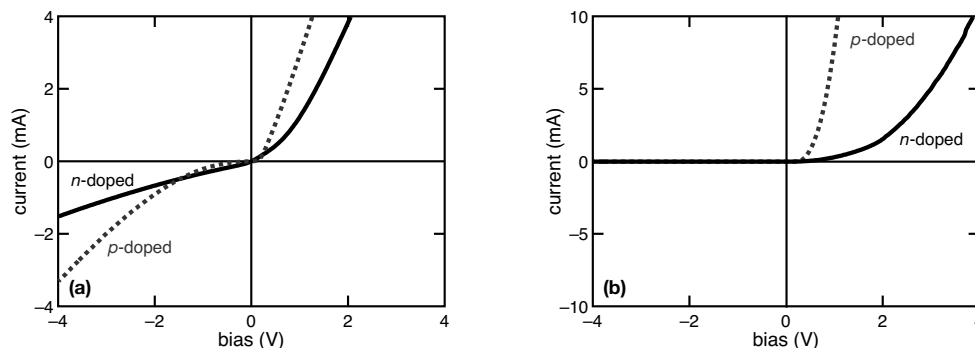


Figure 5.10: (a) Current-voltage characteristics for  $n$ -doped and  $p$ -doped substrates microstructured with a fluence of  $6 \text{ kJ/m}^2$ . Samples are annealed at  $825 \text{ K}$  for 30 minutes following microstructuring. (b) Current-voltage characteristics for  $n$ -doped and  $p$ -doped substrates microstructured with a fluence of  $4 \text{ kJ/m}^2$ . Samples are annealed at  $1075 \text{ K}$  for 30 minutes following microstructuring.

an average shot number of 200 pulses and may improve with larger shot number.

### Effect of silicon substrate doping

In this section, we examine the effect of using  $p$ -doped ( $p$ -Si(100),  $350 \mu\text{m}$  thick, resistivity  $\rho > 1 \Omega\cdot\text{m}$ ) instead of our standard  $n$ -doped substrates. Figure 5.10 shows the current-voltage characteristics for  $n$ -doped and  $p$ -doped substrates annealed at  $825 \text{ K}$  and  $1075 \text{ K}$  for 30 minutes. The  $p$ -doped samples annealed at  $825 \text{ K}$  (Figure 5.10 (a)) have a higher forward bias current than the equivalent  $n$ -doped samples. The dark current for back biases also increases more quickly for  $p$ -doped samples. Overall, the rectification is not as good for the  $p$ -doped samples. However, upon annealing at  $1075 \text{ K}$ , the  $p$ -doped samples exhibit very good diodic properties. The back bias current decreases to the same level as the equivalent  $n$ -doped samples. Also, the forward bias current increases more quickly, giving good rectification ratios. As we saw in Section 4.2.2, annealing to higher temperatures increases donor concentration from sulfur doping. The increase in donor concentration likely leads to better rectification for the  $p$ -doped samples annealed to higher temperatures.

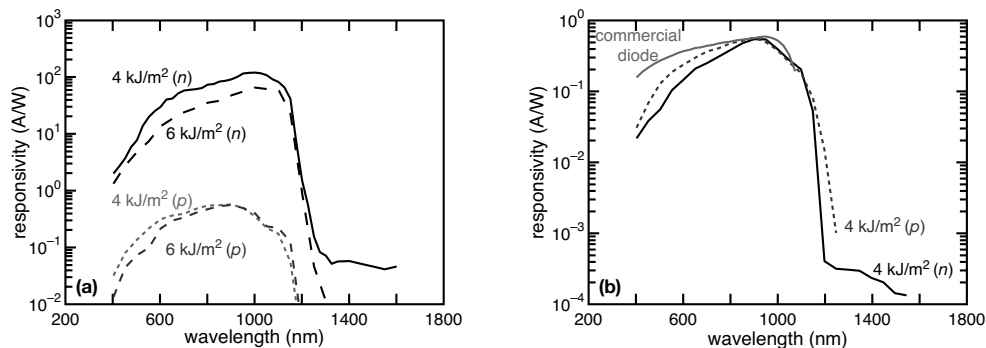


Figure 5.11: (a) Responsivity measurements for microstructured  $n$ -doped and  $p$ -doped substrates made with two different fluences ( $4 \text{ kJ/m}^2$  and  $6 \text{ kJ/m}^2$ ) and annealed at  $825 \text{ K}$  for 30 minutes. Samples made with  $4 \text{ kJ/m}^2$  have the highest response for both the visible and near-infrared. (b) Responsivity measurements for microstructured  $n$ -doped and  $p$ -doped substrates annealed at  $1075 \text{ K}$  for 30 minutes. The responsivity of a commercial silicon photodiode is shown for reference.

Varying the substrate doping has a more drastic effect on the responsivity. Figure 5.11 (a) shows the responsivity for two  $n$ -doped substrates and two  $p$ -doped samples annealed at  $825 \text{ K}$  for 30 minutes. The responsivity for  $n$ -doped substrates is much higher over the entire spectral range. The  $p$ -doped substrates have no measurable response in the near-infrared. However, if we anneal the microstructured samples at  $1075 \text{ K}$  (Figure 5.11 (b)), the responsivity for  $n$ -doped and  $p$ -doped samples is nearly identical. The response for both of these samples is similar to commercial photodiodes. In addition, the spectral responsivity for  $p$ -doped samples annealed at  $825 \text{ K}$  and  $1075 \text{ K}$  is similar. From these results, we conclude that the substrate doping plays an important role in the responsivity. The microstructured  $p$ -doped samples have a lower overall response but have better quantum efficiency.

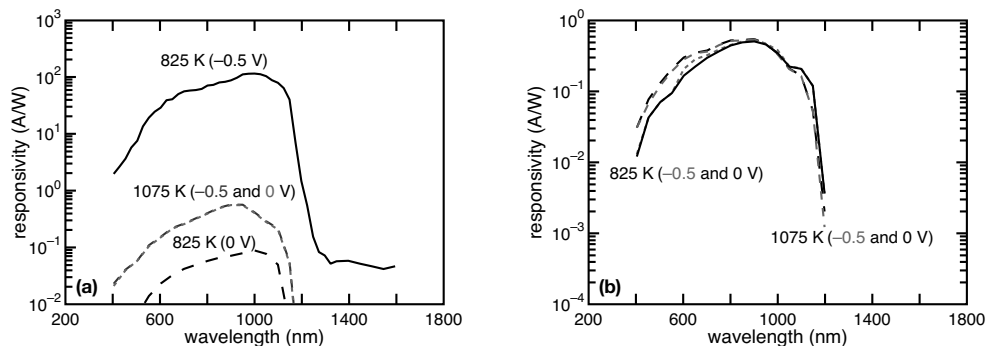


Figure 5.12: (a) Responsivity measurements for microstructured  $n$ -doped substrates made with  $4 \text{ kJ/m}^2$  and annealed at either 825 K or 1075 K for 30 minutes. Measurements are made with a back bias of  $-0.5 \text{ V}$  or with no applied bias. There is a large difference in the responsivity with a small applied bias for samples annealed at 825 K, but no difference for the samples annealed at 1075 K. (b) Responsivity measurements for microstructured  $p$ -doped substrates made with  $4 \text{ kJ/m}^2$  and annealed at either 825 K or 1075 K for 30 minutes. There is little difference in the responsivity for either case.

### Responsivity, quantum efficiency, and gain

Earlier in this chapter, we made brief reference to a difference between responsivity and quantum efficiency. Quantum efficiency, strictly defined, is the number of electron-hole pairs generated per incident photon at zero applied voltage. The measurements we have presented to this point are made at a back bias of  $-0.5 \text{ V}$  and therefore are not, strictly, quantum efficiency measurements. We showed that samples made with a fluence of  $4 \text{ kJ/m}^2$  on  $n$ -doped substrates annealed at 825 K have the highest responsivities, but this result does not mean they also have the highest quantum efficiencies.

Figure 5.12 more clearly distinguishes the difference between high responsivity and high quantum efficiency in our photodiodes. Whereas the responsivity of samples made with  $n$ -doped substrates at a fluence of  $4 \text{ kJ/m}^2$  is much higher than other samples, their responsivity at zero bias (quantum efficiency) is rather low. In fact, if we were to calculate a "quantum efficiency" for these devices at a back bias of  $-0.5 \text{ V}$ , it would be nearly 100.

Quantum efficiencies above 1 are not physically meaningful and these high values mean that there is *gain* in these samples. The gain is quite high ( $>1000$  times), especially for such a small bias. The responsivity of samples made on *n*-doped substrates and annealed to 1075 K is lower at  $-0.5$  V, but their quantum efficiency is much higher. There is a small increase in responsivity with back biasing, but it is reasonable to expect a small gain because a bias will slightly increase the depletion region and the photocarrier collection efficiency [36]. The responsivity of samples made on *p*-doped substrates and annealed at 825 K or 1075 K is also lower, but their quantum efficiencies are higher. The gain disappears with increased anneal temperature or when using a *p*-doped substrate. The responsivities of these devices is comparable to commercial silicon photodiodes, with no significant response to near-infrared light.

Figure 5.13 shows the increase in responsivity with increasing back bias for an *n*-doped substrate microstructured with a fluence of  $4 \text{ kJ/m}^2$  and annealed at 825 K for 30 minutes. The sample was illuminated with a white light source with an approximate power of  $50 \text{ } \mu\text{W}$ . The responsivity, and therefore the gain, increases quickly up to  $-5$  V and more slowly up to  $-15$  V. At voltages beyond  $-15$  V the responsivity begins to fall quickly. Although the increase in responsivity is desirable, there is a corresponding increase in noise. Also, the linearity of a photodiode is a measure of how the response changes with changing incident light power. The responsivity of devices that exhibit a large amount of gain is not very linear; the responsivity is higher at lower light powers, probably because the gain is so large that saturation occurs quickly with increasing light power. The response of samples annealed at 1075 K or made with *p*-doped substrates is more linear because they do not have significant gain with applied bias.

Therefore, it is important to keep in mind that the responsivity of a photodiode does not take into account the quantum efficiency or the noise. Therefore, the best fabrica-

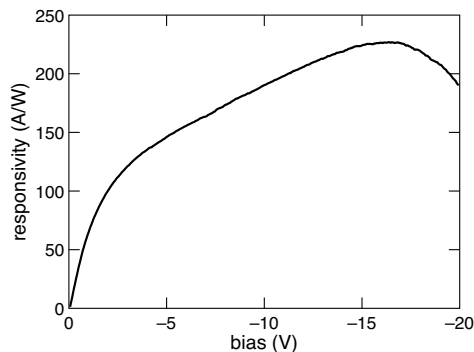


Figure 5.13: Responsivity as a function of back bias for an  $n$ -doped substrate microstructured with a fluence of  $4 \text{ kJ/m}^2$  and annealed at 825 K for 30 minutes. The sample was illuminated with a white light source with an approximate power of  $50 \mu\text{W}$ .

tion conditions for each sample depends on its intended application. That is, the trade-off between high responsivity and high quantum efficiency should be taken into account.

### Effect of temperature

For most photodetectors, it is common practice to cool the detector in order to reduce thermal noise. It is reasonable to expect that cooling our photodiodes would affect noise levels, especially since our samples are sensitive to near-infrared wavelengths<sup>6</sup>. In order to determine the effect of cooling on the characteristics of our photodiodes, we cooled an  $n$ -doped sample, made with a fluence of  $4 \text{ kJ/m}^2$  and annealed at 825 K, from room temperature down to 80 K. During cooling, we made current-voltage and responsivity measurements at increments of 10 degrees K. The highlights of this analysis are shown in Figure 5.14. Figure 5.14 (a) shows the current-voltage characteristics with decreasing temperature. The current in both the back bias and forward bias condition decreases with temperature. At very low temperatures (below 100 K), conduction becomes very low for both forward and back bias. Figure 5.14 (b) shows the responsivity to 1064 nm light at a back bias of

<sup>6</sup>All of the measurements presented thus far have been performed at room temperature.

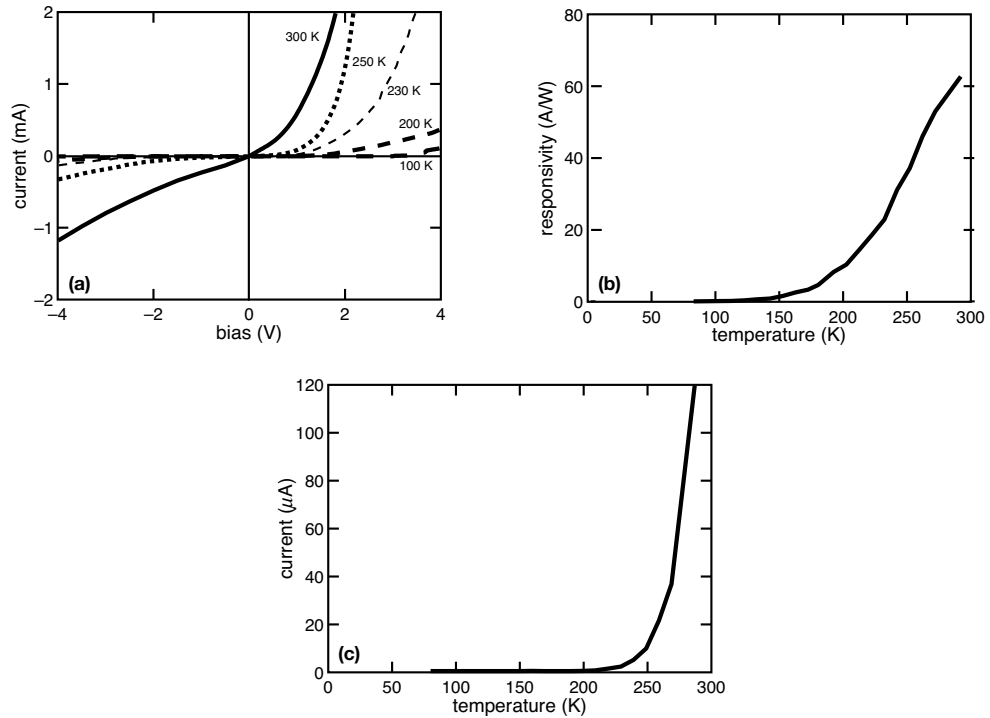


Figure 5.14: (a) The effect of decreasing temperature on the current-voltage characteristics of an  $n$ -doped sample made with a fluence of  $4 \text{ kJ/m}^2$  and annealed at  $825 \text{ K}$ . (b) The effect of decreasing temperature on responsivity of the same sample. (c) The dark current at a back bias of  $-0.5 \text{ V}$  with decreasing temperature. The dark current decreases more quickly with temperature than the responsivity.

$-0.5 \text{ V}$  with decreasing temperature. The responsivity also drops with temperature, which is likely because the wavelength used is close to the band gap of silicon at room temperature and there is an increase in the band gap with decreasing temperature [75]. Figure 5.14 (c) shows the dark current at  $-0.5 \text{ V}$  with decreasing temperature. If we take this measurement to be a rough gauge of the noise in the photodiode, it indicates that the noise decreases much more quickly than the responsivity. This information could be used to optimize device operation but more measurements, especially with below-band gap wavelengths, need to be carried out.

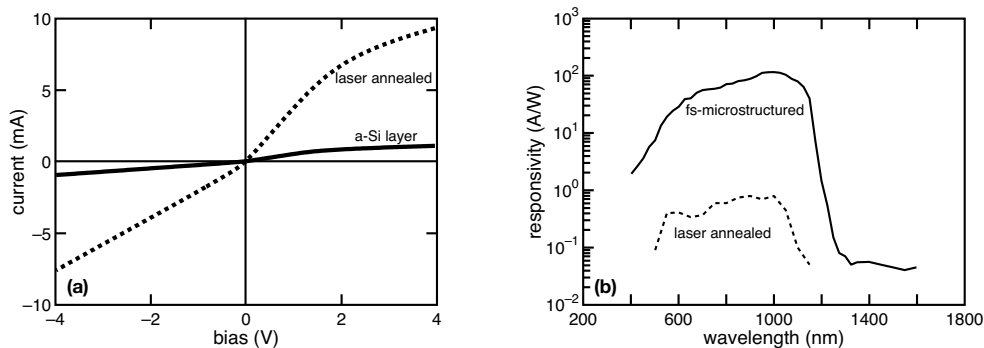


Figure 5.15: (a) The current-voltage characteristics for a heavily sulfur doped amorphous silicon layer on an  $n$ -doped substrate and the same sample after recrystallization of the amorphous layer with nanosecond laser annealing. (b) Responsivity measurements of the laser annealed surface compared to a femtosecond laser microstructured sample. Both responsivity measurements were taken with a back bias of  $-0.5$  V.

### Effect of sulfur inclusion and surface layer structure

A question that comes up in this analysis is whether it is the inclusion of high levels of sulfur alone, the structure of the surface layer, or a combination of the two that leads to the high responsivity and near-infrared sensitivity. In hopes of addressing this question, we performed three experiments trying to deconvolve the contributions of sulfur and structure. First, in collaboration with another research group [74], we prepared a sample that consisted of a thin layer of amorphous silicon with high levels of sulfur doping ( $\sim 1$  at. %) on top of our standard  $n$ -doped substrates. We then measured the current-voltage characteristics and responsivity of this sample. The current-voltage characteristics (see Figure 5.15 (a)) are far from diodic and the responsivity is too low to be measured. We then laser annealed the amorphized layer with nanosecond laser pulses in order to recrystallize the amorphized layer, while maintaining the large amount of sulfur doping. The current-voltage characteristics are also far from diodic, but the responsivity is on the level of  $n$ -doped femtosecond-laser microstructured samples before anneal. Because the  $I$ - $V$  characteristics are so poor, the

responsivity measurements are very noisy and we were not able to discern a significant below-band gap response. Figure 5.15 (a) shows the current-voltage characteristics for the amorphous silicon and laser annealed samples. Figure 5.15 (b) shows the responsivity of a laser annealed sample as compared to the  $n$ -doped microstructured substrates annealed at 825 K. Although these preliminary results are not very encouraging, this approach might prove fruitful with further experiments and variation of parameters. It is likely that the nanosecond-laser anneal does not perfectly recrystallize the surface layer and its structure has similarities to the disordered surface layer we see with femtosecond-laser microstructured samples. Lastly, we made current-voltage and responsivity measurements for nanosecond-laser microstructured annealed at 825 K for 30 minutes (see Section 3.4) surfaces. The current-voltage characteristics are more reminiscent of a resistor than a diode and noise levels are too high to make meaningful responsivity measurements. The poor performance of nanosecond-laser structured photodiodes is likely because there is no discernable disordered surface layer for these structures (see Section 3.4.1) and therefore no junction is formed. From this information, it seems that the inclusion of sulfur and the structure of the surface layer are both critical for high responsivity in the visible and the near-infrared.

### 5.3 Optimization and discussion

With the large amount of data presented in the previous sections, the goal and most important result of our experiments may have been lost. We set out to create a silicon-based photodiode that operated in both the visible and near-infrared. In short, we succeeded remarkably well in this goal. Figure 5.16 summarizes some of the main characteristics of our best performing devices. Thus far, the optimal experimental conditions are microstructuring an  $n$ -doped ( $n$ -Si(111), 260  $\mu\text{m}$  thick, resistivity  $\rho = 8 - 12 \Omega\cdot\text{m}$ ) with

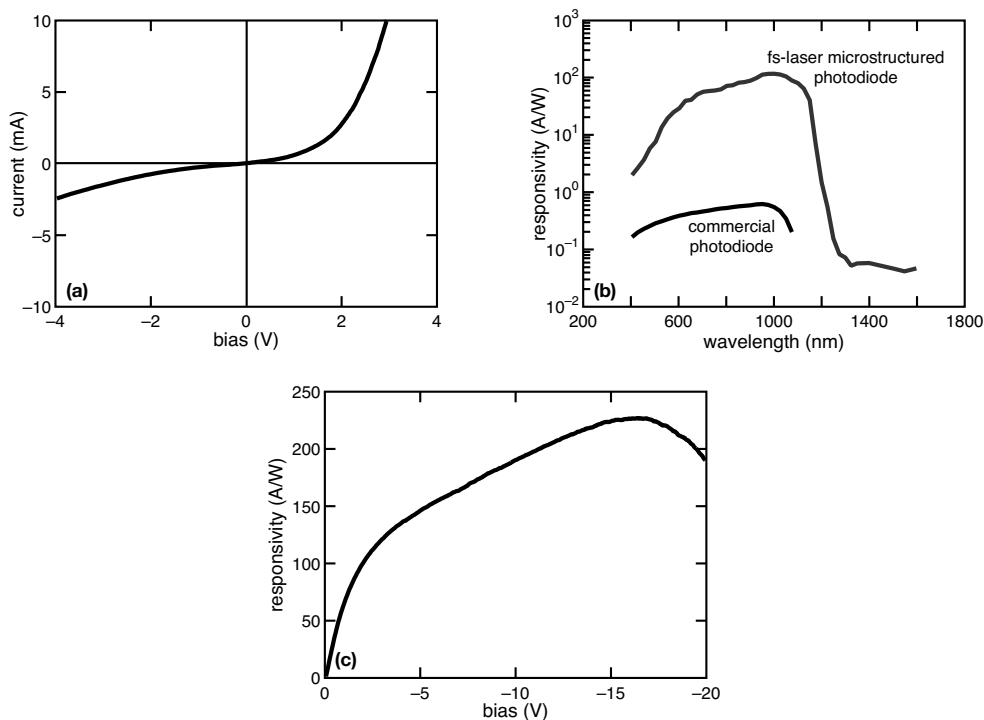


Figure 5.16: (a) The current-voltage characteristics for our best microstructured photodiode. (b) Responsivity of our best microstructured photodiode compared to a commercial silicon photodiode. (c) Responsivity with increasing applied back bias for our best microstructured photodiode.

a fluence of  $4 \text{ kJ/m}^2$  in 0.67 bar of  $\text{SF}_6$  and annealing the sample at 825 K for 30 minutes. The responsivity of this sample is nearly two orders of magnitude higher than commercial silicon photodiodes in the visible; this level of sensitivity is much higher than were anticipated. Responsivities for below-band gap wavelengths as long as 1600 nm are on the order of 100 mA/W. This responsivity is only one order of magnitude lower than commercial photodiodes that are currently used in this spectral range, and five orders of magnitude larger than silicon devices in this spectral range [84]. The mobility ( $\mu$ ) of the surface layer made with these conditions is  $101 \text{ cm}^2\text{V}^{-1}\text{s}^{-1}$ . The response times of the photodiode are 10 ns rise time and 30 ns fall time. The diode capacitance is 63.9 nF at a back bias of  $-0.5 \text{ V}$ .

Immediately following laser-microstructuring, our devices do not make very good photodiodes. Their  $I$ - $V$  characteristics are more representative of a resistor rather than a diode. Their responsivity is on the order of commercial photodiodes but is extremely noisy. It seems that the difference in crystallinity and doping between the disordered surface layer and the undisturbed substrate is not sufficient to create a diodic junction. Annealing dramatically improves both the  $I$ - $V$  characteristics and the responsivity. It is likely that the annihilation of defects and bond rearrangement during annealing (see Section 4.3) improves the  $I$ - $V$  characteristics. Removal of defects at the junction interface along with a higher carrier concentration gradient across the junction leads to improved rectification. However, the exact anneal temperature is critical because responsivity drops significantly if we anneal at too high of a temperature. In addition, high temperature anneals result in diminished below-band gap absorptance. Therefore, optimization requires finding an anneal temperature that provides a balance between good  $I$ - $V$  characteristics and good responsivity.

Arguably, the one characteristic that makes these photodiodes unique is the large gain at very small applied voltages. Our best samples have a large amount of gain ( $> 1000$  times) for an applied bias of  $-0.5$  V. Of all our samples, the ones with high gain have the best responsivity in the visible and, by far, the best responsivity for below-band gap wavelengths. It is likely that the below-band gap absorption only results in a few electron-hole pairs (photocarriers), but the gain is so large that the final photocurrent is brought up to a remarkable level. For samples with little or no gain, we do not see significant below-band gap response.

The gain is present only for certain experimental conditions and therefore we can speculate on the mechanism. For such small applied biases, the gain mechanism one would first expect is photoconductive gain [36]. Photoconductive gain comes from a difference in the recombination lifetime and transit time to the electrodes for electrons and holes.

Briefly, we can imagine a scenario in which electrons have a longer lifetime and travel to the electrodes faster than the holes. If this is the case, an electron leaves the semiconductor before the hole recombines and current continuity forces the external circuit to add another electron from the other side of the semiconductor. If the electron and hole recombination lifetimes are sufficiently long, a single photon absorption could result in several electrons contributing to the photocurrent, which amounts to gain. There are several experimental indications that this is not the case for our photodiodes. First, the mobility of the disordered surface layer is significantly less than the crystalline substrate. The disordered layer is the more  $n$ -doped side of our junction and the photogenerated electrons travel through the disordered layer on their way to the electrode. If anything, we would expect that the recombination lifetime for these electrons would be so small that we would see quantum efficiencies much less than 1. Secondly, if we anneal samples to higher temperatures, it improves the mobility but removes any gain. This result is counterintuitive to the idea of photoconductive gain because annealing to higher temperatures should remove defects and traps that reduce the recombination lifetime of carriers. The measured mobility for samples annealed at 1075 K is 20% higher than those annealed at 825 K but the responsivity is two orders of magnitude less. For the opposite electronic scenario (*i.e.* long-lifetime holes instead of electrons), it is highly unlikely that photogenerated holes are traveling all the way through the predominantly  $n$ -doped substrate and being injected into the disordered layer several times before the photogenerated electrons recombine.

The gain mechanism is more likely the result of an avalanche process from high localized electric fields at defects or collisional ionization at the highly disordered interface. The evidence for this explanation comes from the information contained in Figure 5.11. First, annealing to higher temperatures for microstructured  $n$ -doped substrates removes the gain. Annealing at 825 K leads to a small increase in the doping level but also frus-

trates conduction and mobility (see Section 4.2.2). Annealing at 1075 K leads to a large increase in the doping level but removes defects and allows for better conduction. The healing of these defects at the interface between the surface layer and the substrate decreases gain but increases quantum efficiency as carriers are more efficiently collected. Secondly, no matter what anneal temperature we use, the microstructured  $p$ -doped samples do not exhibit high gain. There is no gain in  $p$ -doped samples because the impact ionization rate for holes is nearly 1000 times less than that of electrons at these low electric field strengths [39]. The low response for  $p$ -doped samples leads to a subtlety in the conditions needed to produce our best photodiodes. Normally one designs a photodiode to have a large difference in carrier concentration across the junction because this leads to a larger internal electric field and better collection efficiency. So, for an  $n$ -doping process, such as our laser microstructuring, we normally want to start with a  $p$ -doped substrate. However, from our measurements, it is clear that  $n$ -doped substrates yield better responsivities. Therefore, an  $n$ -doped substrate is a necessary component of the gain mechanism (collisional ionization). With better understanding of the gain mechanism we can optimize conditions for gain and doping concentration on either side of the junction.

Laser fluence is also an important parameter for optimizing photodiode operation. Lower fluences deposit less energy and do less damage to the surface layer. Lower fluence results in less drastic surface topography for photoelectrons to travel across and shorter distances to electrodes (see Section 3.3). Perhaps with further investigation it may be possible to choose laser parameters that minimize change to the surface morphology and maintain good photodiode characteristics. It is, after all, not the micrometer scale morphology, but the disordered surface layer that is critical to these photodiodes. The decrease in sensitivity to shorter wavelengths for increasing laser fluence may prove beneficial for certain applications in which ultraviolet light detection is undesirable.

There is still a great deal to improve and learn with these devices. The major omission in this analysis is noise characteristics. The purpose of these experiments was to demonstrate creation of a photodiode using laser microstructured silicon and learning about the material from our measurements. The noise levels need to be reduced in these devices, which is more of an engineering pursuit than a matter of new physics or material behavior. Many improvements can be made in the device design, such as surface passivation to minimize recombination, better isolation of surface currents from leaking around the edges of samples, improved electrical contact and design, operation temperature, and defect removal at the interface without loss of response. Of particular interest for both engineering and material science is a more comprehensive analysis of the effect of annealing on the photodiode characteristics. To date, we do not know if the improvement with annealing is strictly a temperature critical effect or if anneals for longer time periods at lower temperature (kinetics) lead to the same improvement. However, we do know that annealing is a critical step for high responsivity and low noise. Lastly, there is a great deal of information contained within the  $I$ - $V$  measurements made at room temperature and while cooling. Analysis of these results might contribute to our understanding of the disordered surface layer and the energy levels of donor electrons.

In this chapter, we demonstrated the first application of femtosecond-laser microstructured silicon to create a functioning optoelectronic device. We fabricated photodiodes with sensitivity levels nearly one hundred times greater than their commercial equivalent and an expanded spectral range from 400 nm to 1600 nm. It is the nature of scientists to avoid overstatements of results, but these photodiodes are a very important discovery for the field of semiconductor photodetectors. The ease of integration and low cost of silicon makes it the most attractive and inexpensive material for photodetectors. The extension of silicon's range of spectral sensitivity and increased sensitivity to visible

light could find application in numerous devices including photodetectors, charged coupled device (CCD) cameras, and photovoltaics. The fabrication process is relatively simple and lends itself to integration with current silicon device processing techniques. With better physical understanding, we can continue to optimize the photodiodes characteristics and, we hope, apply the underlying principles to create other novel devices.

## Chapter 6

# Solar cells, field emission, and future directions

Since the first experiments involving femtosecond-laser microstructuring of silicon, there were high hopes that the process would find novel application in semiconductor devices. We felt the unique morphology and optical properties would find use in devices such as solar cells and field emission arrays. Toward these goals, we spent a great deal of effort and time gaining an understanding of both the formation mechanisms and properties of the microstructured surface. It is only in the past year that we gained the understanding and insight needed to actually produce operating devices. Our first success, highly sensitive photodiodes for the visible and near-infrared, was covered in the previous chapter, but this is only one of several applications toward which we are working. In this chapter, we present the development of two applications; femtosecond-laser microstructured solar cells and field emission arrays. These are two applications that we have worked on for several years but only had success with and understanding of since the recent photodiode work.

We begin the chapter with a brief background on the workings of solar cells and an

update on our recent progress in this pursuit. We then introduce the basic physics of field emission and present early results for femtosecond-laser microstructured field emitters. We also briefly discuss some interesting properties of microstructured silicon that might find application in the future.

## **6.1 Solar cells and renewable energy**

The current political strife and economic climate of the world has reinforced efforts towards using renewable energy sources. Wind power, solar power, and fuel cells are among the many technologies that proponents envision replacing fossil fuel consumption, the current work-horse of the energy business. Unfortunately the energy business is first and foremost concerned with profit and the cost of renewable energy technologies has hindered their implementation. For solar cells in particular, the cost per kilowatt hour (the true figure of merit for businesses) is 5-10 times the average cost of electricity from more traditional suppliers [85]. However, scientific advances and subsidies from conscientious governments are bringing the cost down every year. In the next twenty to thirty years, we hope to witness a transition to renewable energy sources as the dominant provider of electric power.

Efforts to bring down the cost of electricity from solar power are focused on increasing the conversion efficiency of sunlight into electricity and bringing down production costs. Crystalline silicon solar cells comprise the majority of solar cells being used today but the progress in creating more efficient modules at low cost has slowed. Researchers have turned to investigating other forms of silicon (amorphous and microcrystalline) and other materials (conducting polymers and more exotic semiconductors) in order to reduce the cost of solar energy [86, 87, 88, 89, 85, 90]. Progress is steadily being made and the

world market for solar cell energy is growing at a healthy pace [85].

## 6.2 Femtosecond-laser microstructured silicon solar cells

Upon discovering that femtosecond-laser microstructured silicon has near-unity absorption from the visible to the near-infrared, we became excited by possible solar cell applications [91]. First, the increased absorption for visible wavelengths promised to increase the light absorbed by silicon solar cells and, therefore, increase efficiency by reducing losses due to reflection from the silicon surface. Secondly, nearly a third of the sun's energy is at wavelengths longer than  $1.1 \mu\text{m}$  and passes unabsorbed through crystalline silicon solar cells (see Figure 6.1) [92]. Femtosecond-laser microstructured silicon is highly absorbing at these wavelengths and promised to improve efficiency by converting more of the sun's spectrum into electricity. Our initial efforts involved collaboration with solar cell companies to microstructure the surface of completed silicon solar cells. These experiments did not prove fruitful and it is only now, with our recent understanding of the microstructured surface and solar cells themselves, that we understand why did not succeed.

### 6.2.1 Introduction to solar cells

Before continuing on with the explanation of our initial efforts and getting to our recent progress, it is necessary to understand how a solar cell works. The principles are nearly the same as those we learned for photodetectors in the last chapter (see Section 5.1). Typically a solar cell is a  $p$ - $n$  junction photodiode with high quantum efficiency. The conversion of photons into photocarriers is the physical mechanism by which light is converted into electricity. However, there is a fundamental difference between a photodetector and a solar cell. Photodetectors are generally run in "photoconductive" mode, that is, they have an applied back bias and photocurrent is measured. Applying a bias amounts to putting

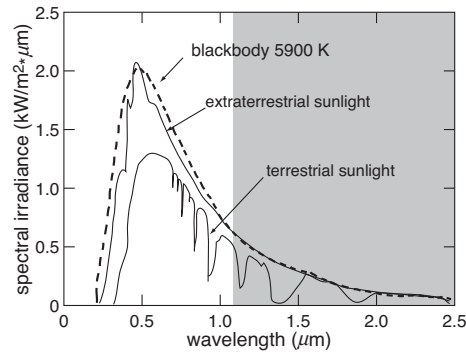


Figure 6.1: Spectral irradiance of the solar spectrum. The solar spectrum above the earth’s atmosphere is close to ideal blackbody radiation at 5900 K. Absorption by  $O_2$ ,  $H_2O$ , and  $CO_2$  molecules in the atmosphere result in dips in the terrestrial solar spectrum. The greyed out region of the graph represents the portion of the spectrum that is not absorbed by crystalline silicon solar cells. Adapted from [92].

energy into the system rather than getting energy out. Solar cells, on the other hand, are run in “photovoltaic” mode. Instead of applying a bias, the photodiode is run open circuit mode or attached to a load. Figure 6.2 illustrates the difference between photoconductive and photovoltaic modes.

In photovoltaic mode, it is possible to convert sunlight into electrical energy. As we saw in the last chapter, incident light converted into photocurrent drops the  $I$ - $V$  curve of a photodiode an amount proportional to the power of the incident light (Figure 5.4 (b)). When this occurs, portions of the  $I$ - $V$  curve lie in the bottom right quadrant of the plot, the so-called fourth quadrant. Operating a photodiode in the fourth quadrant generates electric power. To understand this, we examine the two extreme cases for the  $I$ - $V$  curve in this quadrant. The intersection of the  $I$ - $V$  curve with the voltage axis represents running a photodiode in open circuit mode (infinite resistance). On a physical level, photogenerated carriers in the depletion region are separated by the internal electric field but, since the circuit loop is open, there is nowhere for them to go. The separated photocarriers result

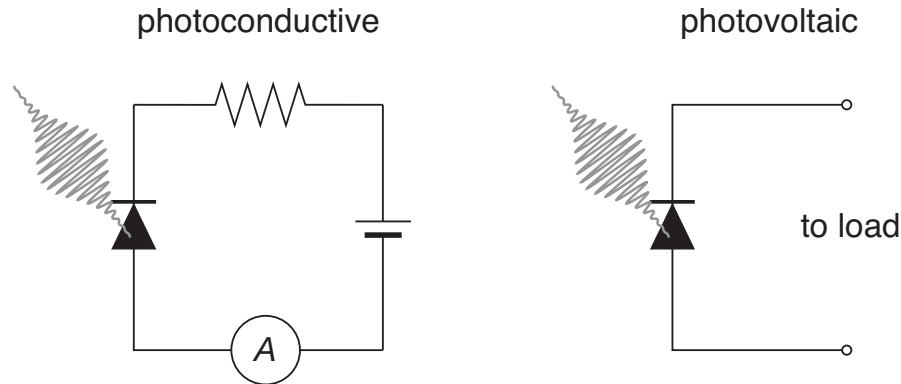


Figure 6.2: Cartoon illustrating the difference between photoconductive and photovoltaic mode.

in a separation of charge and a build up of a potential difference; this potential difference is called the open circuit voltage ( $V_{OC}$ ). Alternatively, the intersection of the  $I$ - $V$  curve with the current axis represents running a photodiode in short circuit mode (infinitely small resistance). On a physical level, there is no resistance in the circuit and therefore any photogenerated carriers contribute to the photocurrent; this current is called the short circuit current ( $I_{SC}$ ). No potential difference builds up in short circuit mode. If we pick a load with *finite* resistance, we end up somewhere along the  $I$ - $V$  curve in the middle of these two extremes. The resistance of the load determines the actual potential difference and photocurrent by Ohm's law ( $V=IR$ ). So, with a finite resistance, incident light creates a potential difference and a current, which amounts to electrical power ( $P=IV$ ).

The figure of merit for a solar cell is the conversion efficiency ( $\eta$ ), which is the percentage of incident solar power that gets converted into electrical power. Conversion efficiency, in turn, depends on three other parameters: the short circuit current ( $I_{SC}$ ), the open circuit voltage ( $V_{OC}$ ), and the fill factor ( $FF$ ). We defined short circuit current and open circuit voltage above. Fill factor is the ratio of the maximum power output to the product of the open circuit voltage and the short circuit current. Graphically, the  $I$ - $V$  curve

maps out an area within the fourth quadrant. The total area represents the total electrical power generated by the incident light, but because we have to pick a single load resistance, we are only able to realize a rectangular portion of this area. The largest rectangle we can fit into this area represents the maximum power output (maximum power rectangle) of the solar cell with a maximum voltage ( $V_m$ ) and maximum current ( $I_m$ ). The fill factor is the ratio of this realized maximum power over the ideal case of a rectangular area with sides  $I_{SC}$  and  $V_{OC}$ ,

$$FF = \frac{P_m}{I_{SC}V_{OC}} = \frac{I_m V_m}{I_{SC}V_{OC}}. \quad (6.1)$$

The maximum power rectangle and fill factor are shown graphically in Figure 6.3. The larger the fill factor, the more efficient the solar cell. The conversion efficiency is the ratio of maximum converted electrical power over the incident light power

$$\eta = \frac{P_m}{P_{in}} = \frac{FF I_{SC} V_{OC}}{P_{in}}. \quad (6.2)$$

So, for a given incident light power, we can use the fill factor, short circuit current, and open voltage to determine the efficiency of a solar cell.

### 6.2.2 Recent progress

Now that we have a basic understanding of how a solar cell works, we can discuss why our initial efforts to improve efficiency failed. We had hoped that increased absorption in the visible would increase the efficiency of solar cells by reducing the amount of reflected light. However, we now know that femtosecond-laser microstructuring results in a disordered surface layer that has a different carrier concentration than the original substrate. In essence, we are adding another junction and potential step into the finished solar cell. The conversion efficiency and quantum efficiency of a solar cell rely heavily on having no unintentional or extra potential steps introduced from processing steps. The additional

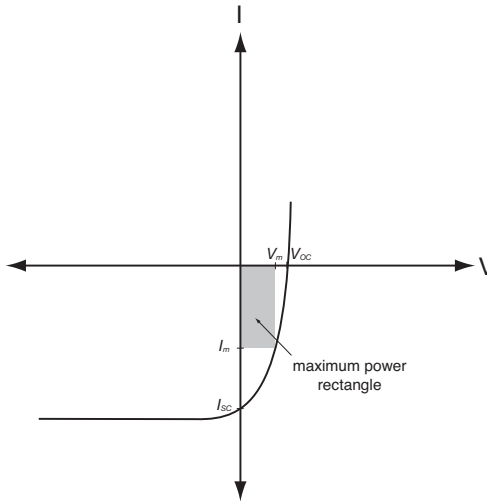


Figure 6.3: Cartoon of the maximum power rectangle of a solar cell. The fill factor is the ratio of this rectangular area over the ideal case of a rectangular area with sides  $I_{SC}$  and  $V_{OC}$ . The more rectangular the  $I$ - $V$  curve, the larger the fill factor and maximum power rectangle.

potential barrier and reduced mobility in the disordered surface layer far outweigh any advantage gained by increased absorption.

The other advantage of femtosecond-laser microstructured silicon for solar cells is the extended absorption range, which may or may not prove increase efficiency. Absorption of additional wavelengths may lead to increased photocurrent, but the open circuit voltage of a semiconductor solar cell is proportional to the semiconductor's band gap. Therefore, the extended absorption range might result in reduced open circuit voltages. In general, there is an inverse relationship between open circuit voltage and short circuit current [39].

With the knowledge we have gained about our surface layer, we are again working toward applying laser microstructuring to creating novel solar cells. Applying the lessons learned while optimizing our photodiodes, we use the  $p$ - $n$  junction created during microstructuring to create femtosecond-laser microstructured silicon solar cells. The fabrication process for samples is very similar to those used for photodiodes. We structure

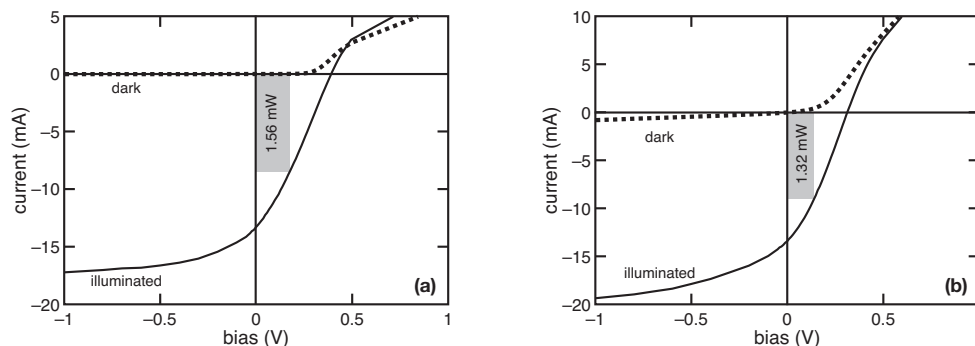


Figure 6.4: (a) The current-voltage characteristics for a high resistivity ( $\rho > 1 \Omega\cdot\text{m}$ ) microstructured substrate with and without one sun illumination. The maximum output power rectangle is shown along with the maximum power. (b) The current-voltage characteristics for a low resistivity ( $\rho = .01 - 0.1 \Omega\cdot\text{m}$ ) microstructured substrate with and without one sun illumination. The maximum power rectangle is shown along with the maximum output power.

*p*-doped crystalline silicon substrates with a fluence of  $4 \text{ kJ/m}^2$  and anneal at 1075 K for one hour. The annealing step proves critical in improving the efficiency of our samples. We then evaporate Cr/Au contacts onto the samples; finger grids are evaporated onto the microstructured surface and the contact on unstructured side covers the whole surface. We then use an Oriel<sup>TM</sup> sun simulator to illuminate the solar cell with the equivalent of one sun at high noon ( $100 \text{ mW/cm}^2$  average power). Figure 6.4 shows the *I-V* characteristics for unilluminated and illuminated solar cells made on a high resistivity ( $\rho > 1 \Omega\cdot\text{m}$ ) and a low resistivity ( $\rho = .01 - 0.1 \Omega\cdot\text{m}$ ) substrate.

The high resistivity substrate solar cell has an open circuit voltage of 0.4 Volts and a short circuit current of 13.4 mA. The fill factor is rather poor, however, and the overall efficiency is 1.56%. The low resistivity substrate solar cell has an open circuit voltage of 0.31 Volts and a short circuit current of 13.45 mA. The fill factor is also rather poor and the overall efficiency is 1.32%. Considering that these devices are made on crystalline substrates these preliminary results are mediocre. Typical commercial crystalline solar cells

have efficiencies around 14 %, depending on the manufacturer. However, we are enthusiastic about the future of this work. After all, the first crystalline solar cells were only 6 % efficient and the first amorphous silicon solar cells were only 2 % efficient [93, 94]. Because we are new to device fabrication, there are several engineering aspects involved in solar cell production that we are not very skilled in. Series resistance added from non ideal electrical contact and the resistance of the substrates can drastically reduce the fill factor. The transition from exponential growth to a linear relationship at forward biases above 0.5 V indicates that series resistances are reducing our fill factors. The numerous methods for improving solar cell efficiency with engineering is beyond the scope of this dissertation [92], but we hope to improve our efficiencies with further work. In the immediate future, we plan to improve efficiency by optimizing laser conditions, substrate doping, and annealing conditions.

Because the microstructuring process leaves the surface layer highly disordered, it is likely that we will pursue application in arenas outside of crystalline silicon solar cells. We are investigating the use of femtosecond-laser microstructured silicon for use in more novel forms of solar cells, such as thin film and hybrid polymer/semiconductor solar cells [86, 95]. Decreasing absorption depths in microcrystalline silicon solar cells could reduce growth times and increase efficiency [89]. In the solar cell research community, there is much excitement about the possibility of producing inexpensive, efficient, and flexible solar cells from conducting polymers combined with nanorods of semiconductor materials such as CdSe. The nanorods are imbedded in the polymer to improve mobility, but have a limited absorption spectra. Imbedding the conical microstructures formed during laser microstructuring with their built in  $p$ - $n$  junction might improve both the spectral absorption and the collection efficiency of these devices.

## 6.3 Field emission from femtosecond-laser microstructured silicon surfaces

Field emission from femtosecond-laser microstructured silicon surfaces was actually the intended topic of the author's dissertation work. Early experiments revealed that the field emission properties of microstructured surfaces were on par with the best technologies in the field. Furthermore, the laser microstructuring process is simpler than the lithographic processes commonly used in other field emission arrays[96]. The results were very encouraging, but there was a problem. In order to understand this problem, we first need an introduction to the basic physics of field emission. As with solar cells, the recent work with photodiodes sheds some light of the problem and recently we began investigating field emission again.

### 6.3.1 Introduction to field emission

Many of us are familiar with cathode ray tubes (CRT) in older television sets and computer monitors. In these devices, a stream of electrons is generated and accelerated toward a luminescent material on the inside glass of the monitor, lighting up the screen. The supply of electrons is generated by heating up a pointed metal cathode and thereby *thermionically* exciting electrons to energies high enough to escape the metal surface. This hot cathode emission is called thermionic emission. Field emission, in contrast, refers to the application of a large electric field that greatly perturbs the potential barrier electrons encounter at a cathode surface, thereby allowing electrons to tunnel quantum mechanically out of the surface. This process is also referred to as cold cathode emission. Field emitters and field emission arrays have numerous applications [96], but the biggest commercial effort is in using field emission for flat panel displays [97]. In general, field emitters have several

advantages over conventional vacuum electron sources. They can produce electron beams with high brightness and current density while operating at low voltages and consuming relatively little power. In addition they can be integrated into small, lightweight devices and operated with high pulse-repetition rates due to their rapid on/off switching speed.

We begin by discussing field emission from a metal surface. The original theory work describing field emission from a metal surface was done by Fowler and Nordheim [98] and is the starting point for understanding field emission from semiconductor surfaces. The following description of field emission comes mainly from the work by Fowler and Nordheim and a more recent summary by Gomer [99]. The reader is encouraged to read these references for a more in depth description.

In a metal, electrons occupy energy levels up to the Fermi energy ( $E_F$ ). In order for an electron to escape the metal and enter into the surrounding vacuum, it must overcome a potential barrier at the surface. The difference between the lowest energy level above the potential barrier and the Fermi level is called the work function ( $\phi$ )<sup>1</sup>. Figure 6.5 (a) graphically illustrates the energy level arrangement with position. If a strong electric field is applied, the potential barrier is perturbed and, instead of a step function, the barrier decreases linearly with distance from the metal/vacuum interface. If the field is strong enough, the potential barrier becomes thin enough for electrons to escape through quantum mechanical tunneling. Figure 6.5 (b) graphically illustrates the effect of an applied field on the potential barrier at the surface.

We can use the Heisenberg uncertainty principle to estimate the magnitude of the electric field necessary for tunneling. The uncertainty principle states that the uncertainty

---

<sup>1</sup>The reader might be familiar with work functions from introductory physics experiments with the photoelectric effect.

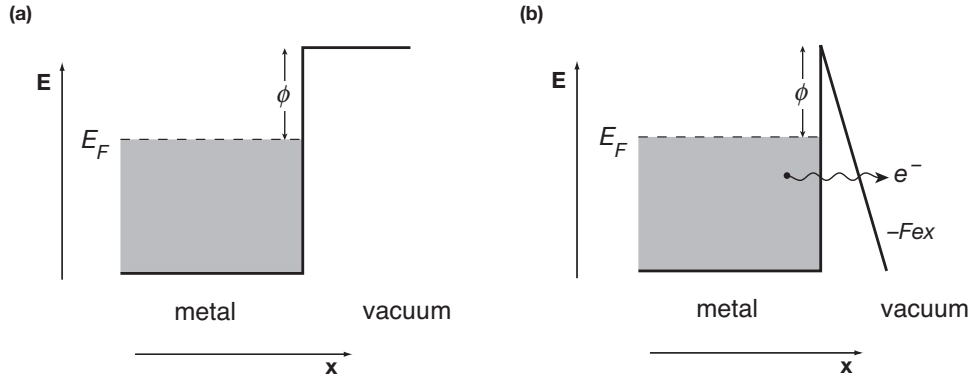


Figure 6.5: Energy level arrangement *vs.* position for field emission from a metal surface (a) without an applied electric field and (b) with an applied field. If the applied field is strong, it can perturb the potential barrier enough for electrons to quantum mechanically tunnel through.

of an electron position ( $\Delta x$ ) is related to the uncertainty of the momentum ( $\Delta p$ ) by

$$\Delta x \Delta p \geq \hbar. \quad (6.3)$$

If we consider an electron near the Fermi level, the uncertainty in momentum needed to overcome the potential barrier is

$$\Delta p = (2m\phi)^{\frac{1}{2}}. \quad (6.4)$$

For tunneling to occur  $\Delta x$  must equal the width of the perturbed potential barrier. The slope of the potential barrier under applied field  $F$  with distance  $x$  is  $-Fex$ . For an electron near the Fermi level, the potential barrier width ( $\Delta x$ ) in the applied field is

$$\Delta x = \frac{\phi}{Fe}. \quad (6.5)$$

Plugging this value for  $\Delta x$  into Heisenberg's formula we have

$$\Delta p \geq \frac{\hbar Fe}{\phi}. \quad (6.6)$$

If we set our two formulas for  $\Delta p$  equal to one another we find that

$$F \approx \frac{(2m)^{\frac{1}{2}} \phi^{\frac{3}{2}}}{\hbar e}. \quad (6.7)$$

For typical material work functions ( $\sim 5$  eV), field emission requires field strengths on the order of  $10^{10}$  V/m. An electric field of this magnitude is not easily reached, but, electric field strengths are enhanced at sharp points. For this reason field emitters are usually sharp tips; the sharper the better. Geometric enhancement can reduce the necessary macroscopic field strength down to be on the order of V/ $\mu\text{m}$  [100, 101]. The sharp, conical microstructures formed during laser microstructuring in the presence of SF<sub>6</sub> are natural candidates for field emitters.

A more rigorous mathematical calculation of field emission current as a function of applied potential difference is carried out by Fowler and Nordheim [98]. Using tunneling probability theory with the WKB (Wentzel, Kramers, and Brillouin) approximation [102], they derive the now classic Fowler-Nordheim formula for field emission from sharp metal tips:

$$J = \frac{(C\beta F)^2}{\phi} e^{-\frac{B\phi^{3/2}}{\beta F}}, \quad (6.8)$$

where  $J$  is the current density,  $F$  is the applied field,  $\phi$  is the work function,  $\beta$  is the geometric enhancement factor, and  $B$  and  $C$  are constants. If we substitute in  $J = I/A$  (with  $A$  the emission area and  $I$  the emission current) and  $F = \beta V$  (with  $V$  the applied potential difference) we arrive at a formula that relates the applied potential difference to the field emission current. Taking the logarithm of both sides of this equation and simplifying we arrive at

$$\ln(I/V^2) = \ln(a) - b(1/V), \quad (6.9)$$

where  $a$  and  $b$  are constants. This form of the Fowler-Nordheim equation shows that we expect a linear relation between the  $\ln(I/V^2)$  and  $1/V$ . Plotting measurements in this form allows one to distinguish between field emission and other emission mechanisms, such as thermionic emission.

The theory for field emission from semiconductors is similar to that of metals. The

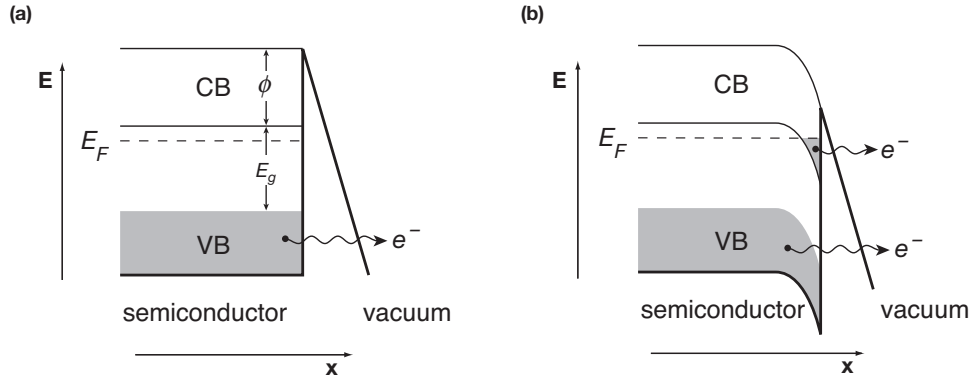


Figure 6.6: Energy level arrangement *vs.* position for field emission from a semiconductor surface in the presence of an electric field (a) without band bending from field penetration (b) and with band bending from field penetration. The conduction band is labeled CB and the valence band is labeled VB.

most significant difference is that the highest significantly occupied energy level is the top of the valence band, rather than at the Fermi level. Therefore, for the simplest case, electrons must overcome an effective work function  $\phi_{eff}$  that includes the band gap energy,

$$\phi_{eff} = E_g + \phi. \quad (6.10)$$

With a large enough applied field, electrons can tunnel from the valence band into vacuum through the perturbed potential barrier. Figure 6.6 (a) illustrates the energy level arrangement *vs.* position for a semiconductor. However, with large applied fields, the electric field penetrates into the surface layer, perturbing the energy band structure near the surface. This phenomenon is called band bending and, if the conduction band bends below the Fermi level, electrons occupy the newly available energy levels just below the Fermi level. These electrons are at a higher energy than those at the top of the valence band and tunnel through at lower electric field strengths. Figure 6.6 (a) illustrates the energy level arrangement *vs.* position for a semiconductor with band bending. Electrons emitted from the surface of a semiconductor also obey the relationships derived in the Fowler-Nordheim

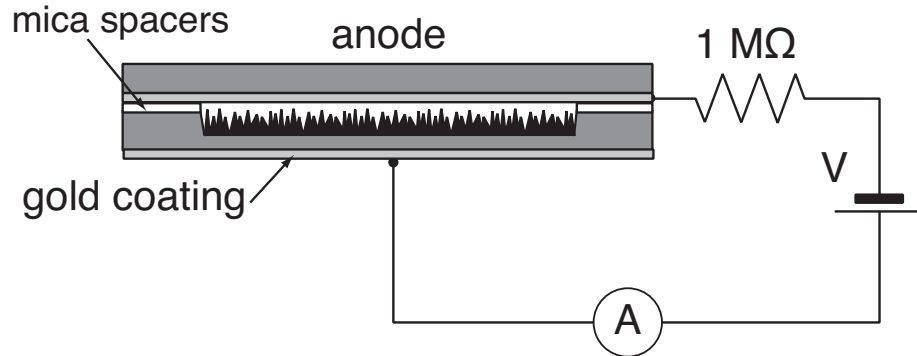


Figure 6.7: Cartoon illustration of the field emission measurement apparatus.

equation (Equation 6.9).

This background information gives us a simplified introduction to field emission theory. The reader is encouraged to refer to the work by Gomer [99] to learn more. We can now present some of our early field emission results as well as discuss the problem we mentioned earlier.

### 6.3.2 Field emission results

Our experimental procedure begins with femtosecond-laser microstructuring  $n$ -doped substrates with a fluence of  $8 \text{ kJ/m}^2$ . We then evaporate a gold contact onto the back (unstructured) surface of the sample. The sample is then clamped together with a gold-coated silicon wafer, which acts as the anode, with a pair of thin mica spacers ( $20 \mu\text{m}$ ) between the two wafers. The mica spacers are made by carefully cleaving sheets of mica using the tip of a razor blade. The mounted sample is placed in a vacuum chamber, which is evacuated to a pressure of approximately  $10^{-6}$  torr. Using vacuum feed-throughs, we apply a potential difference between the microstructured sample and the gold-coated anode. Emission current is measured at each applied voltage with a picoammeter; a  $1 \text{ M}\Omega$

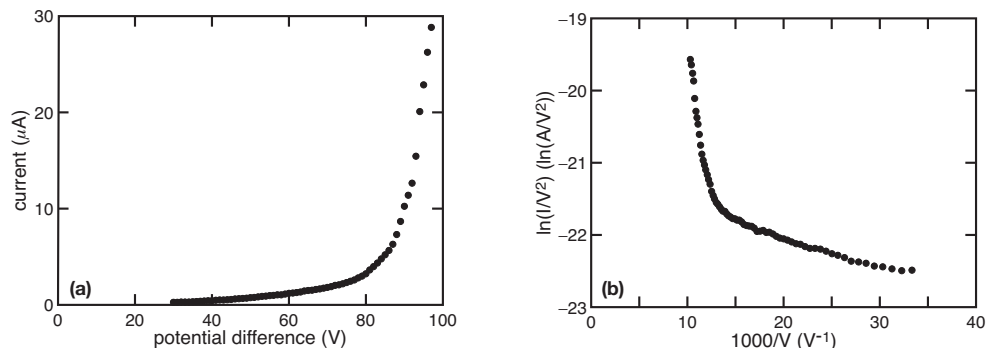


Figure 6.8: (a) Measurement of field emission current as a function of applied potential difference for a silicon surface microstructured in  $\text{SF}_6$ . (b) Fowler-Nordheim plot of the data contained in (a).

resistor is placed in series to protect the ammeter from unexpected surges in current. Figure 6.7 shows a schematic diagram of the field emission measurement apparatus.

The results of field emission measurements for samples microstructured in  $\text{SF}_6$  are shown in Figure 6.8. The figures of merit for a field emitting surface are the turn-on field, defined as the electric field (bias voltage divided by the tip-to-anode spacing) for which a current density of  $0.01 \mu\text{A}/\text{mm}^2$  is observed, and the threshold field, defined as the field at which a current density of  $0.1 \mu\text{A}/\text{mm}^2$  is produced. The turn-on field for substrates microstructured in  $\text{SF}_6$  is  $1.3 \text{ V}/\mu\text{m}$ , and the threshold field is  $2.15 \text{ V}/\mu\text{m}$ . These are excellent values, on par with carbon nanotubes, the best field emission material to date [100]. The Fowler-Nordheim plot for  $\text{SF}_6$  structured samples is shown in Figure 6.8 (b). The two linear regions of the plot indicate that there are two field emission mechanisms contributing, one at low field strength, and one at higher field strengths. Figure 6.9 shows the field emission measurements for substrates microstructured in  $\text{N}_2$ , and  $\text{Cl}_2$ , and air. One of the interesting observations from these results is that the surfaces structured in  $\text{N}_2$  have better emission characteristics than the surfaces structured in  $\text{Cl}_2$ . This result is surprising because the surfaces structured in  $\text{Cl}_2$  have much sharper microstructures (see

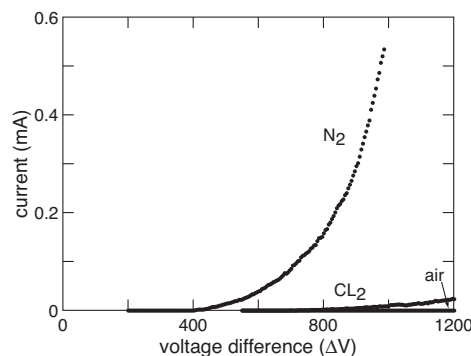


Figure 6.9: Measurements of field emission current as a function of applied potential difference for silicon surfaces microstructured in  $N_2$ ,  $Cl_2$ , and air. The surfaces structured in  $N_2$  have the highest emission currents despite having much blunter microstructures than surfaces structured in  $Cl_2$ .

Section 3.7.1). This difference indicates that it might not be geometric effects alone that cause high emission currents for the  $SF_6$  structured surfaces.

These are encouraging results but, as we mentioned, there is a problem. If one looks at the apparatus arrangement shown in Figure 6.7, there should only be current flow for potential differences where the anode is at a higher potential than the cathode. Electrons are only attracted to higher potentials and applying a potential difference in the opposite direction should result in no current flow. However, when we reversed the polarity of our applied potential, we measured a current. It had an exponential dependence on applied potential but increased at a much slower rate than the field emission current. This issue was cause for concern and we speculated that there was a short circuit in our setup and therefore could not definitively claim that our field emission measurements were accurate. The author spent several years investigating the source of this current and, after many attempts to fix the experimental setup, we moved on to investigate other areas. It is only now, after we discovered that we are creating a  $p-n$  junction during laser microstructuring, that we understand the source of this spurious behavior. By applying a potential difference

that is higher at the back side of the microstructured substrate, we are in fact forward biasing the laser created  $p$ - $n$  junction.

With this new insight we have returned to investigating field emission properties from laser microstructured surfaces. We recently imaged luminescence from a phosphor coated anode; this result indicates that electrons are indeed escaping the silicon surface and traveling to the anode. We are therefore confident that our original results are measurements of field emission current rather than a short circuit. We are also reinforced in this conclusion because other research groups have subsequently investigated field emission from nanosecond-laser microstructured surfaces and measured similar turn-on and threshold fields [103].

## 6.4 Future directions

In this dissertation we presented results on the application of microstructured silicon surfaces in novel photodetectors, solar cells, and field emission devices. These applications are only a subset of the applications that we are currently investigating or plan to investigate. Among the other applications are photoluminescent surfaces [38], micro-manipulation of biomagnetic material, and increased efficiency for drug delivery. We also demonstrated superhydrophilic behavior for microstructured surfaces, and alternatively, superhydrophobic behavior for microstructured surfaces coated with teflon. The increased surface area and electronic properties of substrates microstructured in  $\text{SF}_6$  also might find application in biological and chemical sensors. The future is bright with possibilities and we hope that the applications presented in this dissertation are just the beginning.

## Chapter 7

# Summary and outlook

Over the last decade, interdisciplinary work has gained momentum as the paradigm for the future of academic research. The work contained within this dissertation is truly interdisciplinary, representing an intersection between ultrafast optical science, material science, chemistry, and solid state device physics. We begin by creating femtosecond laser pulses with a complicated, multi-stage laser system. We then focus the laser pulses down onto the surface of silicon causing a light-material interaction with enormous intensities and temperatures that rival conditions at the surface of the sun. The resulting new material has unique morphologies, optical, and electronic properties. By investigating the chemical and structural makeup of the newly formed material we then applied our knowledge to design and create novel optoelectronic devices.

This dissertation contains the current state of our understanding of femtosecond-laser microstructured silicon. We presented analysis of the morphology, structural, and chemical composition of microstructured surfaces with varying experimental parameters. This analysis allowed us to determine a more complete picture of formation mechanisms and gain insight into the interaction between the molten silicon surface and the ambient gas

environment. We then analyzed the effect of many of the same experimental parameters on optical and electronic properties of microstructured silicon. With this information, combined with structural and chemical measurements, we explained the source of the near-unity below-band gap absorption for surfaces microstructured in SF<sub>6</sub>.

With this new found insight into the surface properties, we made the first functioning optoelectronic device using femtosecond-laser microstructured silicon; a highly sensitive silicon-based photodiode for both the visible and near-infrared spectrum. We extended the usable wavelength region of silicon detectors into a previously inaccessible region that has numerous applications in communications and sensing, an accomplishment that might significantly change the commercial landscape for near-infrared detection. We analyzed the effect of experimental parameters on the sensitivity of laser-microstructured photodiodes and identified the presence of a large gain mechanism at small biases. This gain mechanism is critical for the high response of our photodiodes for both the visible and infrared regime. We then presented the beginnings of our work toward using femtosecond-laser microstructured silicon in other devices such as solar cells and field emission arrays. The unique properties of the microstructured surface hold great potential for these and other novel applications.

For each of the areas of research, be it femtosecond laser-material interaction, investigation of material structure after structuring, or novel device design, there are many interesting questions and problems still to be investigated. With each experiment we gain insight into the inner workings of femtosecond-laser microstructured silicon and with each new insight we are better able to take advantage of its unique properties.

I hope that I presented the reader with compelling evidence that the future is bright for this work. Essentially, we have created an entirely new material through the interaction of intense femtosecond laser pulses with silicon in a sulfur containing environment.

---

The resulting chemical and structural makeup are unique to these experimental conditions and, subsequently, the optical and electronic properties are unique as well. Although this accomplishment alone is exciting, I feel that we have just scratched the surface, so to speak. The information in this dissertation deals primarily with the inclusion of a single element, sulfur, into the surface of a single semiconductor, silicon. The true power of our experimental procedure is that we can dope nearly any surface with any element to very high levels in a structurally unique way. The number of possible combinations is enormous and I expect that many more combinations will have novel properties and find useful application. I doubt that we are so lucky as to stumble upon the one important combination with our first attempt.

# References

- [1] T.-H. Her, R. J. Finlay, C. Wu, S. Deliwala, and E. Mazur, “Microstructuring of silicon with femtosecond laser pulses,” *Appl. Phys. Lett.*, vol. 73, p. 1673, 1998.
- [2] T.-H. Her, *Femtochemistry at gas/solid interfaces*. PhD thesis, Harvard University, 1998.
- [3] Z. Ghousheng, P. M. Fauchet, and A. E. Siegman, “Growth of spontaneous periodic surface structures on solids during laser illumination,” *Phys. Rev. B*, vol. 26, p. 5366, 1982.
- [4] H. M. van Driel, J. E. Sipe, and J. F. Young, “Laser-induced periodic surface structures on solids: a universal phenomenon,” *Phys. Rev. Lett.*, vol. 49, p. 1955, 1982.
- [5] S. R. Foltyn, “Surface modification of materials by cumulative laser irradiation,” in *Pulsed Laser Deposition of Thin Films* (D. B. Chrisey and G. K. Hubler, eds.), New York: Wiley-Interscience, 1994.
- [6] J. E. Rothenberg and R. Kelly, “Laser sputtering. Part II. The mechanism of the sputtering of  $\text{Al}_2\text{O}_3$ ,” *Nucl. Instrum. Meth. Phys. Res. B*, vol. 1, p. 291, 1984.
- [7] F. Sanchez, J. L. Morenza, R. Aguiar, J. C. Delgado, and M. Varela, “Whiskerlike structure growth on silicon exposed to ArF excimer laser irradiation,” *Appl. Phys. Lett.*, vol. 69, p. 620, 1996.
- [8] F. Sanchez, J. L. Morenza, R. Aguiar, J. C. Delgado, and M. Varela, “Dynamics of the hydrodynamical growth of columns on silicon exposed to ArF excimer-laser irradiation,” *Appl. Phys. A*, vol. 66, p. 83, 1998.
- [9] W. Kautek and J. Krüger, “Femtosecond-pulse laser microstructuring of semiconducting materials,” in *Material Science Forum* (D. B. Chrisey and G. K. Hubler, eds.), vol. 173-174, p. 17, Switzerland: Trans Tech Publications Inc., 1995.
- [10] A. J. Pedraza, J. D. Fowlkes, and D. H. Lowndes, “Silicon microcolumn arrays grown

- by nanosecond laser irradiation,” *Appl. Phys. Lett.*, vol. 74, p. 2322, 1999.
- [11] T.-H. Her, R. J. Finlay, C. Wu, and E. Mazur, “Femtosecond laser-induced formation of spikes on silicon,” *Appl. Phys. A*, vol. 70, p. 383, 2000.
- [12] A. J. Pedraza, J. D. Fowlkes, S. Jesse, C. Mao, and D. H. Lowndes, “Surface microstructuring of silicon by excimer-laser irradiation in reactive atmospheres,” *Appl. Surf. Sci.*, vol. 168, p. 251, 2000.
- [13] J. D. Fowlkes, A. J. Pedraza, and D. H. Lowndes, “Microstructural evolution of laser-exposed silicon targets in SF<sub>6</sub> atmospheres,” *Appl. Phys. Lett.*, vol. 77, p. 1629, 2000.
- [14] V. V. Voronov, S. I. Dolgaev, S. V. Lavrishchev, A. A. Lyalin, A. V. Simakin, and G. A. Shafeev, “Formation of conic microstructures upon pulsed laser evaporation of solids,” *Quantum Electron.*, vol. 30, p. 710, 2000.
- [15] S. I. Dolgaev, S. V. Lavrishev, A. A. Lyalin, A. V. Simakin, V. V. Voronov, and G. A. Shafeev, “Formation of conical microstructures upon laser evaporation of solids,” *Appl. Phys. A*, vol. 73, p. 177, 2001.
- [16] J. D. Fowlkes, A. J. Pedraza, D. A. Blom, and H. M. M. III, “Surface microstructuring and long-range ordering of silicon nanoparticles,” *Appl. Phys. Lett.*, vol. 80, p. 3799, 2002.
- [17] A. J. Pedraza, J. D. Fowlkes, and Y.-F. Guan, “Surface nanostructuring of silicon,” *Appl. Phys. A*, vol. 77, p. 277, 2003.
- [18] C. Wu, *Femtosecond laser-gas-solid interactions*. PhD thesis, Harvard University, 2000.
- [19] C. Wu, C. H. Crouch, L. Zhao, J. E. Carey, R. J. Younkin, J. Levinson, E. Mazur, R. M. Farrel, P. Gothoskar, and A. Karger, “Near-unity below-band gap absorption by microstructured silicon,” *Appl. Phys. Lett.*, vol. 78, p. 1850, 2001.
- [20] R. Younkin, *Surface studies and microstructure fabrication using femtosecond laser pulses*. PhD thesis, Harvard University, 2001.
- [21] D. G. Georgiev, R. J. Baird, I. Avrutsky, G. Auner, and G. Newaz, “Controllable excimer-laser fabrication of conical nano-tips on silicon thin films,” *Appl. Phys. Lett.*, vol. 84, p. 4881, 2004.
- [22] S. Deliwala, *Time-resolved studies of molecular dynamics using nano- and femtosecond laser pulses*. PhD thesis, Harvard University, 1995.

- [23] R. J. Finlay, *Femtosecond-laser-induced reactions at surfaces*. PhD thesis, Harvard University, 1998.
- [24] J. F. Young, J. E. Sipe, and H. M. van Driel, "Laser-induced periodic surface structure. III. Fluence regimes, the role of feedback, and details of the induced topography in germanium," *Phys. Rev. B*, vol. 30, p. 2001, 1984.
- [25] J. F. Young, J. S. Preston, H. M. van Driel, and J. E. Snipe, "Laser-induced periodic surface structure. II. Experiments on Ge, Si, Al, and brass," *Phys. Rev. B*, vol. 27, p. 1155, 1983.
- [26] L. S. Dake, D. E. King, J. R. Pitts, and A. W. Czanderna, "Ion beam bombardment effects on solid surfaces at energies used for sputter depth profiling," in *Beam effects, surface topography and depth profiling in surface analysis* (A. W. Czanderna, T. E. Madey, and C. J. Powell, eds.), New York: Plenum Press, 1998.
- [27] M. D. Betterton, *Things Fall Apart: Topics in Biophysics and Pattern Formation*. PhD thesis, Harvard University, 2000.
- [28] P. Keblinski, S. R. Phillpot, D. Wolf, and H. Gleiter, "Thermodynamically stable amorphous intergranular films in nanocrystalline silicon," *Phys. Lett. A*, vol. 226, p. 205, 1997.
- [29] P. L. Liu, R. Yen, N. Bloembergen, and R. T. Hodgson, "Picosecond laser-induced melting and resolidification morphology on silicon," *Appl. Phys. Lett.*, vol. 34, p. 12, 1979.
- [30] F. Spaepen and D. Turnbull, "Crystallization processes," in *Laser Annealing of Semiconductors* (J. M. Poate and J. W. Mayer, eds.), New York: Academic Press, 1982.
- [31] J. A. Leavitt, L. C. McIntyre, and M. R. Weller, "Backscattering spectrometry," in *Handbook of Modern Ion Beam Analysis* (J. H. Tesmer, C. J. Maggiore, M. Nastasi, J. C. Barbour, and J. W. Mayer, eds.), Pittsburgh: Material Research Society, 1995.
- [32] A. J. Garratt-Reed and D. C. Bell, *Energy dispersive X-ray analysis in the electron microscope*. Oxford: BIOS Scientific Publisher, 1st ed., 2003.
- [33] <http://www.genplot.com>.
- [34] A. Cavalleri, K. Sokolowski-Tinten, J. Bialkowski, M. Schreiner, and D. von der Linde, "Femtosecond melting and ablation of semiconductors studied with time of flight mass spectroscopy," *Journal of Appl. Phys.*, vol. 85, p. 3301, 1999.
- [35] M. Meunier, B. Fiset, A. Houle, A. V. Kabashin, S. V. Broude, and P. Miller, "Pro-

- cessing of metals and semiconductors by a femtosecond laser-based microfabrication system,” *Proc. SPIE Vol. 4978*, vol. 4978, p. 169, 2003.
- [36] B. Saleh and M. Teich, *Fundamentals of Photonics*. New York: Wiley-Interscience, 1st ed., 1991.
- [37] N. Bloembergen, “Fundamentals of laser-solid interactions,” in *Laser-Solid Interactions and Laser Processing* (S. D. Ferris, H. J. Leamy, and J. M. Poate, eds.), New York: American Institute of Physics, 1979.
- [38] C. Wu, C. H. Crouch, L. Zhao, and E. Mazur, “Visible luminescence from silicon surfaces microstructured in air,” *Appl. Phys. Lett.*, vol. 81, p. 1999, 2002.
- [39] S. M. Sze, *Physics of Semiconductor Devices*. New York: Wiley-Interscience, 2nd ed., 1981.
- [40] R. M. Bradley and J. M. E. Harper, “Theory of ripple topography induced by ion bombardment,” *J. Vac. Sci. Technol. A*, vol. 6, p. 2390, 1988.
- [41] J. Erlebacher, M. J. Aziz, E. Chason, M. B. Sinclair, and J. A. Floro, “Spontaneous pattern formation on ion bombarded Si(001),” *Phys. Rev. Lett.*, vol. 82, p. 2330, 1999.
- [42] J. Erlebacher, M. J. Aziz, E. Chason, M. B. Sinclair, and J. A. Floro, “Nonlinear amplitude evolution during spontaneous patterning of ion-bombarded Si(001),” *J. Vac. Sci. Technol. A*, vol. 18, p. 115, 2000.
- [43] Z. X. Jiang and P. F. A. Alkemade, “The complex formation of ripples during depth profiling of Si with low energy, grazing oxygen beams,” *Appl. Phys. Lett.*, vol. 73, p. 315, 1998.
- [44] G. Carter and V. Vishnyakov, “Roughening and ripple instabilities on ion-bombarded Si,” *Phys. Rev. B*, vol. 54, p. 17647, 1996.
- [45] T. M. Mayer, E. Chason, and A. J. Howard, “Roughening instability and ion-induced viscous relaxation in SiO<sub>2</sub> surfaces,” *J. Appl. Phys.*, vol. 76, p. 1633, 1994.
- [46] S. Rusponi, C. Boragno, and U. Valbusa, “Ripple structure on Ag(110) surface induced by ion sputtering,” *Phys. Rev. Lett.*, vol. 78, p. 2795, 1997.
- [47] E. Chason, T. M. Mayer, B. K. Kellerman, D. T. McIlroy, and A. J. Howard, “Roughening instability and evolution of the Ge(001) surface during ion sputtering,” *Phys. Rev. Lett.*, vol. 72, p. 3040, 1994.
- [48] A. J. Pedraza, J. D. Fowlkes, and D. H. Lowndes, “Self-organized silicon microcolumn

- arrays generated by pulsed laser irradiation,” *Appl. Phys. A*, vol. 69 [Suppl.], p. S731, 1999.
- [49] D. H. Lowndes, J. D. Fowlkes, and A. J. Pedraza, “Early stages of pulsed-laser growth of silicon microcolumns and microcones in air and SF<sub>6</sub>,” *Appl. Surf. Sci.*, vol. 154-155, p. 647, 2000.
- [50] A. J. Pedraza, J. D. Fowlkes, and D. H. Lowndes, “Laser ablation and column formation in silicon under oxygen-rich atmospheres,” *Appl. Phys. Lett.*, vol. 77, p. 3018, 2000.
- [51] V. I. Emel’yanov and D. V. Babak, “Defect capture under rapid solidification of the melt induced by the action of femtosecond laser pulses and formation of periodic surface structures on a semiconductor surface,” *Appl. Phys. A*, vol. 74, p. 797, 2002.
- [52] J. H. Sanderson, R. V. Thomas, W. A. Bryan, W. R. Newell, P. F. Taday, and A. J. Langley, “Multielectron-dissociative-ionization of SF<sub>6</sub> by intense femtosecond laser pulses,” *J. Phys. B: At. Mol. Opt. Phys.*, vol. 30, p. 4499, 1997.
- [53] R. S. Wagner and W. C. Ellis, “Vapor-liquid-solid mechanism of single crystal growth,” *Appl. Phys. Lett.*, vol. 4, p. 89, 1964.
- [54] P. G. Carey and T. W. Sigmon, “In-situ doping of silicon using the gas immersion laser doping (GILD) process,” *Appl. Surf. Sci.*, vol. 43, p. 325, 1989.
- [55] R. Reitano, P. M. Smith, and M. J. Aziz, “Solute trapping of group III, IV, and V elements in silicon by an aperiodic stepwise mechanism,” *J. Appl. Phys.*, vol. 76, p. 1518, 1994.
- [56] M. Y. Shen, C. H. Crouch, J. E. Carey, R. Younkin, M. Sheehy, C. M. Friend, and E. Mazur, “Formation of regular arrays of silicon microspikes by femtosecond laser irradiation through a mask,” *Appl. Phys. Lett.*, vol. 82, p. 1715, 2003.
- [57] T. M. Rassias, *The problem of Plateau - A tribute to Jesse Douglas and Tibor Radó*. New Jersey: River Edge, 1st ed., 1992.
- [58] A. R. Zanatta and I. Chambouleyron, “Absorption edge, band tails, and disorder of amorphous semiconductors,” *Phys. Rev. B*, vol. 53, p. 3833, 1996.
- [59] <http://www.eeel.nist.gov/812/hall.html>.
- [60] L. J. van der Pauw, “A method of measuring the specific resistivity and hall effect on discs of arbitrary shapes,” *Philips Res. Repts.*, vol. 13, p. 1, 1958.

- [61] C. G. Bernhard, "Structural and functional adaptation in a visual system," *Endeavor*, vol. 26, p. 79, 1967.
- [62] K. Noda, B. J. Glover, P. Linstead, and C. Martin, "Flower colour intensity depends on specialized cell shape controlled by a Myb-related transcription factor," *Nature*, vol. 269, p. 661, 1994.
- [63] E. S. Kolesar, V. M. Bright, and D. M. Sowders, "Optical reflectance reduction of textured silicon surfaces coated with an antireflective thin film," *Thin Solid Films*, vol. 290-291, p. 23, 1996.
- [64] J. Zhao, A. Wang, M. Green, and F. Ferrazza, "19.8% efficient honeycomb textured multicrystalline and 24.4% monocrystalline silicon solar cells," *Appl. Phys. Lett.*, vol. 73, p. 1991, 1998.
- [65] H. G. Craighead and R. E. Howard, "Microscopically textured optical storage media," *Appl. Phys. Lett.*, vol. 39, p. 532, 1981.
- [66] J. I. Gittleman, E. K. S. and H. W. Lehmann, and R. Widmer, "Textured silicon: A selective absorber for solar thermal conversion," *Appl. Phys. Lett.*, vol. 35, p. 742, 1979.
- [67] E. S. Kolesar, V. M. Bright, and D. M. Sowders, "Mid-infrared ( $2.5 \leq \lambda \leq 12.5 \mu\text{m}$ ) optical absorption enhancement of textured silicon surfaces coated with an antireflective thin film," *Thin Solid Films*, vol. 270, p. 10, 1995.
- [68] M. A. Sheehy, "Chalcogen doping of silicon with femtosecond laser irradiation above the ablation threshold." to be submitted, 2004.
- [69] M. J. Aziz, "Interface attachment kinetics in alloy solidification," *Metallurgical and Materials Transactions A*, vol. 27A, p. 671, 1996.
- [70] F. A. Trumbore, "Solid solubilities of impurity elements in germanium and silicon," *Bell Syst. Tech. Journal*, vol. 39, p. 205, 1960.
- [71] J. I. Pankove, *Optical Processes in Semiconductors*. New York: Dover Publications, 1st ed., 1971.
- [72] A. Agarwal, H. J. Gossman, D. J. Eaglesham, L. Pelaz, J. M. Poate, and T. E. Haynes, "Critical issues in ion implantation of silicon below 5 keV: Defects and diffusion," *Mater. Sci. Eng. A*, vol. 253, p. 269, 1998.
- [73] S. Roorda, S. Saito, and W. C. Sinke, "Solid phase epitaxial regrowth of microcrystalline Si films on a (100) Si substrate," *Mat. Res. Soc. Symp. Proc.*, vol. 100, p. 417,

- 1988.
- [74] J. M. Warrender and M. J. Aziz private communication, 2004.
- [75] N. W. Ashcroft and N. D. Mermin, *Solid State Physics*. New York: Saunders College Publishing, 1st ed., 1976.
- [76] A. Yariv, *Optical Electronics*. New York: Holt, Rinehart, and Winston, 3rd ed., 1985.
- [77] W. Shockley, "The theory of  $p$ - $n$  junctions in semiconductors and  $p$ - $n$  junction transistors," *Bell. Syst. Tech. J.*, vol. 28, p. 435, 1949.
- [78] Z. Lo, R. Jiang, Y. Zheng, L. Zang, Z. Chen, S. Zhu, X. Cheng, and Z. Liu, "Staircase band gap  $\text{Si}_{1-x}\text{Ge}_x/\text{Si}$  photodetectors," *Appl. Phys. Lett.*, vol. 77, p. 1548, 2000.
- [79] M. E. kurdi, P. Boucaud, S. Sauvage, G. Fishman, O. Kermarrec, Y. Campidelli, D. Bensahel, G. Saint-Girons, I. Sagnes, and G. Patriarche, "Silicon-on-insulator waveguide photodetector with Ge/Si self-assembled islands," *J. Appl. Phys.*, vol. 92, p. 1858, 2003.
- [80] A. Y. Loudon, P. A. Hiskett, G. S. Buller, R. T. Carline, D. C. Herbert, W. Y. Leong, and J. G. Rarity, "Enhancement of the infrared detection efficiency of silicon photon-counting avalanche photodiodes by use of silicon germanium absorbing layers," *Opt. Lett.*, vol. 27, p. 219, 2002.
- [81] G. Masini, L. Colace, G. Assanto, H.-C. Luan, and L. C. Kimerling, "High-performance p-i-n Ge on Si photodetectors for the near infrared: From model to demonstration," *IEEE Trans. Electron Devices*, vol. 48, p. 1092, 2001.
- [82] D. Buca, S. Winneri, S. Lenk, S. Mantl, and C. Buchal, "Metal-germanium-metal ultrafast infrared detectors," *J. Appl. Phys.*, vol. 92, p. 7599, 2002.
- [83] R. Calarco, M. Fiordelisi, S. Lagomarsino, and F. Scarinci, "Near-infrared metal-semiconductor-metal photodetector integrated on silicon," *Thin Solid Films*, vol. 391, p. 138, 2001.
- [84] M. Ghioni, A. Lacaita, G. Ripamonti, and S. Cova, "All-silicon avalanche photodiode sensitive at  $1.3 \mu\text{m}$  with picosecond time resolution," *IEEE J. Quantum Electron.*, vol. 28, p. 2678, 1992.
- [85] <http://www.nrel.gov>.
- [86] W. U. Huynh, J. J. Dittmer, and A. P. Alivisatos, "Hybrid nanorod-polymer solar cells," *Science*, vol. 295, p. 2425, 2002.

- 
- [87] N. Jensen, R. M. Hausner, R. B. Bergmann, J. H. Werner, and U. Rau, "Optimization and characterization of amorphous/crystalline silicon heterojunction solar cells," *Prog. Photovolt: Res. Appl.*, vol. 10, p. 1, 2002.
- [88] J. Yang, A. Banerjee, and S. Guha, "Amorphous silicon based photovoltaics—from earth to the "final frontier",," *Sol. Energy Mater. Sol. Cells*, vol. 78, p. 597, 2003.
- [89] A. V. Shah, J. Meier, E. Vallat-Sauvain, N. Wyrsh, U. Kroll, C. Droz, and U. Graf, "Material and solar cell research in microcrystalline silicon," *Sol. Energy Mater. Sol. Cells*, vol. 78, p. 469, 2003.
- [90] M. A. Green, K. Emery, D. L. King, S. Igari, and W. Warta, "Solar cell efficiency tables (version 17),," *Prog. Photovolt: Res. Appl.*, vol. 9, p. 49, 2001.
- [91] E. Juengst, "Silicon valleys," *Discover Magazine*, vol. 20, February 1999.
- [92] A. Goetzberger, J. Knobloch, and B. Voss, *Crystalline Silicon Solar Cells*. West Sussex: John Wiley and Sons Ltd., 1st ed., 1998.
- [93] D. M. Chapin, C. S. Fuller, and G. L. Pearson, "A new silicon p-n junction photocell for converting solar radiation into electrical power," *J. Appl. Phys.*, vol. 25, p. 676, 1954.
- [94] D. E. Carlson and C. R. Wronski, "Amorphous silicon solar cell," *Appl. Phys. Lett.*, vol. 28, p. 671, 1976.
- [95] W. U. Huynh, J. J. Dittmer, N. Teclamarium, D. J. Milliron, and A. P. Alivisatos, "Charge transport in hybrid nanorod-polymer composite photovoltaic cells," *Phys. Rev. B*, vol. 67, p. 115326, 2003.
- [96] I. Brodie and P. Schwoebel, "Vacuum microelectronic devices," *Proc. of the IEEE*, vol. 82, p. 1006, 1994.
- [97] A. A. Talin, K. A. Dean, and J. E. Jaskie, "Field emission displays: a critical review," *Solid-State Electron.*, vol. 45, p. 963, 2001.
- [98] R. H. Fowler and L. Nordheim, "Electron emission in intense electric fields," *Proc. Roy. Soc. (London) A*, vol. 119, p. 173, 1928.
- [99] R. Gomer, *Field Emission and Field Ionization*, vol. 9 of *Harvard Monographs in Applied Science*. Cambridge, Massachusetts: Harvard University Press, 1st ed., 1961.
- [100] J.-M. Bonard, M. Croci, C. Klinke, R. Kurt, O. Noury, and N. Weiss, "Carbon nanotube films as electron field emitters," *Carbon*, vol. 40, p. 1715, 2002.

- 
- [101] H. C. Lo, D. Das, J. S. Hwang, K. H. Chen, C. H. Hsu, C. F. Chen, and L. C. Chen, "SiC-capped nanotip arrays for field emission with ultralow turn-on field," *Appl. Phys. Lett.*, vol. 83, p. 1420, 2003.
- [102] E. Merzbacher, *Quantum Mechanics*, ch. 7. New York: John Wiley and Sons, Inc., 3rd ed., 1998.
- [103] A. V. Karabutov, V. D. Frolov, E. N. Loubnin, A. V. Simakin, and G. A. Shafeev, "Low-threshold field electron emission of si micro-tip arrays produced by laser ablation," *Appl. Phys. A*, vol. 76, p. 413, 2003.